

Iron Carbide Development and its Effect on Inhibitor Performance

A thesis presented to
the faculty of
the Russ College of Engineering and Technology of Ohio University

In partial fulfillment
of the requirements for the degree
Master of Science

Akram A. Al-Asadi

December 2014

© 2014 Akram A. Al-Asadi. All Rights Reserved.

This thesis titled
Iron Carbide Development and its Effect on Inhibitor Performance

by
AKRAM A. AL-ASADI

has been approved for
the Department of Chemical and Biomolecular Engineering
and the Russ College of Engineering and Technology by

David Young
Research Associate Professor in Chemical and Biomolecular Engineering

Dennis Irwin
Dean, Russ College of Engineering and Technology

ABSTRACT

AL-ASADI, AKRAM A., M.S., December 2014, Chemical Engineering

Iron Carbide Development and its Effect on Inhibitor Performance

Director of Thesis: David Young

Several types of mild steel are used in pipeline transmission. Steels with similar mechanical properties, e.g., yield strengths, have different contents and structures of iron carbide. This leads to different corrosion behaviors and corrosion inhibitor performance.

The purpose of the present study is to develop an understanding of how iron carbide layers, derived from the different microstructures of carbon steels during corrosion, affect corrosion behavior and inhibitor performance.

Glass cell experiments were conducted with 2 liters of 1 wt. % NaCl as the electrolyte at the desired temperature. A magnetic stirrer, set to 200 rpm, was used to ensure a fully mixed solution as carbon dioxide gas was constantly sparged into the test electrolyte. The solution pH was adjusted to the desired pH by addition of deoxygenated 1.0 M sodium hydroxide (NaOH) or sodium bicarbonate (NaHCO₃) solutions. Hydrochloric acid (HCl) was used to maintain the pH around 5.0 ± 0.1 . Three steel samples were immersed in the glass cell once the pH stabilized and tests were run for 3 days. Steels with different microstructures and chemical compositions were used in separate sets of experiments. After 24 hours of each experiment, a sample was withdrawn for surface analysis.

In addition, experiments show that iron carbide layer development is dependent upon the microstructure and chemical composition, particularly carbon content, of the carbon steel from which it is derived.

In each case, iron carbide impairs the performance of tested imidazoline-type inhibitors. The Fe_3C developed from X65 (0.14 wt. % C) steel (ferrite-discrete cementite) has significantly more effect (i.e. decreases the inhibition efficiency) on the performance of inhibitors than the Fe_3C developed from other types of steel. The performance of the inhibitor on X65 (0.05 wt. % C) spheroidized was less impaired than the performance of the inhibitor on other types of steel. In addition, the performance of the inhibitor after 1 day pre-corrosion is also dependent on the microstructure and chemical composition of the steel.

Keywords: CO₂ corrosion, iron carbide, iron carbonate, steel microstructure, normalized, spheroidized, quenched, and tempered.

DEDICATION

*I would like to dedicate my humble effort to my family whose affection, love,
encouragement, and prayers of the day and night
made me able to achieve such success*

ACKNOWLEDGMENTS

The author would like to thank HCED (Higher Committee for Educational Development in Iraq) for their financial support, Dr. David Young, Dr. Srdjan Nestic, Dr. Bruce Brown, Dr. Marc Singer and Dr. Fernando Farelas.

I would like to attribute my success in completing my thesis to the guidance of my committee members, support from my family and friends.

I express my deepest gratitude to my advisor, Dr. David Young, for his excellent guidance, patience, care, providing me with an excellent atmosphere for doing my research, and patiently correcting me. I would like to thank my project leader Dr. Bruce Brown. Despite his lack of time, he always had time for me. I would also like to thank Dr. Srdjan Nestic and Dr. Marc Singer for their excellent guidance. I would like to thank Dr. Fernando Farelas for guiding my research for the past several years and helping me to develop my background in microstructure. Special thanks go out to Dr. David Bayless and Dr. Michael Held for their guidance and best suggestions. My research would not have been possible without their help.

My gratitude also goes out to my committee members, Dr. Marc Singer, Dr. David Bayless and Dr. Michael Held for their support and academic advice in my proposal and thesis. I would like to take this opportunity to express my sincere gratitude to technical staff at the Institute for Corrosion and Multiphase Technology, Mr. Cody Shafer, Mr. Steve Upton and Mr. Alexis Barxias for providing me the necessary technical assistance and support in my experimental work. I also would like to thank all the students for their help. I would like to acknowledge the Higher Committee for

Educational Development in Iraq, HCED, for their financial support during my MS. I would like also to thank all the sponsoring companies for their technical and financial support during my MS. work. I would like to acknowledge T. B. Massalski, Thaddeus B. , et al., Binary alloy phase diagrams, and John Wiley and Sons, Inc. for letting me reproduce their material. Also, my gratitude goes out to all my family members, my mother, my sisters and brothers.

Continuously, they were supporting me and encouraging me with their best wishes. They were always there cheering me up and standing by me through the good and bad times.

TABLE OF CONTENTS

	Page
Abstract.....	3
Dedication.....	5
Acknowledgments.....	6
List of Tables	10
List of Figures	12
Chapter 1: Introduction.....	25
Chapter 2: Literature Review.....	27
2.1 CO ₂ Corrosion.....	27
2.1.1 Chemical Reactions	27
2.1.2 Electrochemical Reactions.....	28
2.1.3 Mass Transport.....	29
2.1.4 Corrosion Product as Iron Carbonate.....	30
2.2 Effects of Flow.....	31
2.3 Effects of Steel Composition and Microstructure.....	32
2.3.1 Corroding Substrate as an Exposed Steel	32
2.3.2 Corrosion Inhibitors and Metallurgical Characteristics	36
2.4 Corrosion Product.....	36
2.4.1 Iron Carbide Layer (Cementite)	37
2.4.2 Effect of Steel Microstructure and Composition on the Structure of Iron Carbide	38
2.4.3 Effect of Iron Carbide on the Corrosion Rate.....	39
2.5 Inhibitors.....	39
2.5.1 Effect of the Iron Carbide Layer on Inhibitor Performance	40
2.5.2 Effect of Chemical Composition on Corrosion Rate and Inhibitor Performance	40
Chapter 3: Hypotheses and Research Objectives.....	42
3.1 Hypotheses.....	42
3.2 Research Objective	44
3.3 Methodology.....	44

Chapter 4: Metallographic Analysis	46
4.1 Introduction.....	46
4.2 Chemical Composition of Chosen Steels.....	53
4.3 Microstructure of Chosen Steels.....	54
Chapter 5: General Corrosion Experiments.....	66
5.1 Introduction.....	66
5.2 Experimental Set-up and Instrumentation	67
5.3 Results and Discussion.....	74
5.3.1 Development of Experimental Procedures.....	74
5.3.1.1 Summary for Development of Experimental Procedures.....	85
5.3.2 Investigation of Fe ₃ C Characteristics Related to The Microstructure of The Steel.....	86
5.3.2.1 Summary for Fe ₃ C Characteristics & Corrosion	134
5.3.3 Investigating The Effect of Residual Fe ₃ C on Inhibitor Performance:	136
5.3.3.1 Summary for Effect of Residual Fe ₃ C on Corrosion Inhibition.....	169
Chapter 6: Conclusions and Future Work.....	170
6.1 Conclusions.....	170
6.2 Future Work	176
6.3 Industrial Applicability	177
References.....	178
Appendix A: Analytical Report	184

LIST OF TABLES

	Page
Table 1: Chemical Composition of X65 (0.14 wt. % C)	53
Table 2: Chemical Composition of X65 (0.05 wt. % C)	53
Table 3: Chemical Composition of C1018	53
Table 4: Hardness Values of The Different Microstructures.....	59
Table 5: Microstructure and Heat Treatment of The Selected Steels	65
Table 6: Test Conditions.....	70
Table 7 : Test Environment.....	70
Table 8: Experimental Parameters for Electrochemical Measurements	71
Table 9: Thickness of Iron Carbide	84
Table 10: Thickness of Iron Carbide for C1018 Ferrite-Pearlite Steel.....	103
Table 11: Thickness of Iron Carbide for C1018 Spheroidized Steel	109
Table 12: Thickness of Iron Carbide for C1018 Quenched-Tempered Steel	114
Table 13: Thickness of Iron Carbide for X65 (0.14 wt. % C) Steel	120
Table 14: Thickness of Iron Carbide for X65 (0.05 wt.% C) Steel	126
Table 15: Thickness of Iron Carbide for X65 (0.05 wt.% C) Spheroidized Steel	134
Table 16: Summary for Fe ₃ C Characteristics of Corroded X65 and C1018 Steels	135
Table 17: Thickness of Iron Carbide with Imidazoline-Type Inhibitor for C1018 Ferrite-Pearlite steel	147
Table 18: Thickness of Iron Carbide with Imidazoline-Type Inhibitor for C1018 Spheroidized	151

Table 19. Thickness of Iron Carbide with Imidazoline-Type Inhibitor for C1018 Quenched-Tempered.....	155
Table 20: Thickness of Iron Carbide with Imidazoline-Type Inhibitor for X65 (0.14 wt. % C)	159
Table 21: Thickness of Iron Carbide with Imidazoline-Type Inhibitor for X65 (0.05 wt.% C).....	163
Table 22: Thickness of Iron Carbide with Imidazoline-Type Inhibitor for X65 (0.05 wt.% C) Spheroidized	168
Table 23: Summary of Corrosion Rate Data for X65 and C1018 Using Different Methods	170
Table 24: Summary of Corrosion Rate Data for X65 and C1018 Using Different Methods.....	171
Table 25: Summary of Corrosion Rate Data for X65 and C1018 Using Different Methods	172

LIST OF FIGURES

	Page
Figure 1: Iron carbonate development on ferritic-pearlitic steels (figure adapted from Akeer's PhD dissertation) [25].	34
Figure 2: Schematic drawing of different microstructures: (a) sample of ferretic-discrete cementite microstructure (b) sample of a corroded ferretic-discrete cementite microstructure (c) sample of ferretic-pearlitic microstructure and arrow showing corroded sample anchored carbide lamellae (d) sample of a corroded ferretic-pearlitic microstructure and arrow showing corroded sample anchored carbide lamellae.	43
Figure 3: The Fe-Fe ₃ C diagram, a portion of the Fe ₃ C diagram, and the evolution of the microstructure of hypoeutectoid steels during a cooling process (This material is reproduced with permissions of John Wiley and Sons, Inc.) [37].	47
Figure 4: Fe-C phase diagram of the phase transformation from austenite to ferrite/pearlite (slow cooling) and from austenite to martensite (fast cooling) [38].	49
Figure 5: CCT diagram of the phase transformation of 0.4 wt.% C, 1.5 wt.% Mn, and 0.5 wt.% Mo steel from austenite to martensite in the fast cooling processes (figure reproduced with permission) [39].	51
Figure 6: CCT diagram of the final obtained microstructure (martensite) of 0.4 wt.% C, 1.5 wt.% Mn, and 0.5 wt.% Mo steel from austenite to martensite in the fast cooling processes (figure reproduced with permission) [39].	51

Figure 7: CCT diagram of the phase transformation of 0.4 wt.% C, 1.5 wt.% Mn, and 0.5 wt.% Mo steel from austenite to ferrite in the slow cooling processes (figure reproduced with permission) [39].....	52
Figure 8: CCT diagram of the phase transformation of 0.4 wt.% C, 1.5 wt.% Mn, and 0.5 wt.% Mo steel from austenite to ferrite/pearlite in the slow cooling processes (figure reproduced with permission) [39].....	52
Figure 9: Samples preparation for metallographic analysis.....	55
Figure 10: Microstructure of X65 (0.14 wt. % C) consists of tempered martensite: (a) IFM image; (b) SEM image.....	57
Figure 11: Microstructure of X65 (0.05 wt. % C) consists of tempered martensite: (a) IFM image; (b) SEM image.....	57
Figure 12: Ferrite-pearlite microstructure of C1018: (a) IFM image (b) SEM image....	58
Figure13: Spheroidized microstructure of C1018: (a) IFM image; (b) SEM image; (c) EDS images of spheroidized steel in ferrite matrix; (d) EDS images of spheroidized steel at grain boundaries.....	61
Figure 14: Spheroidized microstructure of X65 (0.05 wt. %C): (a) IFM image (b) SEM image (c) EDS images of spheroidized steel with ferrite matrix.....	62
Figure 15: Quenched-tempered microstructure of C1018: (a) IFM image (b) SEM image (c) EDS images of quenched-tempered steel at a bright grain (d) EDS images of quenched-tempered steel at black a grain.....	64
Figure 16: Experimental cell design- 1- Ag/AgCl reference electrode, 2- Thermocouple probe, 3- Luggin capillary, 4- Cylindrical working electrode, 5-Condenser, 6- pH probe,	

7- Counter electrode, 8- Hot plate, 9- Stir bar, 10- Hanging samples (adapted from a drawing provided by Cody Shafer in ICMT).....	68
Figure 17: Diagrammatic representation of measurement plan.....	
Figure 18: Corrosion rate vs. time for experiments conducted at pH=6 at 40°C, 60°C and 80°C with X65 steel.....	75
Figure 19: Corrosion rate vs. time for experiments conducted at pH 5.0 and pH 6.0 at 60°C with X65 steel.....	76
Figure 20: Sample (X65) for bulk solution pH 6.0 at 80°C after 1 day (a) SEM image for the surface (b) EDS spectrum for the surface (c) BES image for the surface, (d) SEM image for the cross section, (e) EDS spectrum for the cross section, and (f) BES image for the cross section	80
Figure 21: Sample (X65) for bulk solution pH 6 at 60°C after 1 day (a) SEM image for the surface, (b) EDS spectrum for the surface , (c) BES image for the surface, (d) SEM image for the cross section, (e) EDS spectrum for the cross section, and (f) BES image for the cross section	81
Figure 22: Sample (X65) for bulk solution pH 6 at 40°C after 1 day (a) SEM image for the surface , (b) EDS spectrum for the surface , (c) BES image for the surface, (d) SEM image for the cross section, (e) EDS spectrum for the cross section, and (f) BES image for the cross section	82
Figure 23: Sample (X65) for bulk solution pH 5 at 60°C after 1 day (a) SEM image for the surface, (b) EDS spectrum for the surface , (c) BES image for the surface, (d) SEM	

image for the cross section, (e) EDS spectrum for the cross section, and (f) BES image for the cross section	83
Figure 24: Schematic drawing of different microstructures: (a) sample of ferretic-discrete cementite microstructure (b) sample of a corroded ferretic-discrete cementite microstructure	84
Figure 25: Corrosion rate vs. time for experiments conducted at pH 5.0 and 60°C with C1018 ferrite-pearlite steel	87
Figure 26: LPR and weight loss corrosion rate vs. time for experiments conducted at pH 5.0 and 60°C on C1018 ferrite-pearlite steel	88
Figure 27: Corrosion rate vs. time for experiments conducted at pH 5.0 and 60°C with C1018 spheroidized steel	89
Figure 28: LPR and weight loss corrosion rate vs. time for experiments conducted at pH 5.0 and 60°C on C1018 spheroidized steel	90
Figure 29: Corrosion rate vs. time for experiments conducted at pH 5.0 and 60°C with C1018 quenched-tempered steel	91
Figure 30: LPR and weight loss corrosion rate vs. time for experiments conducted at pH 5.0 and 60°C on C1018 quenched-tempered steel	92
Figure 31: Corrosion rate vs. time for experiments conducted at pH 5.0 and 60°C with X65 (0.14 wt.% C) steel.....	93
Figure 32: LPR and weight loss corrosion rate vs. time for experiments conducted at pH 5.0 and 60°C on X65 (0.14 wt.% C) steel.....	94

Figure 33: Corrosion rate vs. time for experiments conducted at pH 5.0 and 60°C with X65 (0.05 wt.% C) steel.....	95
Figure 34: LPR and weight loss corrosion rate vs. time for experiments conducted at pH 5.0 and 60°C on X65 (0.14 wt.% C) steel.....	96
Figure 35: Corrosion rate vs. time for experiments conducted at pH 5.0 and 60°C with X65 (0.05 wt.% C) spheroidized steel	97
Figure 36: LPR and weight loss corrosion rate vs. time for experiments conducted at pH 5.0 and 60°C on X65 (0.05 wt.% C) spheroidized steel	98
Figure 37: Sample (C1018 Ferrite-Pearlite Steel) for bulk solution pH 5.0 at 60°C (a) SEM image for the surface after 1 day exposure, (b) SEM image for the surface after two day exposure, (c) SEM image for the surface after 3 day exposure, (d) SEM image for the cross-section after 1 day exposure, (e) SEM image for the cross-section after two day exposure, and (f) SEM image for the cross-section after 3 day exposure	100
Figure 38: Microstructure of sample (C1018 Ferrite-Pearlite Steel) for bulk solution pH 5.0 at 60°C for the cross-section after 3 days exposure (a) SEM image at 500x magnification , (b) SEM image at 1000x magnification, (c) SEM image at 2000x magnification, and (d) SEM image at 4000x magnification.....	101
Figure 39: Elemental mapping of C1018 Ferrite-Pearlite Steel sample surface after recovery from bulk solution of pH 5.0 at 60°C for the cross-section after 3 days exposure at 2000x magnification (a) SEM image, (b) carbon distribution map (c) iron map, and (d) oxygen map.....	102

Figure 40: Sample (C1018 spheroidized steel) for bulk solution pH 5.0 at 60°C (a) SEM image for the surface after 1 day exposure, (b) SEM image for the surface after two day exposure, (c) SEM image for the surface after 3 day exposure, (d) SEM image for the cross-section after 1 day exposure, (e) SEM image for the cross-section after two day exposure, and (f) SEM image for the cross-section after 3 day exposure105

Figure 41: Expected Fe₃C layer depth on C1018 spheroidized steel from bulk solution pH 5.0 at 60°C (a) SEM image for the cross-section after 1 day exposure, (b) SEM image for the cross-section after 2 day exposure, and (c) SEM image for the cross-section after 3 day exposure106

Figure 42: Microstructure of sample (C1018 spheroidized steel) for bulk solution pH 5.0 at 60°C for the cross-section after 3 days exposure (a) SEM image at 500x magnification , (b) SEM image at 1000x magnification, (c) SEM image at 2000x magnification, and (d) SEM image at 4000x magnification107

Figure 43: Elemental mapping of C1018 spheroidized steel sample surface after recovery from bulk solution of pH 5.0 at 60°C for the cross-section after 3 days exposure at 2000x magnification (a) SEM image, (b) carbon distribution map (c) iron map, and (d) oxygen map.....108

Figure 44: Sample (C1018 quenched-tempered steel) for bulk solution pH 5.0 at 60°C (a) SEM image for the surface after 1 day exposure, (b) SEM image for the surface after two day exposure, (c) SEM image for the surface after 3 day exposure, (d) SEM image for the cross-section after 1 day exposure, (e) SEM image for the cross-section after two day exposure, and (f) SEM image for the cross-section after 3 day exposure111

Figure 45: Microstructure of sample (C1018 quenched-tempered steel)) for bulk solution pH 5.0 at 60°C for the cross-section after 3 days exposure (a) SEM image at 500x magnification, (b) SEM image at 1000x magnification, (c) SEM image at 2000x magnification, and (d) SEM image at 4000x magnification.....112

Figure 46: Elemental mapping of C1018 quenched-tempered steel sample surface after recovery from bulk solution of pH 5.0 at 60°C for the cross-section after 3 days exposure at 2000x magnification (a) SEM image, (b) carbon distribution map (c) iron map, and (d) oxygen map.....113

Figure 47: Sample [X65 (0.14 wt.% C)] from bulk solution at pH 5.0 at 60°C (a) SEM image for the surface after 1 day exposure, (b) SEM image for the surface after two day exposure, (c) SEM image for the surface after 3 day exposure, (d) SEM image for the cross-section after 1 day exposure, (e) SEM image for the cross-section after two day exposure, and (f) SEM image for the cross-section after 3 day exposure116

Figure 48: Expected Fe₃C layer depth on X65 (0.14 wt.% C) from bulk solution pH 5.0 at 60°C (a) SEM image for the cross-section after 1 day exposure, (b) SEM image for the cross-section after 2 day exposure, and (c) SEM image for the cross-section after 3 day exposure117

Figure 49: Microstructure of X65 (0.14 wt.% C) recovered from bulk solution at pH 5.0 and 60°C for 3 days of exposure (a) SEM image of cross-section at 500 x magnifications, (b) SEM image at 1000x magnification, (c) SEM image at 2000x magnification, and (d) SEM image at 4000x magnification118

Figure 50: Elemental mapping of X65 (0.14 wt.% C) sample surface after recovery from bulk solution of pH 5.0 at 60°C for the cross-section after 3 days exposure at 2000x magnification (a) SEM image of cross-section, (b) carbon distribution map (c) iron map (d) oxygen map (e) manganese map, and (f) molybdenum map119

Figure 51: Sample [X65 (0.05 wt.% C)] from bulk solution at pH 5.0 at 60°C (a) SEM image for the surface after 1 day exposure, (b) SEM image for the surface after two day exposure, (c) SEM image for the surface after 3 day exposure, (d) SEM image for the cross-section after 1 day exposure, (e) SEM image for the cross-section after two day exposure, and (f) SEM image for the cross-section after 3 day exposure122

Figure 52: Expected Fe₃C layer depth on X65 (0.05 wt.% C) from bulk solution pH 5.0 at 60°C (a) SEM image for the cross-section after 1 day exposure, (b) SEM image for the cross-section after 2 day exposure, and (c) SEM image for the cross-section after 3 day exposure123

Figure 53: Microstructure of X65 (0.05 wt.% C) recovered from bulk solution at pH 5.0 and 60°C for 3 days of exposure (a) SEM image of cross-section at 500 x magnifications, (b) SEM image at 1000x magnification, (c) SEM image at 2000x magnification, and (d) SEM image at 4000x magnification124

Figure 54: Elemental mapping of X65 (0.05 wt.% C) sample surface after recovery from bulk solution of pH 5.0 at 60°C for the cross-section after 3 days exposure at 2000x magnification (a) SEM image of cross-section, (b) carbon distribution map (c) iron map (d) oxygen map (e) manganese map, and (f) molybdenum map125

- Figure 55: Raman analysis of sample [X65 (0.05 wt.% C)] from bulk solution at pH 5.0 at 60°C (a) Raman analysis for the surface after 1 day exposure, (b) Raman analysis for the surface after two day exposure, (c) Raman analysis for the surface after 3 day exposure127
- Figure 56: Sample [X65 (0.05 wt.% C)] spheroidized from bulk solution at pH 5.0 at 60°C (a) SEM image for the surface after 1 day exposure, (b) SEM image for the surface after two day exposure, (c) SEM image for the surface after 3 day exposure, (d) SEM image for the cross-section after 1 day exposure, (e) SEM image for the cross-section after two day exposure, and (f) SEM image for the cross-section after 3 day exposure130
- Figure 57: Expected Fe₃C layer depth on X65 (0.05 wt.% C) spheroidized from bulk solution pH 5.0 at 60°C (a) SEM image for the cross-section after 1 day exposure, (b) SEM image for the cross-section after 2 day exposure, and (c) SEM image for the cross-section after 3 day exposure.....131
- Figure 58: Microstructure of X65 (0.05 wt.% C) spheroidized recovered from bulk solution at pH 5.0 and 60°C for 3 days of exposure (a) SEM image of cross-section at 500 x magnifications, (b) SEM image at 1000x magnification, (c) SEM image at 2000x magnification, and (d) SEM image at 4000x magnification.....132
- Figure 59: Elemental mapping of X65 (0.05 wt.% C) spheroidized sample surface after recovery from bulk solution of pH 5.0 at 60°C for the cross-section after 3 days exposure at 2000x magnification (a) SEM image of cross-section, (b) carbon distribution map (c) iron map (d) oxygen map (e) manganese map, and (f) molybdenum map133
- Figure 60: Characteristic structure of an imidazoline-type inhibitor [40]

Figure 61: Corrosion rate vs. time for experiments conducted with C1018 ferrite-pearlite steel at pH 5.0 and 60°C for injection 72 ppm of imidazoline-type inhibitor	138
Figure 62: Corrosion rate vs. time for experiments conducted with C1018 spheroidized steel at pH 5.0 and 60°C for injection 72 ppm of imidazoline-type inhibitor	139
Figure 63: Corrosion rate vs. time for experiments conducted with C1018 quenched-tempered steel at pH 5.0 and 60°C for injection 72 ppm of imidazoline-type inhibitor	140
Figure 64: Corrosion rate vs. time for experiments conducted with X65 (0.14 wt.% C) steel at pH 5.0 and 60°C for injection 72 ppm of imidazoline-type inhibitor	141
Figure 65: Corrosion rate vs. time for experiments conducted with X65 (0.05 wt.% C) steel at pH 5.0 and 60°C for injection 72 ppm of imidazoline-type inhibitor	142
Figure 66: Corrosion rate vs. time for experiments conducted with X65 (0.05 wt.% C) spheroidized steel at pH 5.0 and 60°C for injection 72 ppm of imidazoline-type inhibitor	143
Figure 67: C1018 ferrite-pearlite steel samples recovered from bulk solution pH 5.0 at 60°C (a) SEM image for the surface after 1 day pre-corrosion, (b) SEM image for the surface after 1 day pre-corrosion and after 1 day inhibition, (c) SEM image for the surface after 1 day pre-corrosion and after 2 days inhibition, (d) SEM image for the cross-section after 1 day pre-corrosion, (e) SEM image for the cross-section after 1 day pre-corrosion and after 1 day inhibition, and (f) SEM image for the cross-section after 1 day pre-corrosion and after 2 days inhibition	146
Figure 68: Depth of Fe ₃ C without and with imidazoline-type inhibitor vs. time for experiments conducted at pH 5.0 and 60°C with C1018 ferrite-pearlite steel	147

Figure 69: C1018 spheroidized samples recovered from bulk solution pH 5.0 at 60°C (a) SEM image for the surface after 1 day pre-corrosion, (b) SEM image for the surface after 1 day pre-corrosion and after 1 day inhibition, (c) SEM image for the surface after 1 day pre-corrosion and after 2 days inhibition, (d) SEM image for the cross-section after 1 day pre-corrosion, (e) SEM image for the cross-section after 1 day pre-corrosion and after 1 day inhibition, and (f) SEM image for the cross-section after 1 day pre-corrosion and after 2 days inhibition150

Figure 70: Depth of Fe₃C without and with imidazoline-type inhibitor vs. time for experiments conducted at pH 5.0 and 60°C with C1018 spheroidized steel151

Figure 71: C1018 quenched-tempered steel samples recovered from bulk solution pH 5.0 at 60°C (a) SEM image for the surface after 1 day pre-corrosion, (b) SEM image for the surface after 1 day pre-corrosion and after 1 day inhibition, (c) SEM image for the surface after 1 day pre-corrosion and after 2 days inhibition, (d) SEM image for the cross-section after 1 day pre-corrosion, (e) SEM image for the cross-section after 1 day pre-corrosion and after 1 day inhibition, and (f) SEM image for the cross-section after 1 day pre-corrosion and after 2 days inhibition154

Figure 72: Depth of Fe₃C without and with imidazoline-type inhibitor vs. time for experiments conducted at pH 5.0 and 60°C with C1018 quenched-tempered steel155

Figure 73: X65 (0.14 wt.% C) samples recovered from bulk solution at pH 5 and 60°C (a) SEM image for the surface after 1 day pre-corrosion, (b) SEM image for the surface after 1 day pre-corrosion and after 1 day inhibition, (c) SEM image for the surface after 1 day pre-corrosion after 2 days inhibition, (d) SEM image for the cross-section after 1 day

pre-corroded, (e) SEM image for the cross-section after 1 day pre-corroded and after 1 day inhibition, and (f) SEM image for the cross-section after 1 day pre-corroded and after 2 days inhibition158

Figure 74: Depth of Fe₃C without and with imidazoline type inhibitor vs. time for experiments conducted at pH 5.0 and 60°C on X65 (0.14 wt. % C) steel.....159

Figure 75: X65 (0.05 wt.% C) samples recovered from bulk solution at pH 5 and 60°C (a) SEM image for the surface after 1 day pre-corrosion, (b) SEM image for the surface after 1 day pre-corrosion and after 1 day inhibition, (c) SEM image for the surface after 1 day pre-corrosion after 2 days inhibition, (d) SEM image for the cross-section after 1 day pre-corroded, (e) SEM image for the cross-section after 1 day pre-corroded and after 1 day inhibition, and (f) SEM image for the cross-section after 1 day pre-corroded and after 2 days inhibition162

Figure 76: Depth of Fe₃C without and with imidazoline type inhibitor vs. time for experiments conducted at pH 5.0 and 60°C on X65 (0.05 wt. % C) steel.....163

Figure 77: X65 (0.05 wt.% C) spheroidized samples recovered from bulk solution at pH 5 and 60°C (a) SEM image for the surface after 1 day pre-corrosion, (b) SEM image for the surface after 1 day pre-corrosion and after 1 day inhibition, (c) SEM image for the surface after 1 day pre-corrosion after 2 days inhibition, (d) SEM image for the cross-section after 1 day pre-corroded, (e) SEM image for the cross-section after 1 day pre-corroded and after 1 day inhibition, and (f) SEM image for the cross-section after 1 day pre-corroded and after 2 days inhibition.....167

Figure 78: Depth of Fe_3C without and with imidazoline type inhibitor vs. time for experiments conducted at pH 5.0 and 60°C on X65 (0.05 wt. % C) spheroidized steel168

Figure 79: Trend of corrosion inhibitor performance with steel type.....176

CHAPTER 1: INTRODUCTION

Corrosion causes dangerous and costly damage to drinking water systems, pipelines, bridges, public buildings, and infrastructure associated with the production of oil and gas. Failures in infrastructure for the production of oil and gas lead to a decline in the production rate, unscheduled shutdowns, environmental contamination, high repair costs, and fire accidents. These expensive damages are reflected in the cost of crude oil. In 2001, the direct cost of corrosion in the United States was reported to be \$276 billion on an annual basis [1].

Compared to the use of corrosion resistant materials, corrosion inhibitors used in combination with carbon steel can be an economic alternative for corrosion mitigation in oil and gas pipelines. However, how corrosion inhibitors behave under particular environmental conditions may not be well understood. Consequently, under operational conditions for pipeline transmission systems, corrosion inhibitors do not always perform as expected [2]. Therefore, research that sheds light on factors that affect inhibitor performance, as well as mechanistic phenomena thereof, is of great importance regarding the design, qualification, and choice of inhibitors.

In the laboratory, newly polished steel samples are typically used to test corrosion inhibitors for mitigation of carbon dioxide (CO₂) corrosion [3]. On the other hand, in production environments encountered in the field, steel surfaces inside operating pipelines are covered with different types of corrosion product layers or deposited scales, such as residual iron carbide, precipitated iron carbonate, iron sulfides, calcium carbonate, etc. Consequently, applied inhibitors may encounter surface layers that have

the potential to significantly affect inhibitor adsorption and performance. There is limited peer reviewed literature on this subject, and is often somewhat contradictory. Kowata and Takahashi reported that corrosion inhibitors can penetrate deep through generated corrosion product layers [4]. Also, inhibitors are able to generate a protective barrier on the steel surface against corrosive agents. Papavinasam further discussed layer porosity, discussing the role of pore size in inhibitor migration [5]. Kapusta, *et al.*, reported that 1 day of pre-corrosion had a negative influence on the performance of the inhibitor [6]. However, Hausler, *et al.*, reported that, at a high CO₂ partial pressure and elevated temperature, four days of pre-corrosion had an insignificant influence on the performance of the inhibitor [7] - [8]. In addition, Gulbrandsen and Nestic reported that certain oil soluble corrosion inhibitors worked better with pre-corroded surfaces [3]. Therefore, studies investigating the performance of an inhibitor should always be accompanied by examinations of the metal surface and corrosion product layer or scale. The purpose of the proposed research project is to focus on the effect of residual iron carbide derived from CO₂ corrosion of steel on inhibitor performance.

CHAPTER 2: LITERATURE REVIEW

Once mild steel is exposed to CO₂ environments it can rapidly corrode. In order to understand CO₂ corrosion mechanisms for mild steel there are many factors that merit consideration. These factors are concisely described below [9], [10], [11], [12].

2.1 CO₂ Corrosion

The chemical reactions of species in bulk solution, electrochemical reactions of species on the steel surface, and mass transport of species from bulk solution to and away from the steel surface are each used to describe the CO₂ corrosion process; each of these key factors are described below [10].

2.1.1 Chemical Reactions

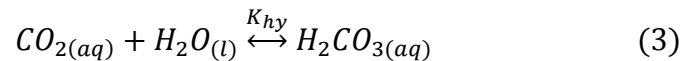
One of the important parameters that govern CO₂ corrosion is water chemistry. Once carbon dioxide (CO₂) is dissolved in water, it can be described as aqueous CO₂ [10]:



K_{CO_2} denotes the temperature dependent solubility constant of the, defined as follows:

$$K_{CO_2} = \frac{[CO_2]}{pCO_2} \quad (2)$$

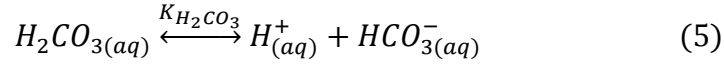
This dissolved CO₂ partially hydrates to form carbonic acid(H_2CO_3):



K_{hy} denotes the corresponding equilibrium constant for hydration defined as:

$$K_{hy} = \frac{[H_2CO_3]}{[CO_2]} \quad (4)$$

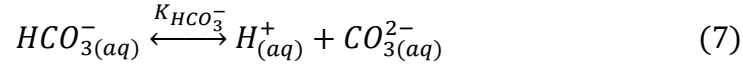
The produced H_2CO_3 then partly dissociates to form a hydrogen ion (H^+) and a bicarbonate ion (HCO_3^-):



$K_{H_2CO_3}$ denotes the equilibrium constant of the reaction, defined as:

$$K_{H_2CO_3} = \frac{[H^+]. [HCO_3^-]}{[H_2CO_3]} \quad (6)$$

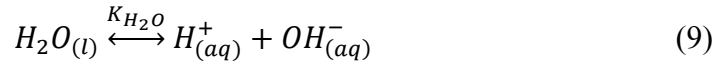
The HCO_3^- partially dissociates to form carbonate anions (CO_3^{2-}) hydrogen ions (H^+):



Where $K_{HCO_3^-}$ denotes the equilibrium constant, defined as:

$$K_{HCO_3^-} = \frac{[H^+]. [CO_3^{2-}]}{[HCO_3^-]} \quad (8)$$

Dissociation of water is another source of hydrogen ions(H^+):



K_{H_2O} denotes the equilibrium constant, defined as:

$$K_{H_2O} = [H^+]. [OH^-] \quad (10)$$

Combinations of these reactions dictate the concentrations of each species in aqueous solution and their availability for participation in electrochemical reactions.

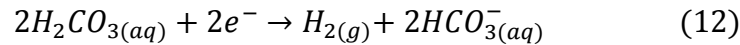
2.1.2 Electrochemical Reactions

The electrochemical reactions take place on the steel surface. These reactions include the cathodic evolution of hydrogen (reduction) and the anodic dissolution of iron (oxidation). The reduction processes are described by the following half-reactions [10]:

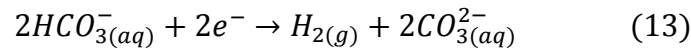
- (1) The cathodic evolution of hydrogen ions occurs due to reduction of hydrogen ions generated by the partial dissociation of carbonic acid (H_2CO_3), bicarbonate ion (HCO_3^-), and water (H_2O), as presented by the equilibrium reactions (5), (7) and (9).



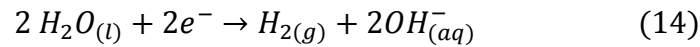
- (2) The direct cathodic reduction of carbonic acid (H_2CO_3).



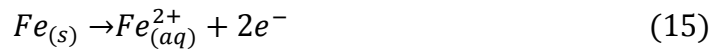
- (3) The direct cathodic reduction of the bicarbonate (HCO_3^-), the dominant species at near neutral pH [12].



The direct cathodic reduction of water (H_2O), if $pH > 6$ and partial pressure of CO_2 (pCO_2) $\ll 1$ this reaction is significant [13] :



The oxidative dissolution of iron is always the accompanying anodic half-reaction in anoxic acid corrosion environments.



2.1.3 Mass Transport

The rate of the electrochemical reaction is controlled by the mass transport rates of the reducible species and dissolved metal ions, which move to and away from the steel surface. In the corrosion process, as a result of the turbulent flow of the solution near the metal surface, mass transport takes place *via* molecular diffusion, within a diffusion boundary layer, and *via* convection [10].

In the CO₂ corrosion process, reducible hydrogen ion is consumed at the steel surface as described in Equation 11. Simultaneously, ferrous ion concentration increases as shown in Equation 15. As a result, the mass transport of reducible hydrogen ions to the steel surface governs and restricts the process. The metal reacts with carbonic acid, as shown in Equation 12, and bicarbonate ion, as described in Equation 13; overall this corresponds to the release/consumption of electrons in the corrosion process. Mass transport affects carbonic acid and bicarbonate ions. However, the chemical reaction to produce carbonic acid is the rate-determining step for these two species because the diffusion rate is faster than the chemical reaction of the dissolved CO₂ to produce the carbonic acid, described in Equation 3 [10].

2.1.4 Corrosion Product as Iron Carbonate

Dissolved ferrous ions (Fe²⁺) react with the carbonate anions (CO₃²⁻), which form by the dissociation processes as described in Equation 13, to produce iron carbonate (FeCO₃) as a corrosion product, or deposited scale. This iron carbonate heterogeneously precipitates at the steel surface. Also, the protectiveness of the iron carbonate against the corrosion process is reliant on the precipitation rate. In general, an adherent and dense iron carbonate layer is able to form on the steel surface when the precipitation/formation rate of iron carbonate on the steel surface exceeds the corrosion rate, the oxidative dissolution of iron [11], [12], [14], [15]. The CO₂ pressure and temperature are factors upon which the precipitation rate of the iron carbonate is also dependent. The saturation value (S (FeCO₃)) of the iron carbonate directly affects the precipitation rate, as defined by Equation 16:

$$S(\text{FeCO}_3) = \frac{[\text{Fe}^{2+}] * [\text{CO}_3^{2-}]}{K_{\text{sp}_{\text{FeCO}_3}}} \quad (16)$$

Where:

$[\text{Fe}^{2+}]$ represents measured ferrous ion concentration in the bulk solution.

$[\text{CO}_3^{2-}]$ represents the equilibrium concentration of carbonate ions, which is straightforwardly related to the solution pH by Equation 7.

$K_{\text{sp}_{\text{FeCO}_3}}$ represents the solubility product for iron carbonate, which is a function of ionic strength and temperature [10], [11]. The saturation level, $S(\text{FeCO}_3)$, is termed undersaturated when less than one and supersaturated when greater than one. When the supersaturation of iron carbonate is achieved, this can lead to the formation of an adherent and dense FeCO_3 layer.

2.2 Effects of Flow

The effect of flow on CO_2 corrosion is reliant on the condition of the steel surface. For example, turbulent movement leads to an increase in the rate of species transport from and towards the steel surface. As an example, iron carbonate layer cannot form on the steel surface when the FeCO_3 saturation is less than unity $S < 1$ (at pH 4 for example) [9], [10]. At this condition, fast flow of species increases the rate at which H^+ is replenished and Fe^{2+} is removed from the surface. Consequently, such flow leads to increases in corrosion rate as long as mass transfer is the limiting step. The effect of flow is insignificant when iron carbonate is produced on the steel surface at high pH (pH > 6.5), where the saturation level is greater than the saturation limit [9].

An iron carbonate layer does not form on the steel surface at pH 4 when the saturation level is less than the saturation limit, $S < 1$, [9], [10]. At this condition, fast flow of species increases the rate at which H^+ is replenished and generated Fe^{2+} is removed from the surface. Consequently, such flow leads to increases in corrosion rate. The effect of flow is insignificant when iron carbonate is produced on the steel surface at $pH > 5$, where the saturation level is greater than the saturation limit [9]. On the other hand, the effects of flow enable breakdown of the iron carbonate corrosion product layer, or scale, that is particularly deleterious at turbulent local areas such as bends, valves, and expansions [16], [17].

2.3 Effects of Steel Composition and Microstructure

In the oil and gas industry design criteria for pipeline materials are mainly concentrated on mechanical properties, such as toughness, weldability, and strength, rather than resistance to corrosion [18]. The microstructure of steel depends on its chemical composition and processing, particularly heat treatment and rolling [19], [20]. The microstructure governs the mechanical properties of pipeline materials. Also, the microstructure of the steel has a significant influence on generated iron carbide characteristics, nucleation and growth of iron carbonate as a corrosion product, and inhibitor layer/film characteristics in CO_2 environments [19], [20].

2.3.1 Corroding Substrate as an Exposed Steel

In CO_2 environments, if the saturation limit of iron carbonate in the bulk solution is sufficiently high, the iron carbonate layer can form as a corrosion product [11], [12]. Such a layer can be adherent, but may not be protective. For diverse steels with the same

mechanical properties, lab experiments and field experience show that degree of protectiveness and adherence of this iron carbonate can differ [21], [22]. Many researchers reported that quenched and tempered steels, with a tempered martensite microstructure, performed differently from normalized steels with ferritic-pearlitic microstructure in terms of growth/protectiveness of corrosion product [15], [21], [23], [24]. Carbides are considered to play a major role governing the properties, protectiveness and adherence of corrosion products. In fact, the iron carbide phase supports the iron carbonate layer and anchors it to the surface of the steel. Therefore, the morphological characteristics of generated iron carbide are a significant factor that needs to be considered in the study of steel corrosion.

In the ferritic-pearlitic steels, the pearlite component is a lamellar structure constituted of alternate layers of iron carbide (cementite) and ferrite. The ferrite becomes anodic, and rapidly corrodes when such a steel is exposed to the CO₂ environment. However, the cementite lamellae remain attached to the surface of the corroded steel. Once the ferrous ion concentration is high enough to achieve supersaturation condition in aqueous CO₂ and the flow becomes stagnant and diffusion limited, such as in the cavities between iron carbide lamellae, the iron carbonate layer rapidly forms. Thus, cementite lamellae facilitates iron carbonate growth and adherence on the steel surface, as shown in Figure 1.

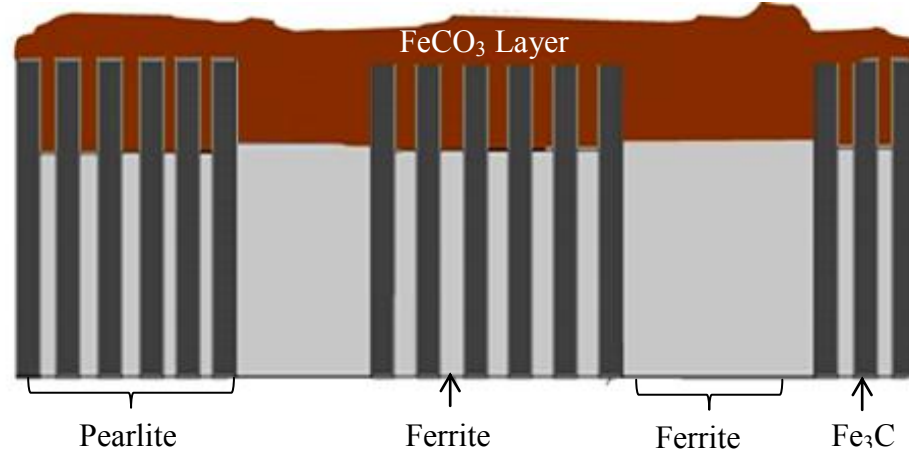


Figure 1. Iron carbonate development on ferritic-pearlitic steels (figure adapted from Akeer's PhD dissertation) [25].

The characteristics of the ferritic-pearlitic microstructure have an important effect on steel performance in CO₂ corrosion. The steel performance will be impaired when the ferritic-pearlitic steel is heterogeneous, *i.e.*, consists primarily of ferrite grains with pearlite. Increasing carbon content and normalizing heat treatment, to yield a more homogeneous alloy, can improve the performance of a J55 steel of ferritic-pearlitic type [26]. This study also reported that increasing the content of carbon gives steel with homogeneous and fine globular grains, which is more protective than the banded ferritic-pearlitic structure.

Corrosion, and related phenomena, for martensitic quenched and tempered steels are still poorly understood. Martensitic quenched and tempered steel has fine grains. It is difficult to determine its microstructure by optical microscopy because of the dominance of such fine grains; however, use of higher magnification electron microscopy can help to determine its microstructure. The ratio of pearlite to ferrite in normalized steel is reliant

on the content of the carbon, but steels with relatively more uniform martensitic microstructures can form at much lower carbon concentrations [21]. This study also surmised that there is no obvious understanding about how the microstructural characteristics of quenched and tempered martensitic steels impact the development of the iron carbonate layer [21]. Also, the study reported that the corrosion rate of quenched and tempered steels with larger spheroidal carbides is lower than for those with a large population of small grain carbides. Once again, the study reported that the large number of small grain carbides could attached on the surface of the corroded samples and lead to formation of non-protective iron carbonate layers with exposed, and conductive, iron carbides [21]. Also, the study showed that the corrosion rates for quenched and tempered steels having no iron carbides are the lowest; however, it did not provide an obvious explanation about how the iron carbonate attached to the surface of the corroded steel. Another study discussed the influence of supersaturation of FeCO_3 over a range of Fe^{2+} and CO_3^{2-} concentrations on a martensitic X65 steel at 25°C and higher pH ($\text{pH} > 6.8$) with respect to iron carbonate formation, without respect to its microstructure [27]. This study hypothesized that the relative inability to form protective iron carbonate layers under such conditions could be attributed to the absence of an iron carbide effect when pearlite is not present.

From these brief literature observations, the size of ferrite and pearlite grains, and also the size, shape, and distribution of iron carbides in the steel, could be considered as significant factors that affect corrosion processes. Therefore, the main factors that need to be considered are heat treatment, mechanical properties, and chemical composition of the

steel in order to control the iron carbide formation on mild steel. Also, another significant factor that needs to be considered is the steel surface condition, such as freshly polished or corroded samples.

2.3.2 Corrosion Inhibitors and Metallurgical Characteristics

The most effective method to control corrosion of mild steel in the oil and gas industry is the use of corrosion inhibitors, including surface-active compounds that favorably adsorb on the steel surface. The mechanism of inhibitor adsorption is still not well understood. Gulbrandsen, *et al.*, reported that if the structure of the steel is primarily cementite-type rather than ferrite, the efficiency of the corrosion inhibitor could be detrimentally affected [2]. However, the authors also reported that the efficiency of the inhibitor is higher on a fresh steel surface. Also, the study reported that iron carbides would be increasingly exposed once mild steel is corroded. More exposed iron carbide leads to an increase in the cathodic area. In addition, if the actual type of mild steel is unaccounted for, the large cathodic areas negatively affect the efficiency of the inhibitor. Another study reported that the efficiency of inhibitor could be negatively affected when the content of chromium (Cr) is increased [9]. Also, this study stated that one reason for the poor performance of inhibitors could be chromium enrichment of the FeCO_3 layers and the inhomogeneous distribution of chromium in ferrite and pearlite [9].

2.4 Corrosion Product

In CO_2 corrosion, formed layers on the steel surface are derived from the steel. These layers have significant effects on corrosion mechanisms, being able to increase or decrease the corrosion rate due to their composition, location, morphology and

physicochemical characteristics. Predicting corrosion rate can be difficult due to these complicating factors relating to layer properties. Furthermore, there are other environmental parameters, such as temperature, CO₂ partial pressure, flow rate and pH of electrolyte that may further affect the formation and behavior of corrosion product layers [28]. In CO₂ corrosion of mild steel, there are four forms of corrosion product layers that are produced at temperatures ranging from 5°C to 150°C. These four layer types are “iron oxide”, “iron carbide”, “iron carbonate”, and “iron carbonate plus iron carbide”. [28] The iron oxide layer often appears as a “tarnish” on the steel surface and contains iron and oxygen approximately in the ratio of 1:2, not unlike a passive film. An “iron carbide”, or cementite, layer is generated *via* selective oxidative dissolution of ferrite from steel. An “iron carbonate” layer nucleates and grows at the steel surface from ferrous ion generated during the corrosion process. A mixed “iron carbonate plus iron carbide” layer has the potential to occur given appropriate conditions and microstructural characteristics. Therefore, understanding the nature of iron carbide and how it is present in a steel microstructure will be of key importance to understanding how a corrosion product layer forms and, potentially, its interactions with corrosion inhibitors.

2.4.1 Iron Carbide Layer (Cementite)

Iron carbide (cementite) consists of 6.7 wt.% carbon and 93.3 wt.% iron, thus it has a chemical formula of Fe₃C [29]. Dissolved ferrous ions are formed by anodic dissolution of ferrite in carbon steel. An iron carbide layer is left over at the steel surface as a result of this selective oxidation process. Therefore, iron carbide is not a corrosion product per se, but rather it is a residual material derived from the carbon steel after the

ferrous ion is released into solution from the oxidized ferrite [30]. The generated iron carbide layer is porous and relatively fragile; therefore, it is liable to be damaged by flow. Given that it is uncorroded material, it has the potential to generate a porous network on the metal surface associated with an appropriate initial steel microstructure [28]. At low temperature and pressure in multiphase flow conditions, it has been previously reported that such a corrosion product/layer is unprotective [31].

2.4.2 Effect of Steel Microstructure and Composition on the Structure of Iron Carbide

The structure of iron carbide relies upon the chemical composition and microstructure of the carbon steel from which it is derived. A previous study established that once a ferritic-pearlitic microstructure steel has been corroded, lamellar cementite remains [32]. Similarly, when a quenched and tempered martensitic steel is corroded, a dispersed-cementite results. This means that various carbide structures have divergent properties for the anchoring of corrosion product layers. Due to the fact that lamellar carbides contain cavities that permit the development of local aqueous conditions that favor FeCO_3 nucleation and crystal growth, mild steels with such structures can be hypothesized to undergo less severe corrosion when compared to mild steels with dispersed-carbide structures. Essentially, porosity/cavities in carbide residues are more capable of initiating and sustaining the growth of corrosion product layers due to development of local supersaturation conditions. Consequently, growth and stability of the corrosion product layer is enhanced due to such microstructural features [32].

2.4.3 Effect of Iron Carbide on the Corrosion Rate

Many investigations have been conducted to research the influence of cementite on corrosion rate. Kermani and Morshed reported that the presence of residual iron carbide on the metal surface increases the severity of the corrosion process [9]. This gradual enrichment of a steel surface with a porous and uncorroded iron carbide layer could be the reason for the increase in the corrosion rate during pre-corrosion [3]. A later study reported that the iron carbide layer is an electronic conductor as well as a very efficient substrate for hydrogen evolution in acidic solutions[33]. The iron carbide layer is itself resistant to corrosion but non-protective to the underlying steel [30]; iron carbide remains on the surface of the steel when the ferrite component corrodes. This iron carbide provides an additional surface area for the cathodic reaction. Eventually, these layers are undermined by corrosion and lose electrical contact with the steel [2, 3].

2.5 Inhibitors

In the production of oil and gas, a well-known phenomenon and a serious problem is the corrosion of carbon steel pipelines. Also, the most cost effective method used to control corrosion is inhibition. For these reasons, much research has been dedicated to investigate the mechanism of the corrosion inhibition with particular regard to the design and suitable choice of inhibitors. Corrosion inhibitors are able to interfere with cathodic or anodic reactions. Also, inhibitors are able to generate a protective barrier on the steel surface against corrosive agents. In general, inhibitors are able to work by a combination of interfering with a cathodic (or an anodic) reaction and generating a protective barrier on the steel surface. Adsorption of inhibitor molecules at the steel-solution interface

happens when the inhibitor is added. A change in potential difference between the solution and the metal surface simultaneously accompanies this adsorption. This change in potential happens because of the non-uniform distribution of electrical charges at the interface. There are many factors that affect the efficiency of the inhibitor. In the macroscopic view, the efficiency of inhibitors relies on temperature, pressure, solution chemistry, etc. At the molecular level, the efficiency of inhibitors relies on molecular geometry, mode of interaction with the metal surface, the number of adsorption sites, electronic structure of the molecules, inhibitor charge density, etc. [5], [31].

2.5.1 Effect of the Iron Carbide Layer on Inhibitor Performance

Iron carbide also has an effect on the performance of the corrosion inhibitor applied to carbon steels. It was reported that the longer the pre-corrosion time, the thicker the iron carbide layer becomes [3]. Consequently, the thickness of iron carbide impaired the inhibitor performance. The reason is that the iron carbide layer acts as a barrier preventing the transfer of the inhibitor to the active steel surface below. Also, this study has reported that when the iron carbide layer was removed by a brush, the performance of the inhibitor improved.

2.5.2 Effect of Chemical Composition on Corrosion Rate and Inhibitor Performance

In CO₂ environments, chemical composition has a significant effect on the corrosion of carbon steels. A study has reported that the efficiency of the inhibitor ranged from 84 to 98% [2]. Also, this study reported that differences in the amount of carbon (in pearlite) and copper in the steel resulted in variations in the efficiency of the inhibitor. It has also been reported that molybdenum (Mo) has a positive effect that helps to decrease

the corrosion rate of carbon steels[34]. Another study showed that trace amounts of copper (Cu), nickel (Ni), chromium (Cr), and possibly (Mo) enhance the corrosion potential of carbon steels, making it more noble [35]. On the other hand, a study mentioned that addition of copper (Cu) may possibly have an effect on the inhibitor efficiency [2]. In CO₂ environments, the sulfur (S) content of carbon steels seems to have an effect on the corrosion rate as well, as reported in a laboratory study. In addition, in low-shear-stirred CO₂ corrosion tests, low sulfur content of carbon steels have a higher corrosion rate than certain high sulfur content carbon steels [28].

CHAPTER 3: HYPOTHESES AND RESEARCH OBJECTIVES

3.1 Hypotheses

In order to study the effect of iron carbide on inhibitor performance, the following hypotheses will be tested:

1. The difference between X65 and C1018 steels, namely the size and morphology of the cementite layer, are expected to lead to variation in inhibitor performance on pre-corroded specimens.
 - a. When ferrite with discrete cementite particles in the steel microstructure is corroded, discrete cementite particles will become unattached and be removed. This permits ready attachment of inhibitor to the active steel surface. This corrosion process is illustrated schematically in Figure 2 (a) and (b).
 - b. In contrast, once the ferritic-pearlitic microstructured steel is corroded, attached lamellar cementite remains. This process is illustrated schematically in Figure 2 (c) and (d). This layer will have more of an effect on inhibitor performance compared to when discrete cementite particles are present due to the fact that the lamellar carbide structure will act as a diffusion barrier. Consequently, this lamellar cementite layer prevents the inhibitor to transfer to the active steel surface, thus impairing inhibitor performance.
2. Thick iron carbide layers will generate a barrier that prevents the transfer of the inhibitor compounds to the active surface of the steel leading to a decrease in the inhibitor performance.

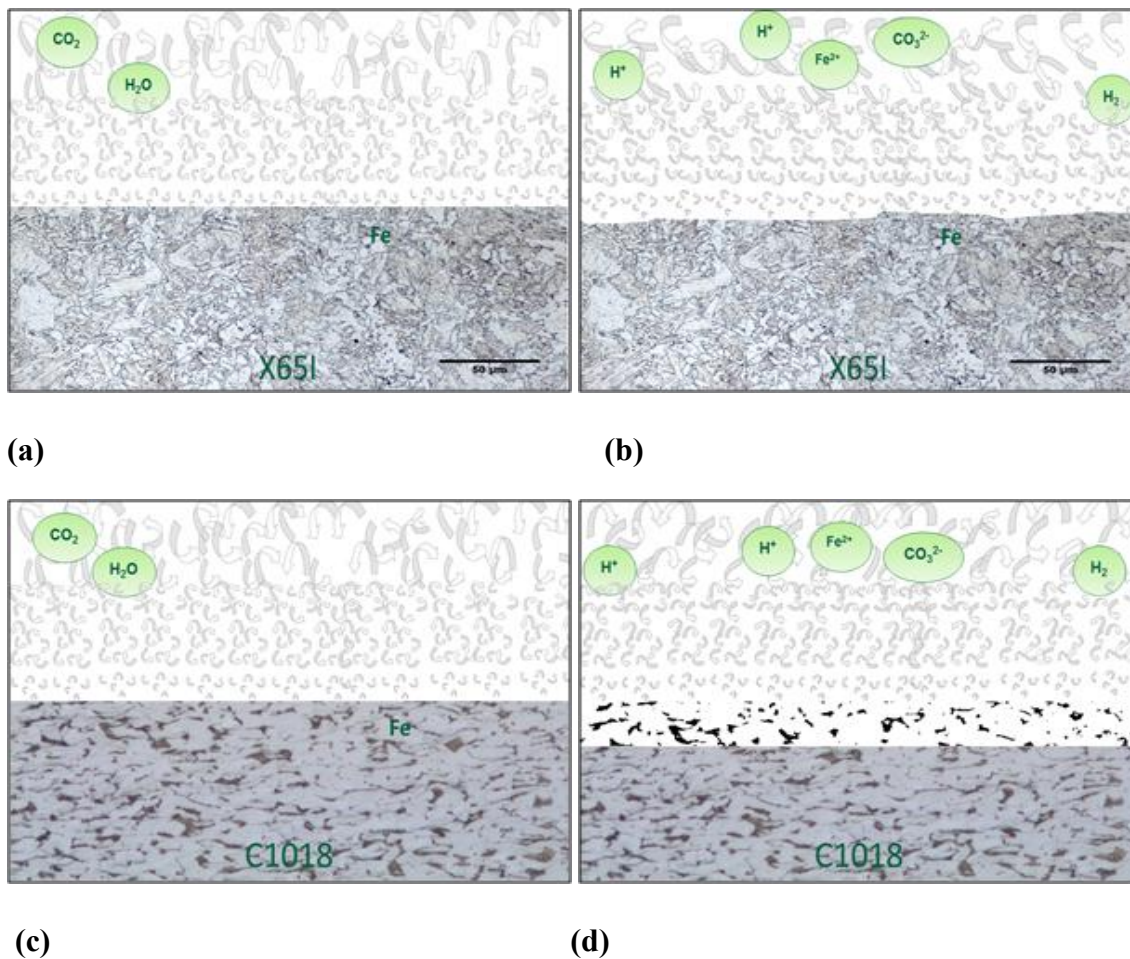


Figure 2. Schematic drawing of different microstructures: (a) sample of ferretic-discrete cementite microstructure (b) sample of a corroded ferretic-discrete cementite microstructure (c) sample of ferretic-pearlitic microstructure and arrow showing corroded sample anchored carbide lamellae (d) sample of a corroded ferretic-pearlitic microstructure and arrow showing corroded sample anchored carbide lamellae.

3.2 Research Objective

This research is important because several types of mild steel are used in pipeline transmission. Steels with similar mechanical properties, e.g., yield strengths, may have different contents and structures of iron carbide. This is hypothesized to lead to different corrosion behaviors and corrosion inhibitor performance. The primary objective of this study is to develop an understanding of how iron carbide layers, derived from the different microstructures of carbon steels during corrosion, affect corrosion behavior and inhibitor performance.

3.3 Methodology

The hypotheses will be tested as follows:

1- Establish repeatable test conditions for generation, or otherwise, of residual Fe_3C at corroding steel surfaces:

- a. pH 6.0 at different temperatures.
- b. 60°C at different pH values.

2- Investigation of Fe_3C characteristics, if present, related to the microstructure of the material:

The goal of this step is to use different steels (X65, C1018, and thermally treated C1018, X65) with different iron carbide types in order to observe and measure the difference between virgin and heat treated X65 and C1018 steels with respect to thickness and morphology of the cementite layer developed during corrosion.

3- Investigation of the effect of residual Fe_3C on inhibitor performance:

The goal of this step is to observe and measure the difference between X65, C1018, and thermally treated C1018, X65 steels with respect to iron carbide development and the variation in inhibitor performance on pre-corroded specimens.

Weight loss and electrochemical measurement will be used to determine the corrosion rate. Scanning electron microscopy will be used to characterize cementite layers on corroded steel surfaces.

CHAPTER 4: METALLOGRAPHIC ANALYSIS

4.1 Introduction

Any steel is termed mild steel or low carbon steel when it has a carbon content between 0.02 wt.% and 0.3 wt.% [36]. The chemical composition and/or the type of manufacturing and heat treatment, particularly mechanical and thermodynamic processes, have to be determined in order to understand the microstructure of any steel. Figure 3 shows the phase diagram of the iron-carbon system [36]. Fundamentally, a phase is a physically homogeneous part of a material system. Iron and carbon are not completely soluble in each other when they are added together in an alloy. They create separate phases, as shown in Figure 3. This is due to atomic radii differences as well as differences in crystal structure. In addition, phase diagrams tell which phases are present at a given temperature, which is on the y -axis, and a given nominal or overall composition of carbon content, which is on the x -axis. The phase diagram is a map that tells at any temperature and nominal composition three things: which phases are present, the chemical composition of each phase or phases, and their weight (or mole) fractions. Most alloys have two or more phases because this improves their mechanical properties are improved. That is one reason why phase diagrams are an essential tool in metallurgy.

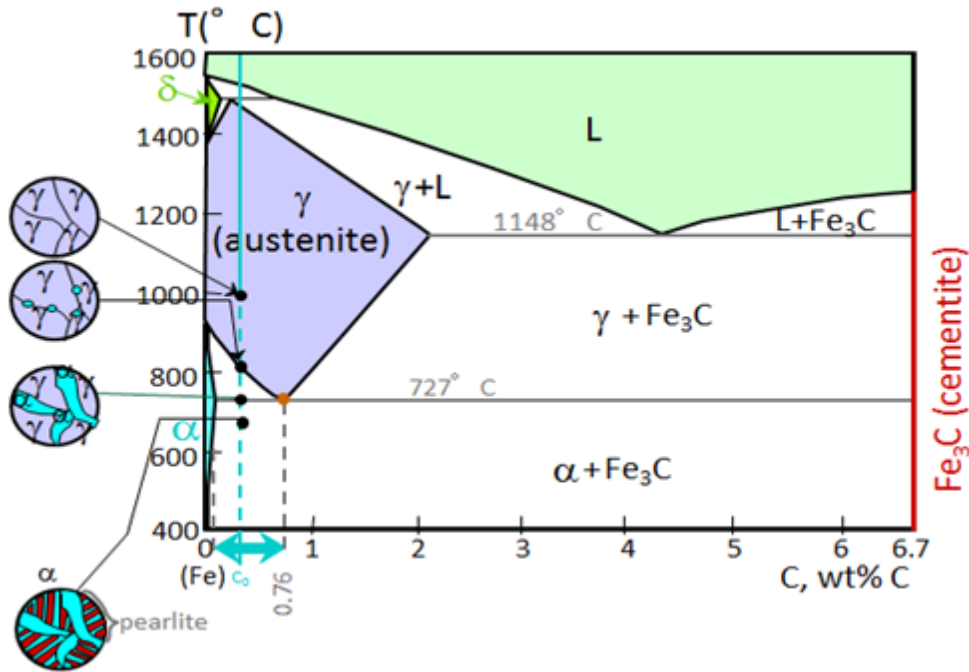


Figure 3. The Fe-Fe₃C diagram, a portion of the Fe₃C diagram, and the evolution of the microstructure of hypoeutectoid steels during a cooling process (This material is reproduced with permissions of John Wiley and Sons, Inc.) [37].

As pipeline steels have different chemical compositions, they have different mechanical properties and are categorized into particular grades [36]. Chemical composition and heat treatment of steels are the key factors that affect the formation of the microstructure of the steels. Controlling the cooling rate and thermal treatment of hot steel from the austenite temperature can yield many different microstructures, such as ferrite-pearlite, spheroidized, bainite, martensite, and tempered martensite. The type of heat treatment, termed as full annealing, process annealing, normalizing, spheroidizing, quenching, and quenching/tempering used to achieve a desired microstructure is determined by controlling the thermal processing [36].

Upon initial solidification, see Figure 3, iron or low carbon steel will form a body-centered cubic (BCC) structure; this is called δ -ferrite (delta-ferrite). On further cooling, the delta ferrite will be transformed to a face-centered cubic (FCC) unit cell, which is called austenite or γ -iron (gamma iron) [36]. For mild steel, or low carbon steel, austenite is the phase that is present above the critical eutectoid temperature A_3 , as shown in Figure 4. The austenite phase will be transformed back to a BCC unit cell structure to become alpha-ferrite, α -Fe, when austenite is cooled below the critical eutectoid temperature A_3 [36]. At 1,146 °C, the austenite (γ) is able to dissolve as much as 2.04 % by mass carbon. For steels with less than 0.76 wt.% C, ferrite grains start to nucleate and grow usually at grain boundaries when the austenite cools to below the A_3 transformation point. The remaining austenite is surrounded by ferrite and becomes progressively richer in carbon. Finally, remaining austenite will be transformed to pearlite when the cooling temperature reaches the A_1 transformation line at 727°C; this corresponds to eutectoid point for transformation of γ -Fe to α -Fe and Fe_3C . In the part of Figure 4 depicting slow cooling in air, the light grains represent ferrite and the banded grains represent pearlite [36]. Pearlite is defined as alternating lamellae of ferrite and iron carbide (Fe_3C). On the other hand, the austenite will not have enough time to transform into ferrite and pearlite when the steel is rapidly cooled from austenite, which is known as the quenching technique. This is shown in the part of Figure 4 depicting fast cooling. Instead of transforming to ferrite and pearlite, the austenite will transform to the martensite structure [36]. Martensite has a body centered tetragonal (BCT) unit cell that is capable of having

a higher content of carbon than α -Fe. Consequently, cooling rates are also a key factor that governs alloy microstructure and mechanical properties.

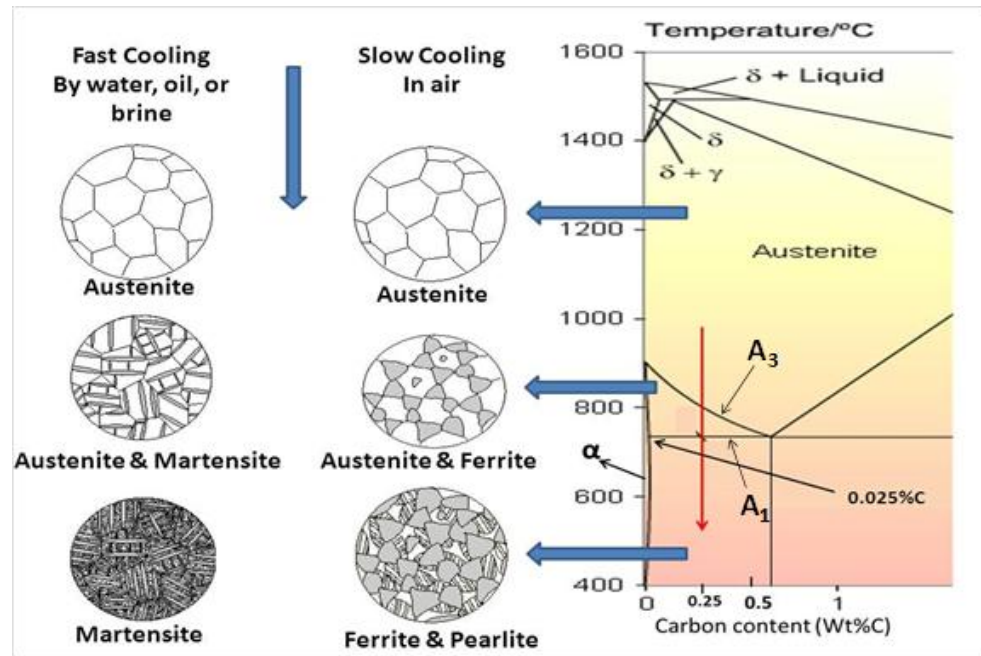


Figure 4. Fe-C phase diagram of the phase transformation from austenite to ferrite/pearlite (slow cooling) and from austenite to martensite (fast cooling) [38].

In order to determine the steel microstructure during cooling from austenite, continuous cooling transformation (CCT) diagrams are created. These diagrams determine the steel structure at various temperatures with respect to time for alloys with particular chemical compositions. The needed microstructure of the steel, which could be ferrite/pearlite at low cooling rates, bainite at medium cooling rates, and/or martensite at fast cooling rates, is determined by the cooling rate of steel. In addition, the carbon

content (wt.% C) and, for example, the molybdenum content (wt.% Mo) of the steel significantly impact the CCT diagram.

The transformation curves shown in the CCT diagrams are shifted to the right side when wt.% C and wt.% Mo are increased. During a continuous fast cooling rate, the structure of 0.4 wt.% C steel transforms from austenite to martensite as shown in Figure 5 and Figure 6 [39]. This type of cooling is called the quenching technique.

Oil, water, or brine is used to rapidly cool the steel after the temperature is increased to about 50°C above A3. The desired martensitic microstructure is nucleated dependent on the carbon content of the steel. During a continuous slow cooling rate, the structure of 0.4 wt. % C steel transforms from austenite to ferrite/pearlite as shown in Figure 7 and Figure 8. This type of cooling is called the normalizing technique. Air is used to slowly cool the steel after the temperature is increased to about 50°C above A3.

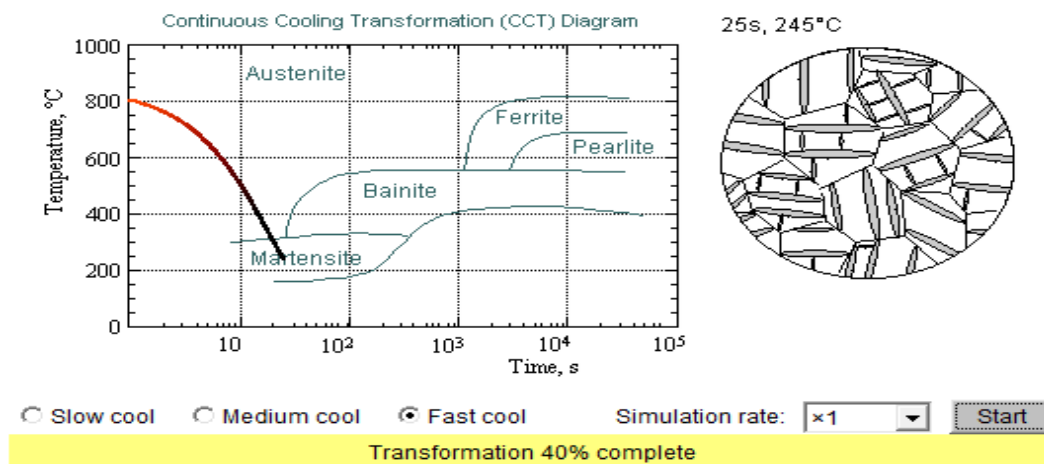


Figure 5. CCT diagram of the phase transformation of 0.4 wt.% C, 1.5 wt.% Mn, and 0.5 wt.% Mo steel from austenite to martensite in the fast cooling processes (figure reproduced with permission) [39].

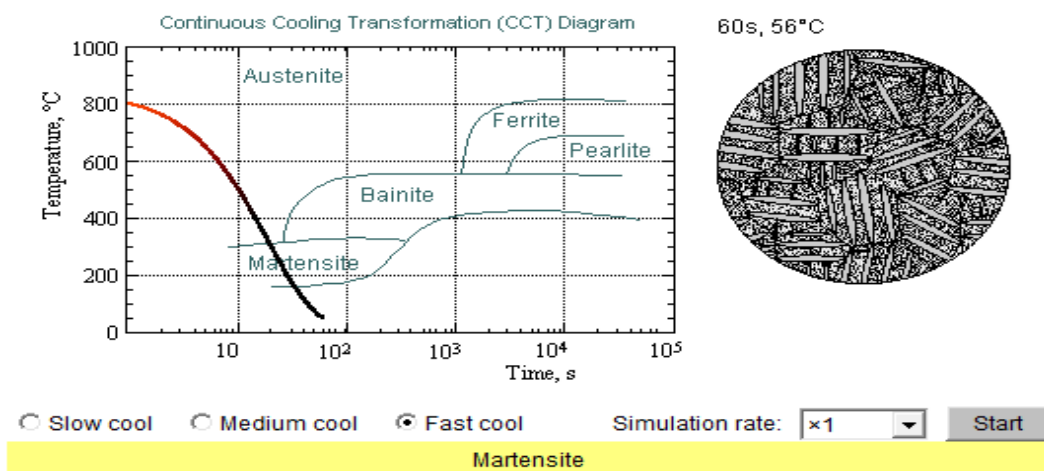


Figure 6. CCT diagram of the final obtained microstructure (martensite) of 0.4 wt.% C, 1.5 wt.% Mn, and 0.5 wt.% Mo steel in the fast cooling processes (figure reproduced with permission) [39].

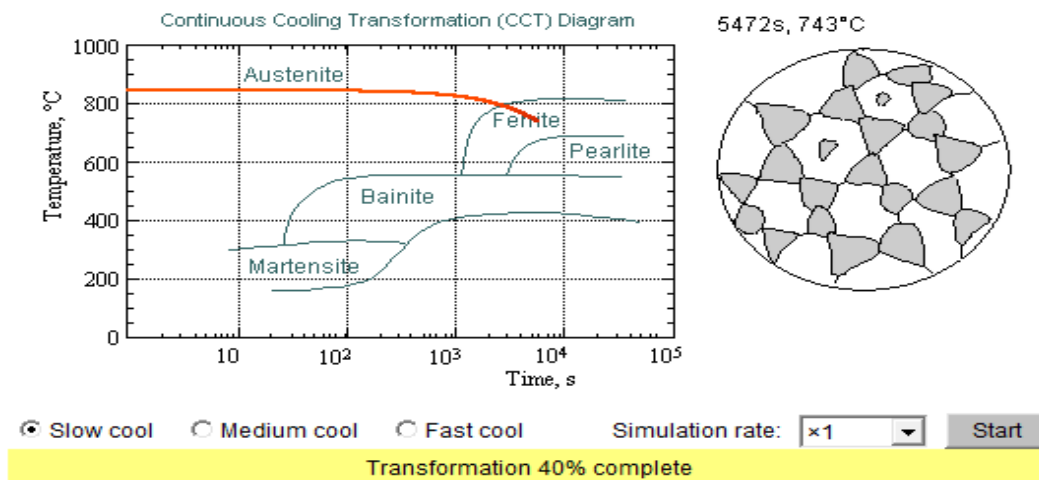


Figure 7. CCT diagram of the phase transformation of 0.4 wt.% C, 1.5 wt.% Mn, and 0.5 wt.% Mo steel from austenite to ferrite in the slow cooling processes (figure reproduced with permission) [39].

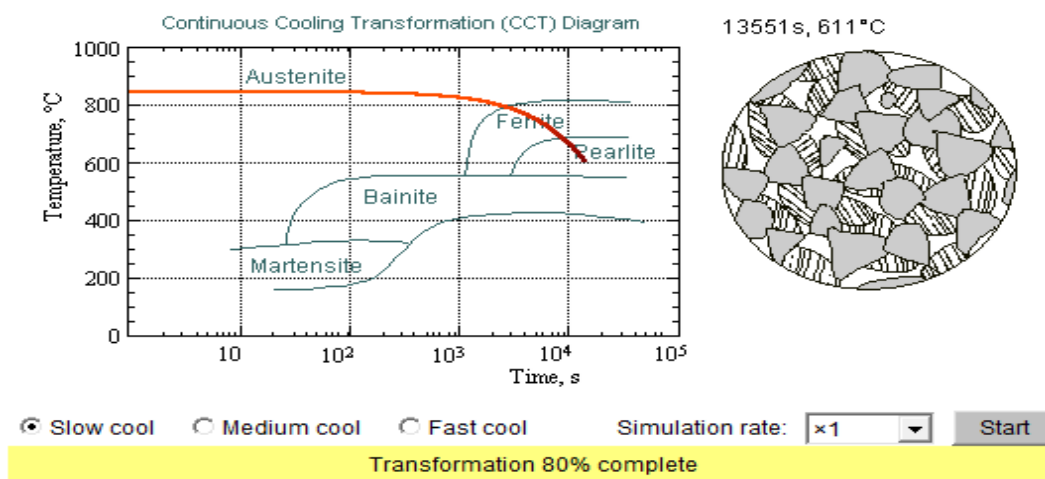


Figure 8. CCT diagram of the phase transformation of 0.4 wt.% C, 1.5 wt.% Mn, and 0.5 wt.% Mo steel from austenite to ferrite/pearlite in the slow cooling processes (figure reproduced with permission) [39].

4.2 Chemical Composition of Chosen Steels

X65 [0.14 wt. % C; 0.05 wt. % C], C1018 [ferrite-pearlite], and thermally treated C1018 and X65 [austenized then quenched and tempered; spheroidized]) steels were selected for study. Their chemical compositions are shown in Table 1, Table 2, and Table 3. These steels were selected in order to observe and measure the difference between them with respect to thickness and morphology of the cementite layer developed during corrosion and the variation in inhibitor performance on pre-corroded specimens.

Table 1
Chemical Composition of X65 (0.14 wt. % C)

Al	As	C	Co	Cr	Cu	Mn	Mo	Nb	Ni	P
0.033	0.015	0.14	0.012	0.150	0.140	1.180	0.160	0.027	0.38	0.012
S	Sb	Si	Sn	Ti	V	Zn	Fe			
0.003	0.035	0.25	0.012	0.002	0.052	0.004	balance			

Table 2
Chemical Composition of X65 (0.05 wt. % C)

Al	As	C	Co	Cr	Cu	Mn	Mo	Nb	Ni	P
0.033	0.015	0.05	0.012	0.15	0.14	1.51	0.16	0.03	0.38	0.004
S	Sb	Si	Sn	Ti	V	Zn	Fe			
<0.001	0.035	0.25	0.012	0.01	0.04	0.004	balance			

Table 3
Chemical Composition of C1018

Al	As	C	Co	Cr	Cu	Mn	Mo	Nb	Ni	P
0.001	0.007	0.18	0.010	0.063	0.250	0.79	0.020	0.006	0.078	0.008
S	Sb	Si	Sn	Ti	V	Zn	Fe			
0.029	0.011	0.25	0.017	<0.001	0.001	0.004	balance			

4.3 Microstructure of Chosen Steels

The cross-sectioned side of each flat sample was used to do metallographic analysis. These flat samples were mounted in the epoxy in order to do metallographic analysis using the polishing and etching process [39].

4.3.1 Etching Procedure:

2% Nital solution, prepared in-house, was used to conduct the etching.

Equipment and Material:

- a. 2% Nital solution which is 2% nitric acid in ethanol.
- b. Cotton used to swab samples.
- c. Polished samples ready to be etched.

Procedure

Two drops of 2% Nital solution were dropped on the cotton. The cotton was swabbed with the polished samples in a circular motion for 15 seconds until a haze (gray color) started to appear on the surface of the polished samples. Immediately, isopropyl alcohol and then deionized water (DI water) were used to rinse the samples. Finally, cold air was used to dry the samples.

An Alicona infinite focus microscope (IFM) and JEOL JSM6390LV scanning electron microscope (SEM) was used to conduct metallurgical studies for the samples.



Figure 9. Samples preparation for metallographic analysis: (a) Flat sample; (b) Mounted in epoxy.

The microstructures of these chosen steels are described as below:

X65: Two X65 steels were characterized, one has a carbon content of 0.14 wt.% C and the other 0.05 wt.% C. Figure 10 and Figure 11 show that their structures are similar to the martensitic structure shown in Figure 6. This is consistent with a processing that involves the steel being quenched and tempered (Q&T). The molybdenum in the alloy, 0.16 wt.% Mo, shifts the curves of the CCT diagrams to the right and assists martensite formation, as shown in Figure 5 and Figure 6 [39]. The carbon trapped in the martensite is released during a tempering technique to increase ductility and relieve internal stresses. Increasing the temperature of martensite to below the A_1 transformation temperature leads to a release of carbon from interstitial positions, resulting in (partial) transformation into ferrite and Fe_3C .

As shown before, low carbon content, 0.14 wt. % C and 0.05 wt.% C, shifts the curves of the CCT diagrams to the left side, which possibly stops the formation of martensite at rapid cooling rates. However, the curves of the CCT diagrams of the steels

with some addition of Mo can be shifted to the right and assist the formation of martensite [39]. Also, the percentages of the α -Fe and iron carbide in this steel are calculated based on the phase diagram as shown in Equation 17 and Equation 18.

$$\% \alpha = \frac{C_{Fe_3C} - C_0}{C_{Fe_3C} - C_\alpha} \quad (17)$$

Where:

C_0 is the amount of carbon content in the steel.

C_α is the amount of iron dissolved in ferrite which is 0.022.

For X65 (0.14 wt. % C):

$$\% \alpha = \frac{6.7 - 0.14}{6.7 - 0.022} = 98.2\%$$

For X65 (0.05 wt. % C):

$$\% \alpha = \frac{6.7 - 0.05}{6.7 - 0.022} = 99.6\%$$

$$\% Fe_3C = \frac{C_0 - C_\alpha}{C_{Fe_3C} - C_\alpha} \quad (18)$$

For X65 (0.14 wt. % C):

$$\% Fe_3C = \frac{0.14 - 0.022}{6.7 - 0.022} = 1.8 \%$$

For X65 (0.05 wt. % C):

$$\% Fe_3C = \frac{0.05 - 0.022}{6.7 - 0.022} = 0.4 \%$$

For quenched and tempered carbon steel, this assumes a full, rather than partial, transformation of martensite to α -ferrite with maximum formation of Fe_3C .

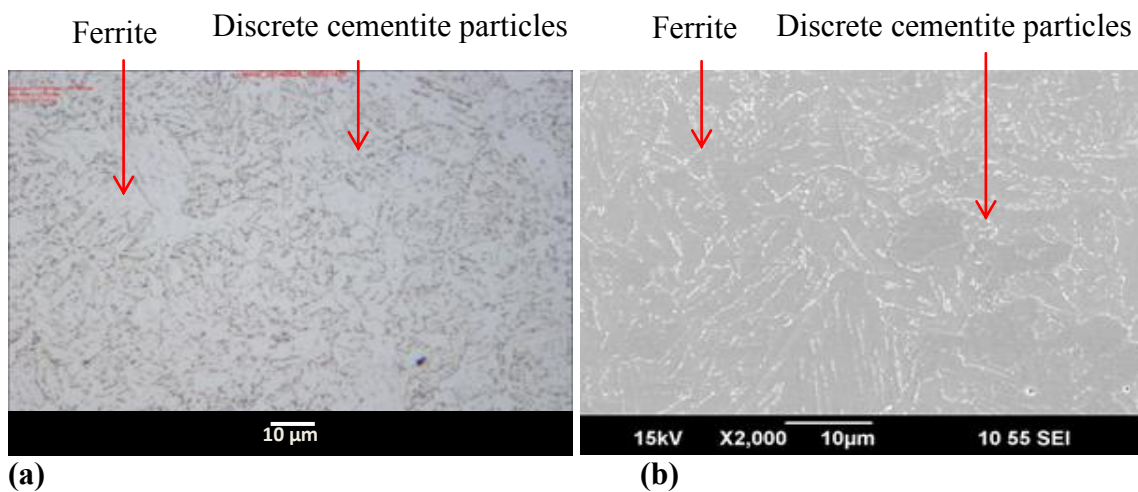


Figure 10. Microstructure of X65 (0.14 wt. % C) consists of tempered martensite: (a) IFM image; (b) SEM image.

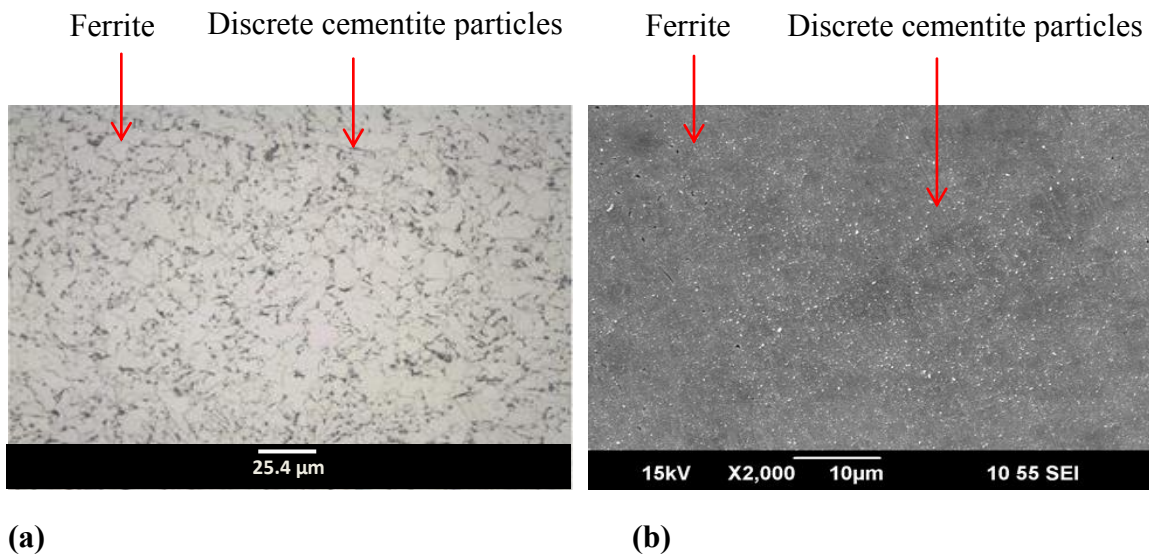
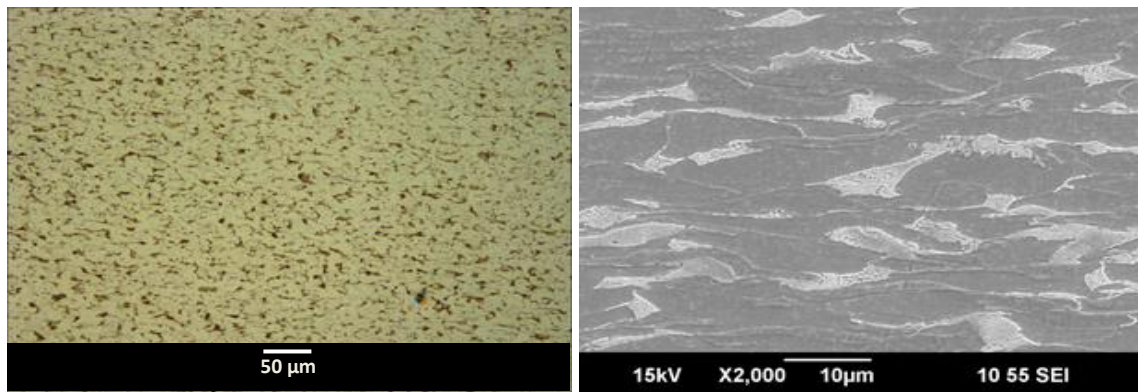


Figure 11. Microstructure of X65 (0.05 wt. % C) consists of tempered martensite: (a) IFM image; (b) SEM image.

C1018: This steel has a higher amount of carbon (0.18 wt. % C) than the X65 materials. Figure 12 shows that C1018 steel consists of light grains of ferrite with some dark pearlite grains. Also, this figure shows that the structure of this steel is similar to the ferrite/pearlite structure presented in Figure 13. C1018 was normalized by increasing the temperature of this steel to 50°C above A3, and then cooling it in air; the generated microstructure is composed of ferrite-pearlite.



(a)

(b)

Figure 12. Ferrite-pearlite microstructure of C1018: (a) IFM image (b) SEM image.

In addition, the concentration of ferrite, iron carbide, pearlite and proeutectoid ferrite in this steel is calculated, based on the phase diagram, as follows:

$$\% \alpha = \frac{C_{Fe_3C} - C_0}{C_{Fe_3C} - C_\alpha}$$

$$\% \alpha = \frac{6.7 - 0.18}{6.7 - 0.022} = 97.6\%$$

$$\% Fe_3C = \frac{C_0 - C_\alpha}{C_{Fe_3C} - C_\alpha}$$

$$\%Fe_3C = \frac{0.18 - 0.022}{6.7 - 0.022} = 2.4 \%$$

$$\% \text{ pearlite} = \frac{0.18 - 0.022}{0.76 - 0.022} = 21.4\%$$

$$\% \text{ proeutectoid ferrite} = 78.6\%$$

Table 4 shows the measured Rockwell B hardness values of the studied steels and calculated Vickers hardness values; measurements were taken with using 1/16 in Brale indenter 100 kg load these are given on the same hardness scale for ease of comparison.

Table 4
Hardness Values of The Different Microstructures

Material and Microstructure	Rockwell B Hardness (HRB)	Vickers Hardness (HV)
C1018 Quenched; martensitic	94.0 ± 0.31	213.0
C1018 Quenched and tempered martensite	90.1 ± 1.90	192.0
C1018 Normalized (initial); ferritic-pearlitic	82.0 ± 1.82	163.0
C1018 Spheroidized	69.6 ± 1.23	126.0
X65 (0.14 wt. % C) fine structure of pearlite in a ferrite matrix*	88.8 ± 0.19	179.0
X65 (0.05 wt. % C) fine structure of pearlite in a ferrite matrix*	87.1 ± 0.27	171.0
X65 (0.05 wt. % C) Spheroidized	70.6 ± 1.3	128.0

* As described in the analytical report by Nadcap see appendix A

Different thermal treatments of initial steels were applied in order to obtain two distinct types of steel microstructures, which are:

1. Spheroidized steel [on C1018 and X65 (0.05 wt. % C)]:

- a. Put the sample in the furnace at 700°C for 24 hours [21].
- b. After heating at 700°C for 24 hours, the furnace is turned off and the sample is naturally cooled therein for a further 24 hours.

Figure 13 shows the microstructure of this steel and also shows that these small particles, in the ferrite matrix and at the grain boundaries, are cementite. Also, the hardness value of the spheroidized steel is shown in Table 4.

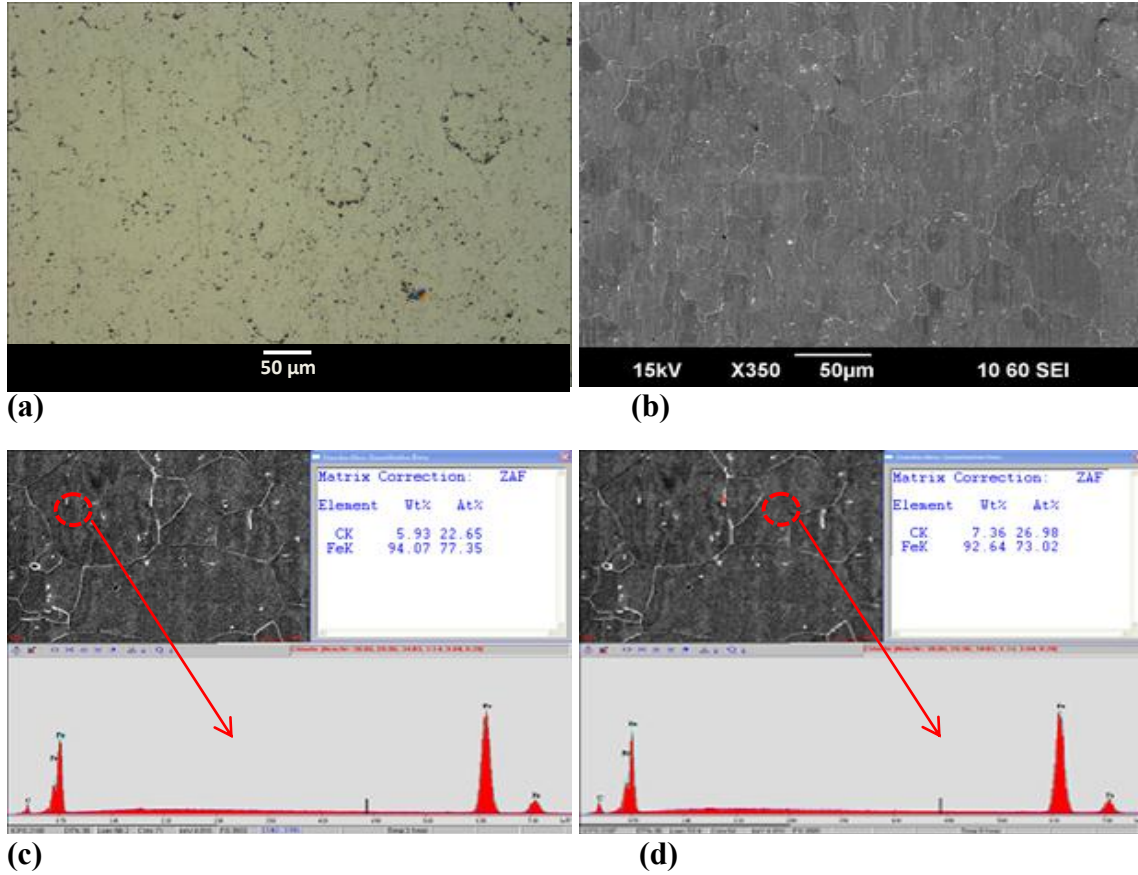


Figure 13. Spheroidized microstructure of C1018: (a) IFM image; (b) SEM image; (c) EDS images of spheroidized steel in ferrite matrix; (d) EDS images of spheroidized steel at grain boundaries.

Also, the content of ferrite and iron carbide in this steel is calculated, based on the phase diagram, as:

$$\% \alpha = \frac{C_{Fe_3C} - C_0}{C_{Fe_3C} - C_\alpha}$$

$$\% \alpha = \frac{6.7 - 0.18}{6.7 - 0.022} = 97.6\%$$

$$\% Fe_3C = \frac{C_0 - C_\alpha}{C_{Fe_3C} - C_\alpha}$$

$$\%Fe_3C = \frac{0.18 - 0.022}{6.7 - 0.022} = 2.4 \%$$

Figure 14 shows the microstructure of this steel and also shows that these small particles, in the ferrite matrix and in the grain boundaries, are cementite particles. Also, the hardness test of this steel is shown in Table 4.

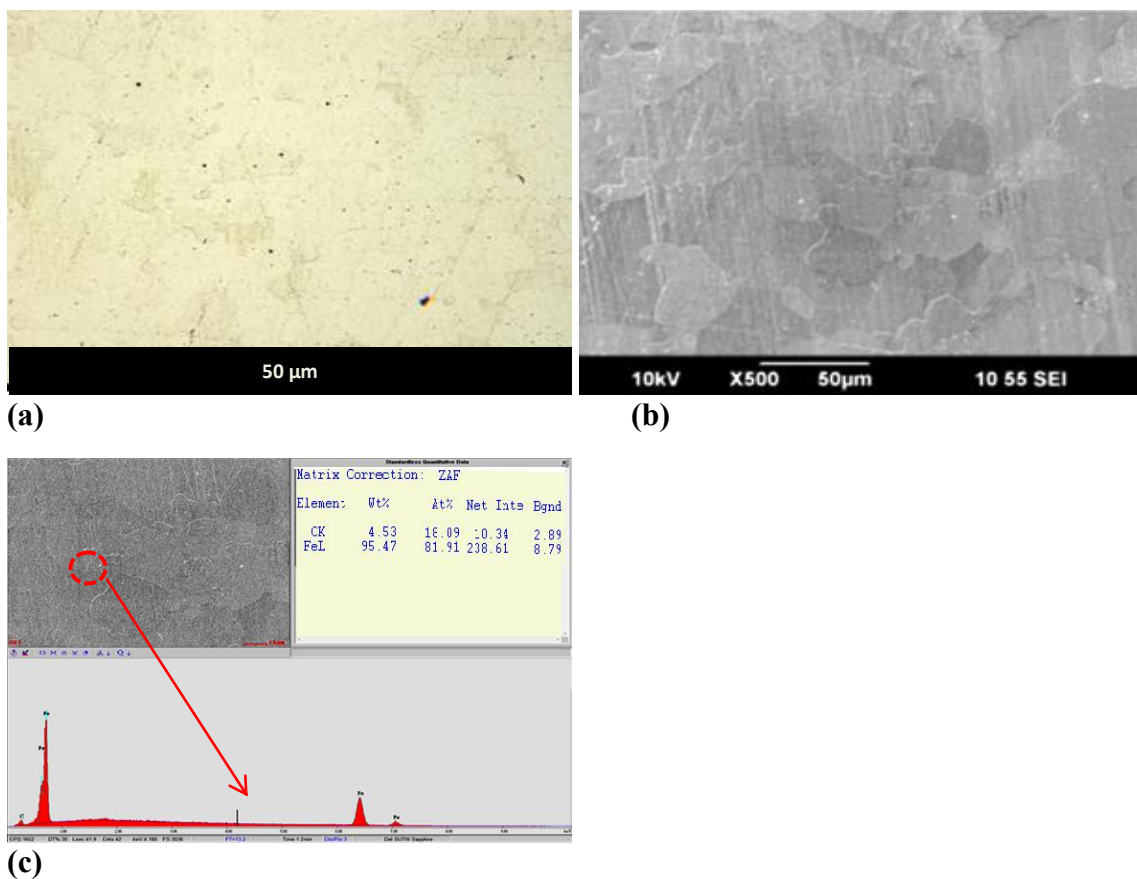


Figure 14. Spheroidized microstructure of X65 (0.05 wt. %C): (a) IFM image (b) SEM image (c) EDS images of spheroidized steel with ferrite matrix.

The concentration of ferrite and iron carbide in the spheroidized X65 steel with 0.05 wt.% C was similarly calculated as:

$$\% \alpha = \frac{C_{Fe_3C} - C_0}{C_{Fe_3C} - C_\alpha}$$

$$\% \alpha = \frac{6.7 - 0.05}{6.7 - 0.022} = 99.6\%$$

$$\% Fe_3C = \frac{C_0 - C_\alpha}{C_{Fe_3C} - C_\alpha}$$

$$\% Fe_3C = \frac{0.05 - 0.022}{6.7 - 0.022} = 0.4 \%$$

2. Quenched-Tempered steel

- a. Put the sample in the furnace at 900°C for 20 minutes
- b. After heating, the sample is quenched in the water for 5 minutes
- c. The quenched sample is reheated at 450°C for 30 minutes
- d. After reheating, the sample is cooled in water for 5 minutes

Figure 15 shows the microstructure of the C1018 after this thermal processing.

The hardness value of quenched as well as quenched and tempered specimens is shown in Table 4. In addition, Table 5 shows a summary of selected steel microstructures with heat treatment.

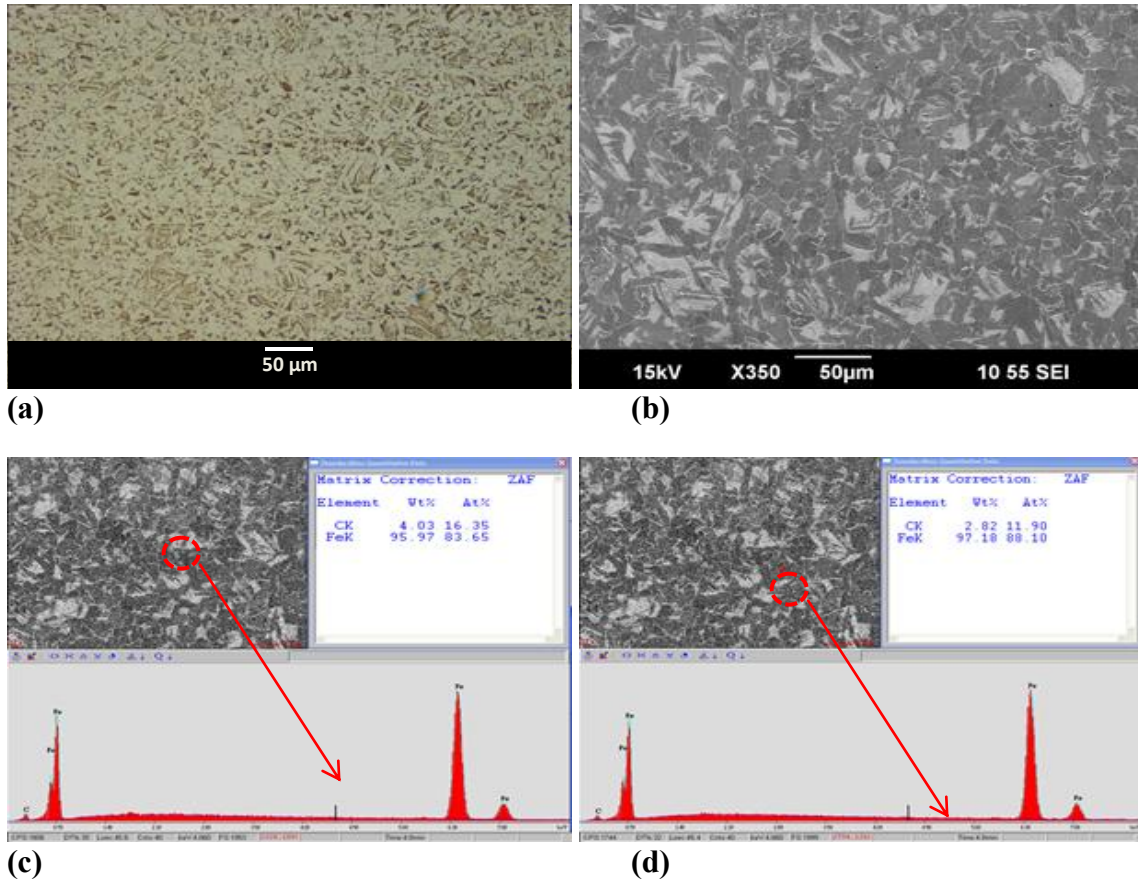


Figure 15. Quenched-tempered microstructure of C1018: (a) IFM image (b) SEM image (c) EDS images of quenched-tempered steel at a bright grain (d) EDS images of quenched-tempered steel at black a grain.

Moreover, the maximum ferrite and iron carbide contents in this steel are calculated as:

$$\% \alpha = \frac{C_{Fe_3C} - C_O}{C_{Fe_3C} - C_\alpha}$$

$$\% \alpha = \frac{6.7 - 0.18}{6.7 - 0.022} = 97.6\%$$

$$\%Fe_3C = \frac{C_0 - C_\alpha}{C_{Fe_3C} - C_\alpha}$$

$$\%Fe_3C = \frac{0.18 - 0.022}{6.7 - 0.022} = 2.4 \%$$

Table 5
Microstructure and Heat Treatment of The Selected Steels

Steel	Carbon content wt%	Microstructure	Heat treatment
X65	0.14	Tempered Martensite	Quenched & Tempered (Q-T)
X65	0.05	Tempered Martensite	Quenched & Tempered (Q-T)
X65	0.05	Spheroidized	Spheroidized (Sph.)
C1018	0.18	Ferrite/pearlite	Normalized
C1018	0.18	Spheroidized	Spheroidized (Sph.)
C1018	0.18	Quenched-tempered	Quenched-tempered (Q-T)

CHAPTER 5: GENERAL CORROSION EXPERIMENTS

5.1 Introduction

Glass cell experiments were conducted with 2 liters of 1 wt.% NaCl as the electrolyte at the desired temperature. A magnetic stirrer, set to 200 rpm, was used to ensure a fully mixed solution as carbon dioxide gas was constantly sparged into the solution. The solution pH was adjusted to the desired value by addition of deoxygenated 1.0 M sodium hydroxide (NaOH) or sodium bicarbonate (NaHCO₃) solutions. Hydrochloric acid (HCl) was used to maintain the pH around 5.0. Samples were immersed in the glass cell once the pH stabilized. Tests were run for 3 days with 3 samples. The studied steels were X65 with 0.14 wt.% C (ferrite-discrete cementite), a lower carbon X65 with 0.05 wt.% C (ferrite-discrete cementite), thermally treated X65 (0.05 wt.% C, spheroidized), C1018 (ferrite-pearlite), thermally treated C1018 (austenized then quenched and tempered), and thermally treated C1018 (spheroidized). Each steel was used in separate sets of experiments. . After 24 hours of each experiment, a sample was withdrawn for surface analysis. Electrochemical techniques were employed in order to measure the corrosion properties of carbon steel with time; open circuit potential (OCP), linear polarization resistance (LPR), and electrochemical impedance spectroscopy (EIS) were used. A Gamry® Reference 600 potentiostat was used for all electrochemical measurements. Weight loss (WL) measurements were also used to determine corrosion rates. Scanning electron microscopy (SEM), energy dispersive X-ray spectroscopy (EDS), and backscattered electron imaging (BSE) were used for surface analysis.

5.2 Experimental Set-up and Instrumentation

In order to achieve the goals of this study, preliminary experiments have been designed and conducted in low pressure CO₂ conditions with a glass cell at 1 bar total pressure. A three-electrode set up was used, as shown in Figure 16, with the following electrode arrangement:

- Working electrode (WE): cylindrical carbon steel test samples (5.4 cm² for X65 and 5.5 cm² for C1018).
 - Counter electrode (CE): platinum mesh (6 cm²). The role of this electrode is to apply a polarization current that is generally controlled according to current density or to the steel potential.
 - Reference electrode (RE): a saturated silver/silver chloride (Ag/AgCl) probe separated from the system by a porous Vycor® frit. The role of this electrode is to observe the response of the electrochemical system to the perturbation caused by counter electrode.
- The temperature and pH were continuously observed.

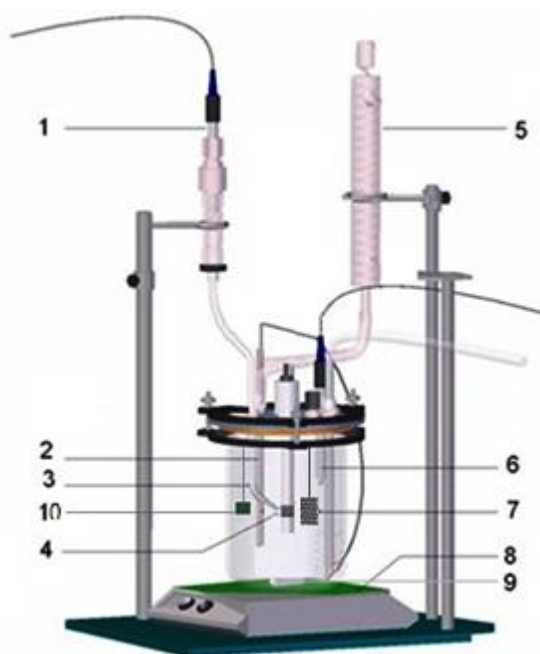


Figure 16. Experimental cell design- 1- Ag/AgCl reference electrode, 2- Thermocouple probe, 3- Luggin capillary, 4- Cylindrical working electrode, 5-Condenser, 6- pH probe, 7- Counter electrode, 8- Hot plate, 9- Stir bar, 10- Hanging samples (adapted from a drawing provided by Cody Shafer in ICMT).

5.2.1 Materials and Sample Preparation

X65 and C1018 carbon steels were selected for study. Their chemical compositions and microstructures are shown in Table 1, Table 2, Table 3, Figure 10, Figure 11, Figure 12, Figure 13, Figure 14, and Figure 15, respectively. Samples were wet polished with 150, 400 and 600 grit silicon carbide (SiC) paper, washed with isopropyl alcohol in an ultrasonic bath and dried. Flat samples and cylindrical samples were placed into the test electrolyte. The flat samples were for surface analyses and the

cylindrical samples were mounted on a holder and acted as the working electrode for the electrochemical measurements.

5.2.2 Procedure

Test conditions and a test matrix, respectively, are shown in Table 6 and Table 7. The glass cell was filled with 2 liters of electrolyte with a concentration of 1 wt. % NaCl. A magnetic stirrer (at 200 rpm) was used to stir the solution and the temperature was set to the desired value. Carbon dioxide gas was constantly sparged into the solution. The dissolved oxygen levels in the solution were below 10 ppb. The pH was adjusted to the desired value by addition of deoxygenated sodium hydroxide (NaOH) or sodium bicarbonate (NaHCO_3) solution. Hydrochloric acid (HCl) was used to maintain the pH at 5.0 ± 0.1 . Samples were immersed in the glass cell once the pH stabilized. After each 24 hour interval, samples were withdrawn for surface analysis.

Experimental procedures are shown in Figure 17. Electrochemical techniques were employed in order to measure the corrosion properties of carbon steel with time; namely open circuit potential (OCP), linear polarization resistance (LPR), and electrochemical impedance spectroscopy (EIS). Polarization resistance (R_p) was obtained from LPR and was fixed by subtracting solution resistance (R_s) determined from EIS measurements; see Table 8 for key parameters relating to electrochemical measurements. Weight loss (WL) measurements were also used to determine corrosion rates. Infinite focus microscopy (IFM), scanning electron microscopy (SEM), energy dispersive X-ray spectroscopy (EDS), and backscattered electron imaging (BSE) were used for surface analysis.

Table 6
Test Conditions

Test condition #	Initial pH and Temperature	Test Time	Test Material
Step 1: Develop Experimental Procedure			
1	pH=6.0, T=80 °C	23 hours	X65
2	pH=6.0, T=60 °C	24 hours	X65
3	pH=6.0, T=40 °C	24 hours	X65
4	pH=5.0, T=60 °C	24 hours	X65
Step 2: Investigate Fe ₃ C Characteristics Related to the Microstructure of the Material			
5	pH=5.0, T=60 °C	3days	C1018(F/P)
6	pH=5.0, T=60 °C	3days	C1018(Sph.)
7	pH=5.0, T=60 °C	3days	C1018(Q-T)
8	pH=5.0, T=60 °C	3days	X65 (0.14 wt.% C)
9	pH=5.0, T=60 °C	3days	X65 (0.05 wt.% C)
Step 3: Investigate the Effect of Residual Fe ₃ C on Inhibitor Performance			
10	pH=5.0, T=60 °C, Inhibitor	3days	C1018(F/P)
11	pH=5.0, T=60 °C, Inhibitor	3days	C1018(Sph.)
12	pH=5.0, T=60 °C, Inhibitor	3days	C1018(Q-T)
13	pH=5.0, T=60 °C, Inhibitor	3days	X65 (0.14 wt.% C)
14	pH=5.0, T=60 °C, Inhibitor	3days	X65 (0.05 wt.% C)

Table 7
Test Environment

Parameter	Conditions & Methods
Test solution	1 wt.% NaCl
Total Pressure	1 bar
Reagents to adjust Ph	NaHCO ₃ , NaOH & HCl (as aqueous solutions)
Stirring	200 RPM

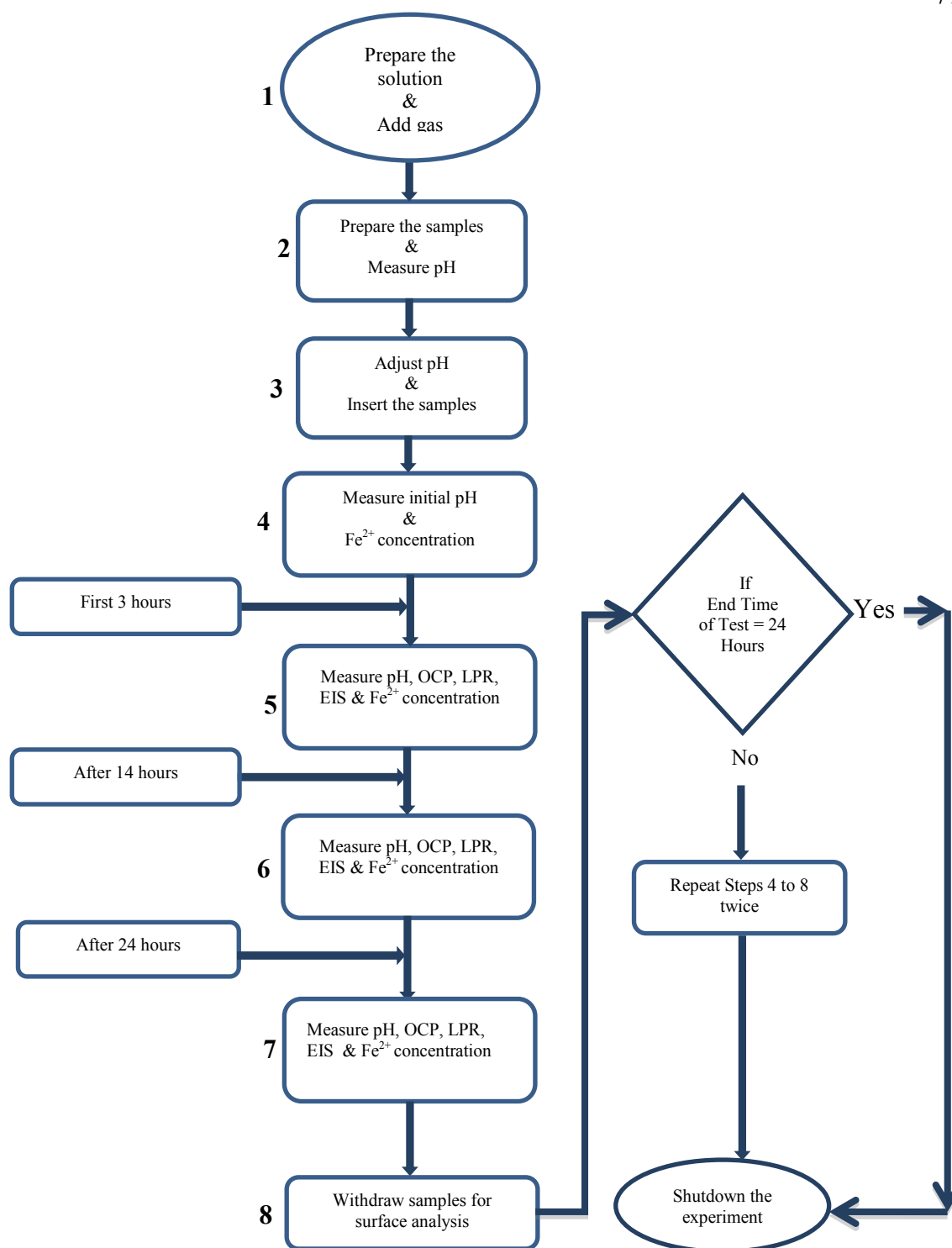


Figure 17. Diagrammatic representation of measurement plan.

Table 8
Experimental Parameters for Electrochemical Measurements

Technique	Parameters
LPR	Scan Rate: 0.125 mV / s. Polarization range: ± 5 mV (vs. Open Circuit Potential). B value: 26 mV
EIS	Frequency range: 10000 Hz \sim 0.001 Hz. Points per Decade: 5. AC amplitude: 5 mV. DC potential: 0 vs. EOC.

A Gamry potentiostat was used to conduct the electrochemical measurements. In the beginning, the OCP was measured and then appropriate time permitted the stabilization of the potential of the sample. A large fluctuation in the values of OCP (greater than 10% of the applied potential for the measurement of LPR) would result in incorrect values of the polarization resistance (R_p). Therefore, this stabilization is important to ensure a correct reading of the LPR measurement. Polarization ranging from -5 mV to +5 mV with respect to the OCP at a scan rate of 0.125 mV/s was used in order to polarize the potential of the sample. The LPR measurements were taken multiple times in each experiment. Preceding each measurement of the LPR, the OCP was measured for 5 minutes in order to be sure the potential of the specimen reverted to its original reading and was steady. Equation 19 was used in order to calculate the corrosion current of each measurement:

$$I_{corr} = \frac{B}{R_p} \quad (19)$$

Where:

I_{corr} represents the corrosion current (Amps)

B represents the Stern-Geary coefficient, called B value (V)

R_p represents the polarization resistance (Ω)

Depending on the metal and electrolyte, B value may vary from 0.013 to 0.052 V.

It was assumed that the corrosion rate was not purely under charge-transfer control.

According to this assumption, it is recommended to use $B=0.026$ V [38]. Equation 20

was used in order to calculate B value, $B = 0.026$ V, by using values of 0.12 V/decade for both the anodic and cathodic Tafel coefficients:

$$B = \frac{\beta_a * \beta_c}{2.3 * (\beta_a + \beta_c)} \quad (20)$$

Where:

β_a represent anodic Tafel coefficients (V/decade)

β_c represent cathodic Tafel coefficients (V/decade)

Equation 21 was used in order to calculate the corrosion rate of each LPR measurement:

$$CR = \frac{I_{corr} * M}{\rho * n * F * A} \quad (21)$$

Where:

I_{corr} represents the corrosion current (Amps) already calculated from Equation 19

M represents the molecular weight (g)

ρ represents the density of the sample (g/cm^3)

n represents number of electrons involved in the electrochemical reaction

F represents Faraday constant, 96,487 coulombs

A represents the surface area of the sample (cm^2)

Furthermore, in order to measure the corrosion rate by weight loss measurement for tested steels, Equation 22 was used:

$$\text{Corrosion rate} \left(\frac{\text{mm}}{\text{yr}} \right) = \frac{*W}{A * t * d} \quad (22)$$

Where:

W represents the mass loss (g).

A represents the surface area of the sample (mm^2).

t represents the exposure time (year).

d represents the density of the sample material (g/mm^3).

5.3 Results and Discussion

5.3.1 Development of Experimental Procedures:

The goal of this step is to achieve repeatable test conditions for development of iron carbide layers by using two series of experimental conditions:

- pH 6.0 for 40°C, 60°C and 80°C.
- 60°C for pH values of 5.0 and 6.0.

Effect of Fe_3C on Corrosion:

Figure 18, for pH 6.0, shows that the corrosion rate (CR) was relatively constant with time at a lower temperature and increased with time at a higher temperature. Acceleration of electrochemical and chemical reactions is the reason that the corrosion rate increased with increased temperature [13].

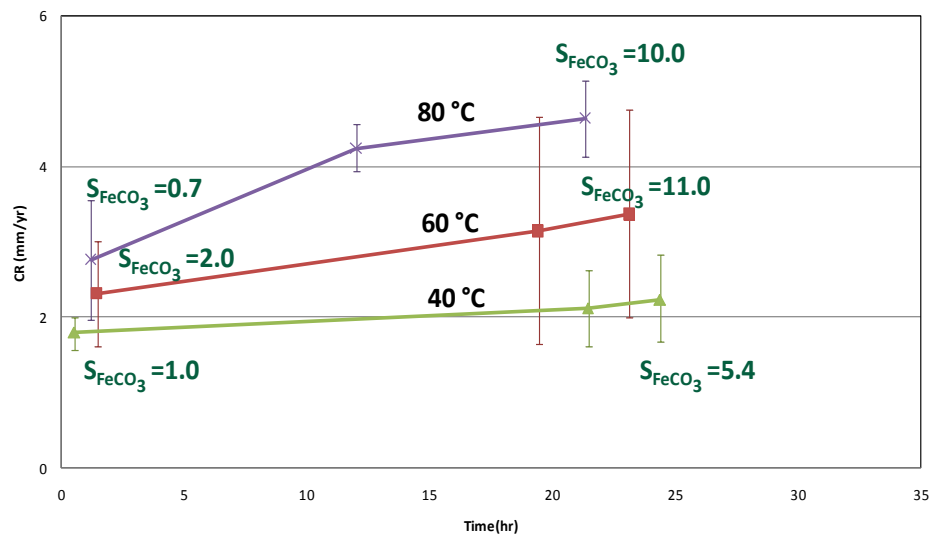


Figure 18. Corrosion rate vs. time for experiments conducted at pH=6 at 40°C, 60°C and 80°C with X65 steel.

Figure 19 shows that the corrosion rate (CR) increased with time more for the pH 5.0 condition than for the pH 6.0 condition at 60°C. This is consistent with a greater availability of hydrogen ions, hence an enhanced rate for the hydrogen ion reduction reaction [13]. Furthermore, it is well known that exposed, porous and non-protective iron

carbide acts as a cathodic surface while the ferrite is anodic [13]. Therefore, during the corrosion process, the CO_2 saturated electrolyte can penetrate through these iron carbide layers and further corrosion of the underlying ferrite takes place. Such oxidative dissolution of steel will lead to residual, and progressively thicker, iron carbide layers. Thus, a thicker iron carbide layer means an increase in the area of the cathodic site associated with the corrosion process, and its acceleration. The pH 5 solution has a higher initial corrosion rate because of the greater availability of hydrogen ions. The slope of the LPR corrosion rate for the pH 5 solution is greater because of the progressively thicker, higher surface area iron carbide layer on which the cathodic reduction reactions take place.

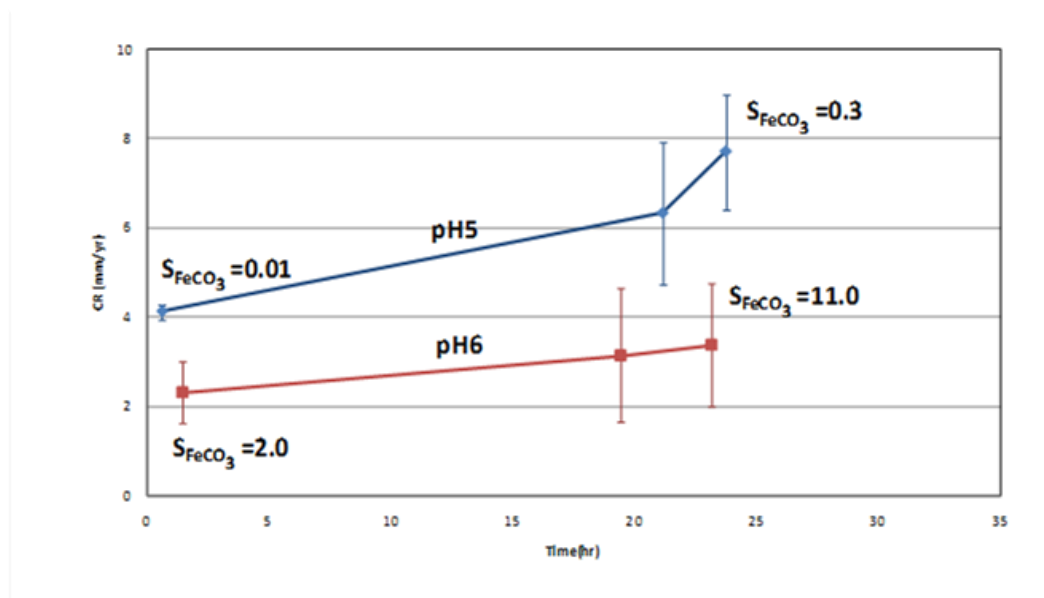


Figure 19. Corrosion rate vs. time for experiments conducted at pH 5.0 and pH 6.0 at 60°C with X65 steel.

Differences in degree of saturation, with respect to FeCO_3 , with time are also shown in Figure 18 and Figure 19.

The saturation level, $S(\text{FeCO}_3)$, is termed undersaturated when less than one and supersaturated when this level is greater than one.

Figure 18 shows that supersaturation of iron carbonate is rapidly achieved at pH 6.0 at each of the studied temperatures. Similar degrees of supersaturation were observed at 60°C and 80°C, but were lower at 40°C. This indicates that there is a higher probability for formation of a protective iron carbonate layer at pH 6.0 at each of the studied temperatures [13]. Under these conditions, it is predicted that iron carbonate will form on the surface and consequently lower the corrosion rate by acting as a mass transfer barrier between the solution and the steel surface. However, in order to initiate the formation of iron carbonate, high saturation values are needed [41]. Figure 19 shows that for the pH 5.0 test at 60°C, the saturation limit relating to the bulk condition was not exceeded. This means that there is a low probability for formation of an iron carbonate corrosion product layer that can confer protection [13]. Figure 19 also shows that the saturation limit for iron carbonate at pH 6.0 at 60°C was exceeded. As shown in Figure 19, the corrosion rate for pH 6.0 at 60°C did not appreciably increase as compared to the corrosion rate for pH 5.0 at 60°C. Therefore, in order to avoid precipitation of the iron carbonate layer, experimental conditions at pH 5.0 and 60°C are the best for this study.

Surface Analysis:

SEM and BSE images with EDS spectra of top surface areas and cross-sections, respectively, for the pH 6.0 tests at 40°C, 60°C and 80°C are shown in Figure 20, Figure

21, and Figure 22. The surface morphology shows uniform corrosion and no scattered crystals of iron carbonate on the surface. The thickness of the iron carbide is thinner at a lower temperature than at a higher temperature. Figure 20 (d), Figure 21 (d), and Figure 22 (d) show that the iron carbide is present on the surface. This results in higher corrosion rate with increasing temperature, as shown in Figure 18. Corrosion rates were calculated based on the depth of the iron carbide layer for the pH 6.0 tests at 40°C, 60°C, and 80°C and determined to be $1.8 \pm 0.9/-0.5$ mm/yr, $2.2 \pm 2.1/-1.4$ mm/yr, and $2.9 \pm 2.2/-1.4$ mm/yr, respectively. It is well known that temperature will affect the rates of the corrosion reactions which in turn will also affect the thickness of the residual iron carbide layer. Results of EDS and BSE analyses also confirm that the iron carbide remains on the steel surface.

SEM, BSE images, and EDS spectra of top surface areas and cross-sections, respectively, for the pH 5.0 test at 60°C are shown in Figure 23. Although the surface morphology again shows uniform corrosion and no scattered crystals of iron carbonate on the surface, the thickness of the iron carbide layer increased with time more for the pH 5.0 condition than for pH 6.0 at 60°C. As shown in Figure 19, corrosion rate (CR) increased with time more for the pH 5.0 condition than for the pH 6.0 condition at 60°C. Also, corrosion rates were calculated based on the depth of the iron carbide layer for the 60°C tests at pH 5.0 and pH 6.0 are 1.8 ± 0.4 mm/yr and $3.1 \pm 2.3/-1.6$ mm/yr, respectively. This indicates that the higher the corrosion rate, the thicker the iron carbide layer becomes as the ferrous ions leave the material and the iron carbide structure remains. Also, this indicates that the pH has an effect on the development of the iron

carbide layer. Results of EDS and BSE analyses also confirm that the iron carbide is left over on the steel surface. Note that the surface layer contains Mo, Mn, Ni, and V alloying elements at elevated concentrations relative to the steel substrate. In addition, when the ferritic-discrete cementite microstructure steel was corroded, some discrete cementite particles remained on the surface whilst others lost contact with the steel surface as shown in Figure 24. This resulted in formation of a layer of cementite on the steel surface. It is also noteworthy that the thickest iron carbide layer was observed for the pH 5.0 test at 60°C as shown in Table 9.

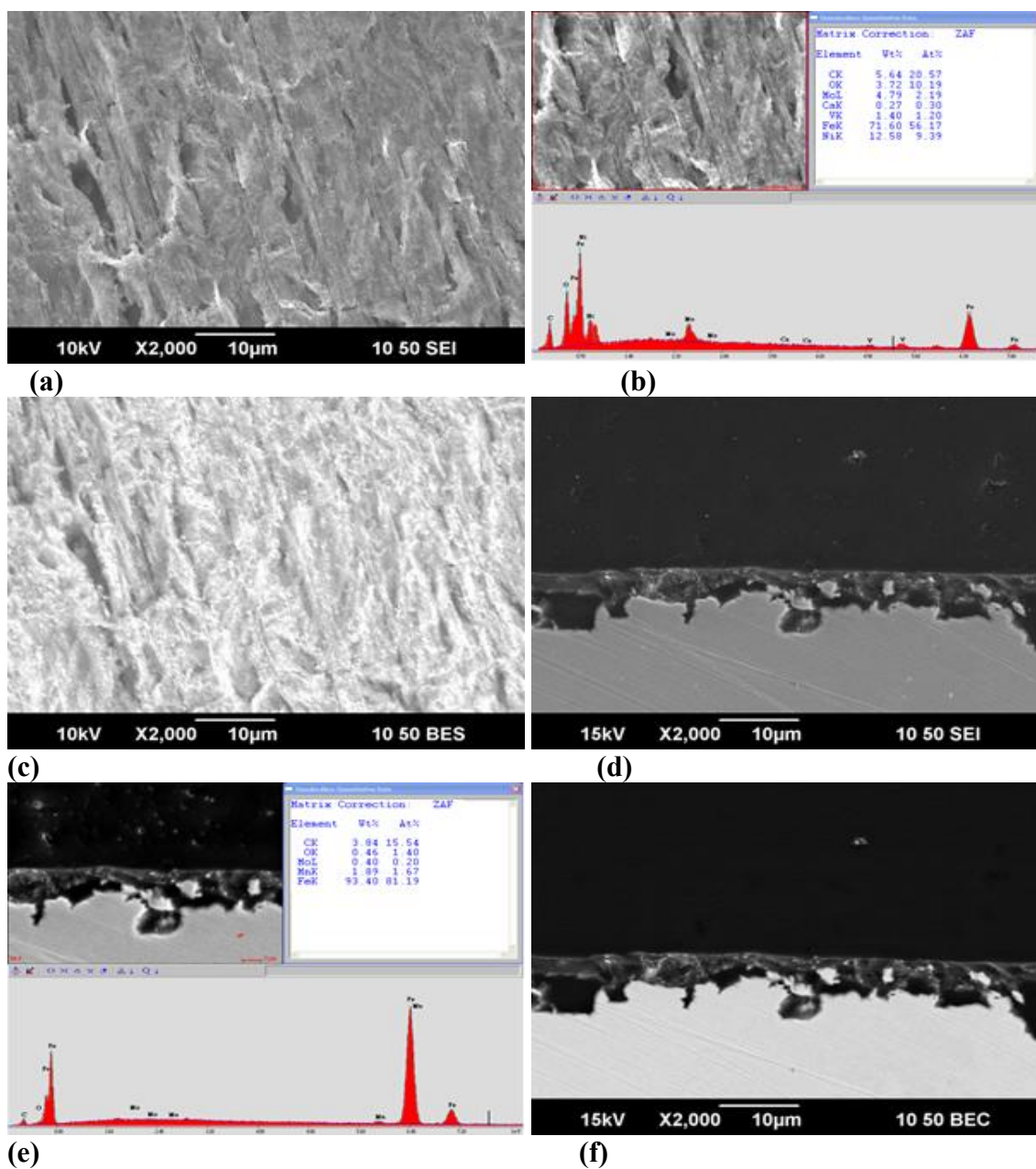


Figure 20. Sample (X65) for bulk solution pH 6.0 at 80°C after 1 day (a) SEM image for the surface (b) EDS spectrum for the surface (c) BES image for the surface, (d) SEM image for the cross section, (e) EDS spectrum for the cross section, and (f) BES image for the cross section.

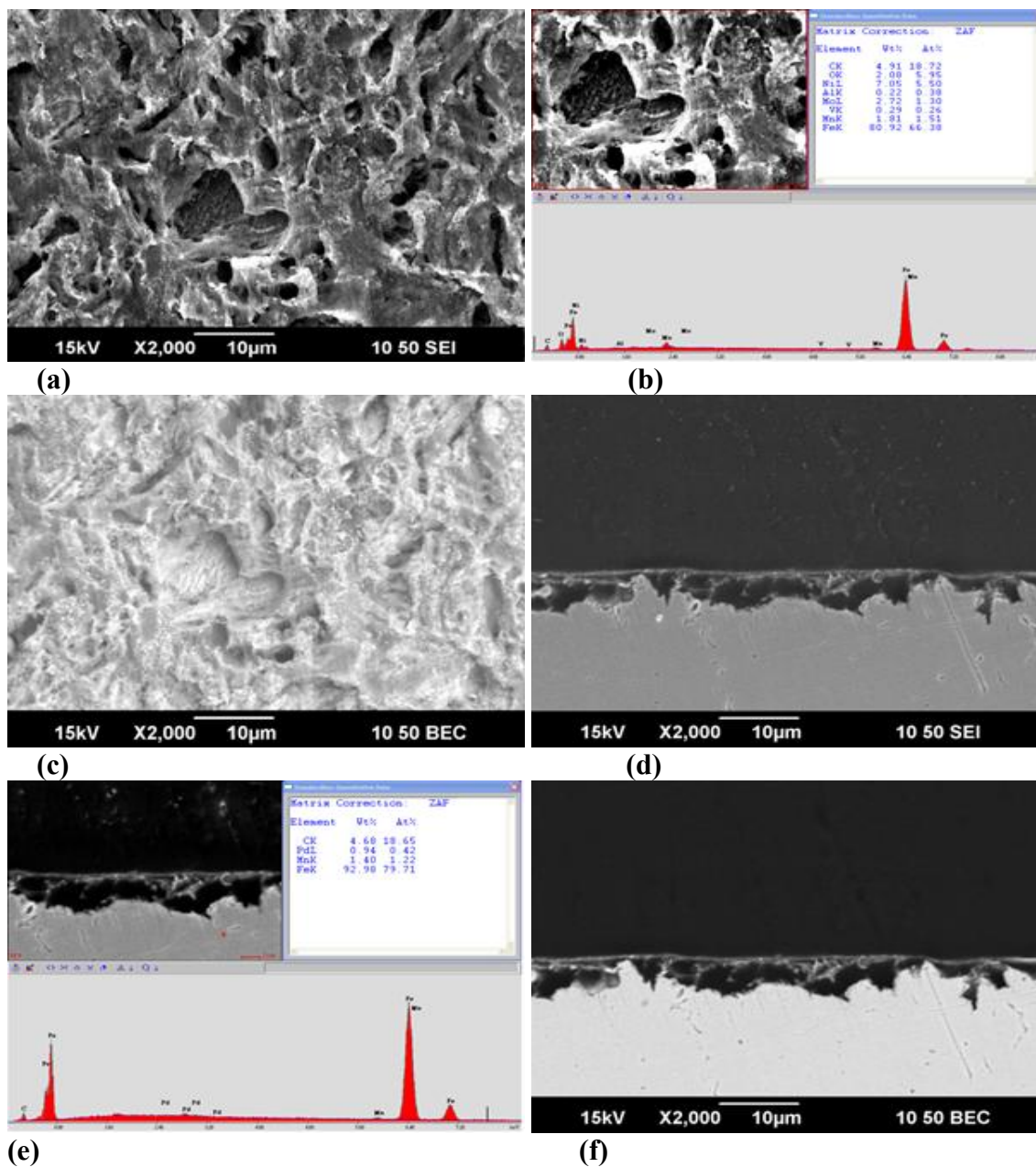


Figure 22. Sample (X65) for bulk solution pH 6 at 40°C after 1 day (a) SEM image for the surface, (b) EDS spectrum for the surface, (c) BES image for the surface, (d) SEM image for the cross section, (e) EDS spectrum for the cross section, and (f) BES image for the cross section.

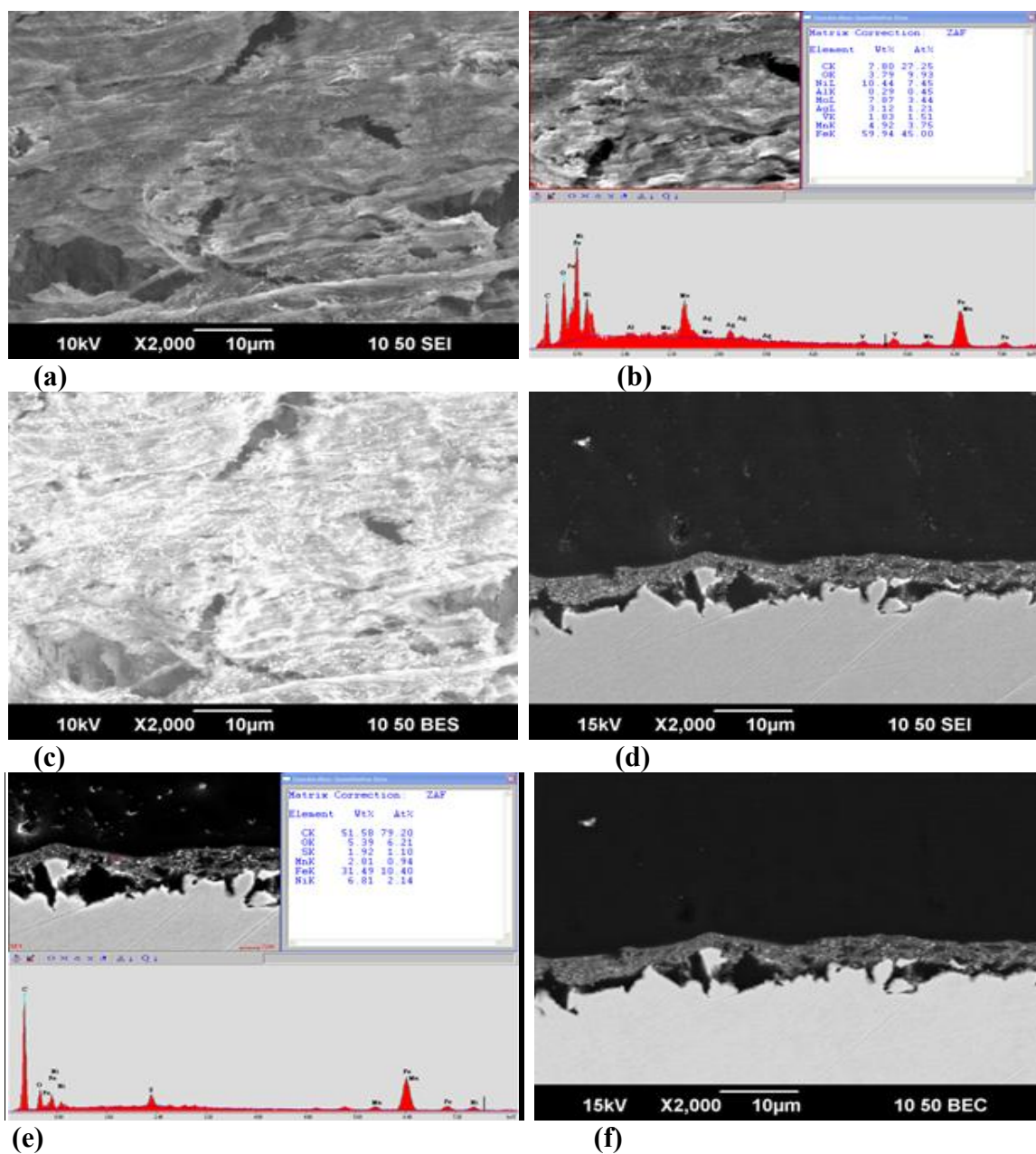
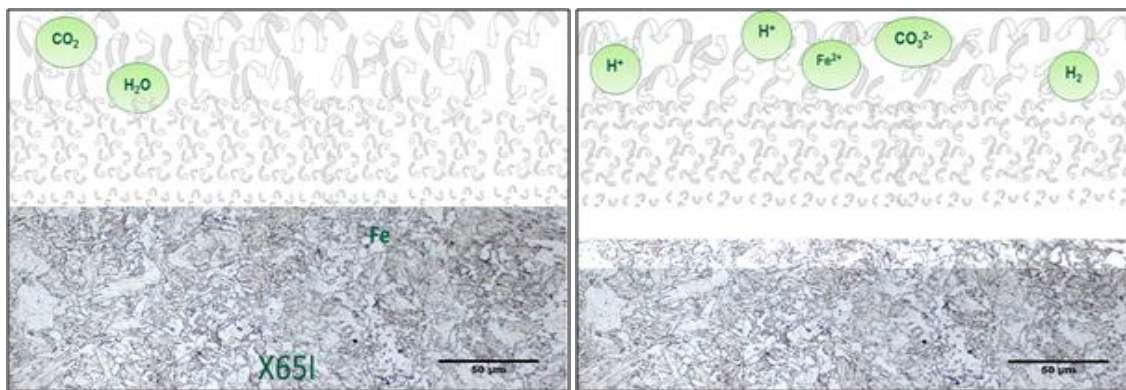


Figure 23. Sample (X65) for bulk solution pH 5 at 60°C after 1 day (a) SEM image for the surface, (b) EDS spectrum for the surface, (c) BES image for the surface, (d) SEM image for the cross section, (e) EDS spectrum for the cross section, and (f) BES image for the cross section.

Table 9
Thickness of Iron Carbide

Test condition #	Initial pH and Temperature	Test Time	Thickness of Fe ₃ C	Depth CR
X65 (0.14 wt. % C) Steel				
		(hours)	(μm)	(mm/yr)
1	pH=6.0, T=80 °C	23	7.8 +6.1/-3.9	1.8 +0.9/-0.5
2	pH=6.0, T=60 °C	24	6.1 +5.7/-3.1	2.2 +2.1/-1.4
3	pH=6.0, T=40 °C	24	5.1 +2.4/-1.5	2.9 +2.2/-1.4
4	pH=5.0, T=60 °C	24	8.5 +6.3/-1.6	3.1 +2.3/-1.6



(a)

(b)

Figure 24. Schematic drawing of different microstructures: (a) sample of ferretic-discrete cementite microstructure (b) sample of a corroded ferretic-discrete cementite microstructure.

5.3.1.1 Summary for Development of Experimental Procedures

The corrosion rate (CR) was relatively constant with time at a lower temperature and increased with time at a higher temperature. During each study, the iron carbides were left over on the surface of the corroded sample. Also, the thickness of the iron carbide is thicker at a higher temperature than at a lower temperature. The corrosion rate (CR) increased with time more for the pH 5.0 condition than for the pH 6.0 condition at 60°C. In addition, the thickness of the iron carbide layer increased with time more for the pH 5.0 condition than for pH 6.0 at 60°C.

During the corrosion process, the CO₂ saturated electrolyte can penetrate through these iron carbide layers and further corrosion of the underlying ferrite takes place. The pH 5 solution has a higher initial corrosion rate because of the greater availability of hydrogen ions. The slope of the LPR corrosion rate for the pH 5 solution is greater because of the gradual increase in thickness of the iron carbide layer. There is a higher probability for formation of a protective iron carbonate layer at pH 6.0 at each of the studied temperatures because the supersaturation of the iron carbonate is rapidly achieved at pH 6.0 at each of the studied temperatures. Therefore, in order to avoid precipitation of the iron carbonate layer, experimental conditions at pH 6.0 and different temperatures are not optimal for this study. However, for the pH 5.0 tests at 60°C, there is a low probability for the formation of an iron carbonate corrosion product layer that can confer protection because the saturation limit relating to the bulk condition was not exceeded. Therefore, in order to avoid precipitation of the iron carbonate layer, experimental conditions at pH 5.0 and 60°C are the best for this study. Moreover, some discrete

cementite particles remained on the surface whilst others lost contact with the steel surface when the ferritic-discrete cementite microstructure steel was corroded.

5.3.2 Investigation of Fe_3C Characteristics Related to The Microstructure of The Steel:

The goal of this step is to use different steels, X65 and C1018, in order to:

1. Observe the difference between X65 and C1018 steels with respect to thickness and morphology of the cementite layer developed during corrosion.
2. Measure weight loss in order to compare LPR corrosion rate and depth of the iron carbide with weight loss corrosion rate.

Effect of Fe_3C characteristics on corrosion:

- C1018 Ferrite-pearlite steel:

Figure 25 shows that the corrosion rate (CR) increased with time for the C1018 ferrite-pearlite material and that the saturation limit of FeCO_3 was not exceeded.

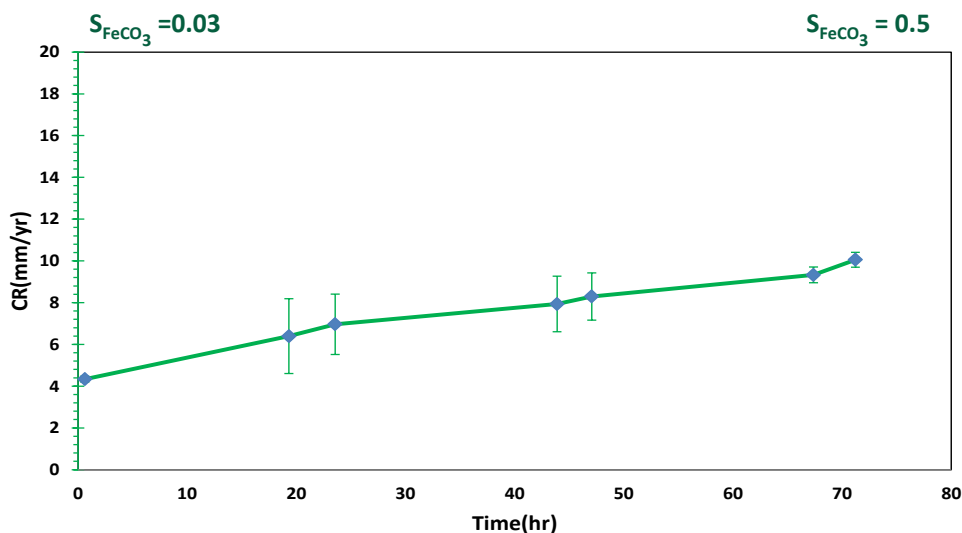


Figure 25. Corrosion rate vs. time for experiments conducted at pH 5.0 and 60°C with C1018 ferrite-pearlite steel.

LPR is measured multiple times per day and the area under the CR versus time curve is integrated for a value which should be equivalent to the weight loss corrosion rate. It is shown in Figure 26 that the integrated LPR corrosion rate does not match the weight loss corrosion rate. The reason the rates do not match is that the LPR measurements are affected by an increase in the surface area where the cathodic reaction occurs (hydrogen reduction). This increase in “cathodic area” is directly related to the amount of cementite left over by the corrosion process. The cathodic reaction happens on both initial active surface and on the newly developed cementite surface while the anodic reaction (oxidation of iron) only occurs on the initial active surface. A galvanic coupling between the initial anodic steel and the added cathodic cementite follows. The change in cathodic surface area with the development of iron carbide cannot be captured by the

LPR measurements which are performed assuming that the anodic and cathodic surface areas are identical and constant of time. It is believed that this observation is at the heart of the mismatch between LPR and weight loss measurements.

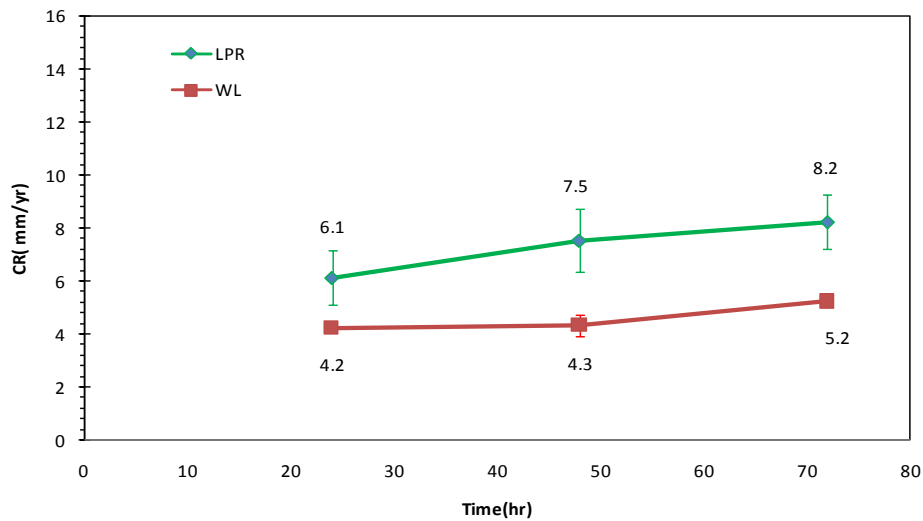


Figure 26. LPR and weight loss corrosion rate vs. time for experiments conducted at pH 5.0 and 60°C on C1018 ferrite-pearlite steel.

- C1018 spheroidized steel:

Figure 27 shows that the corrosion rate (CR) increased with time for the C1018 spheroidized material and that the saturation limit of FeCO_3 was not exceeded. Figure 25 and Figure 27 show that the corrosion rate increases in each case, but there is a higher corrosion rate for C1018 spheroidized material.

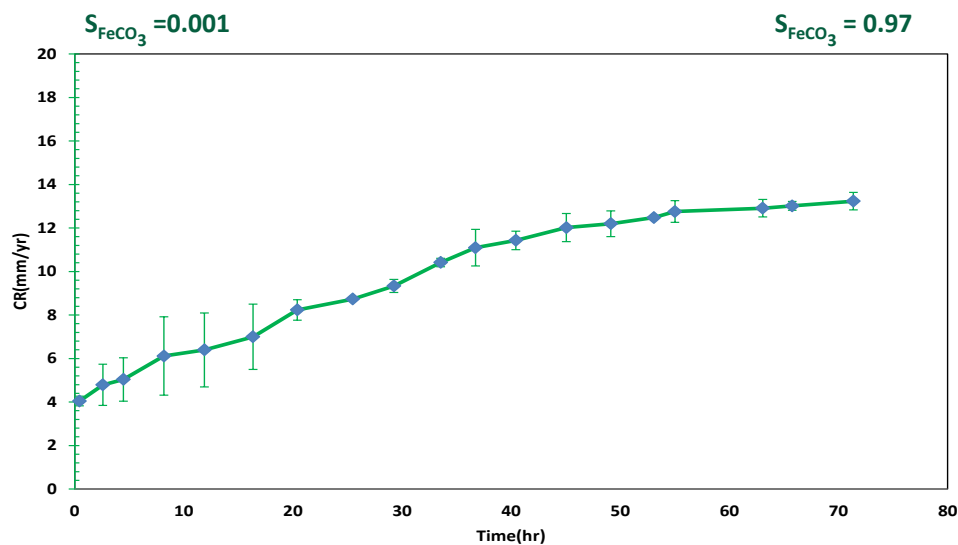


Figure 27. Corrosion rate vs. time for experiments conducted at pH 5.0 and 60°C with C1018 spheroidized steel.

LPR is also measured multiple times per day and the area under the CR versus time curve is integrated for a value which should be equivalent to the weight loss corrosion rate. It is shown in Figure 28 that the integrated LPR corrosion rate again does not match the weight loss corrosion rate. As previously, the reason the rates do not match is that the LPR value are affected by an increase in cathodic surface area, with development of iron carbide.

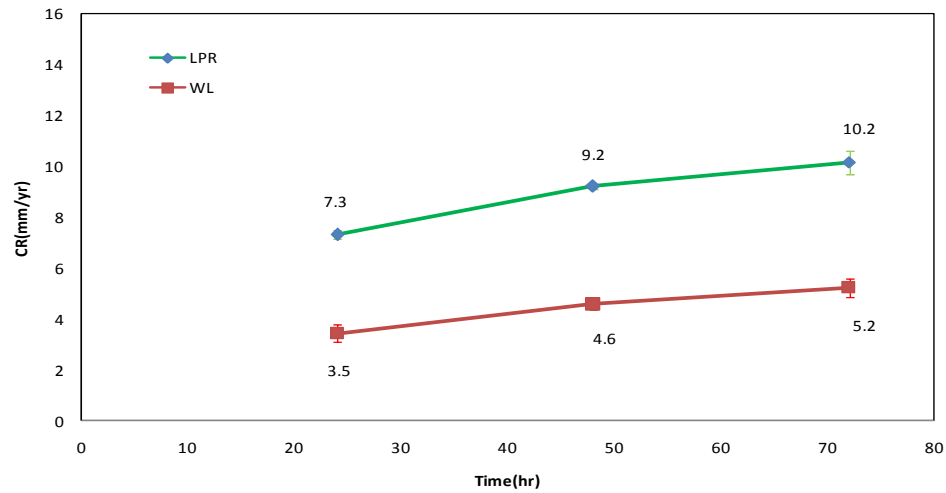


Figure 28. LPR and weight loss corrosion rate vs. time for experiments conducted at pH 5.0 and 60°C on C1018 spheroidized steel.

- C1018 quenched-tempered steel:

Figure 29 shows that the corrosion rate (CR) increased with time for the C1018 quenched-tempered material and that the saturation limit of FeCO_3 was not exceeded.

Figure 25, Figure 27, and Figure 29 show that the corrosion rate increases in each case, but there is a higher corrosion rate for C1018 quenched-tempered material.

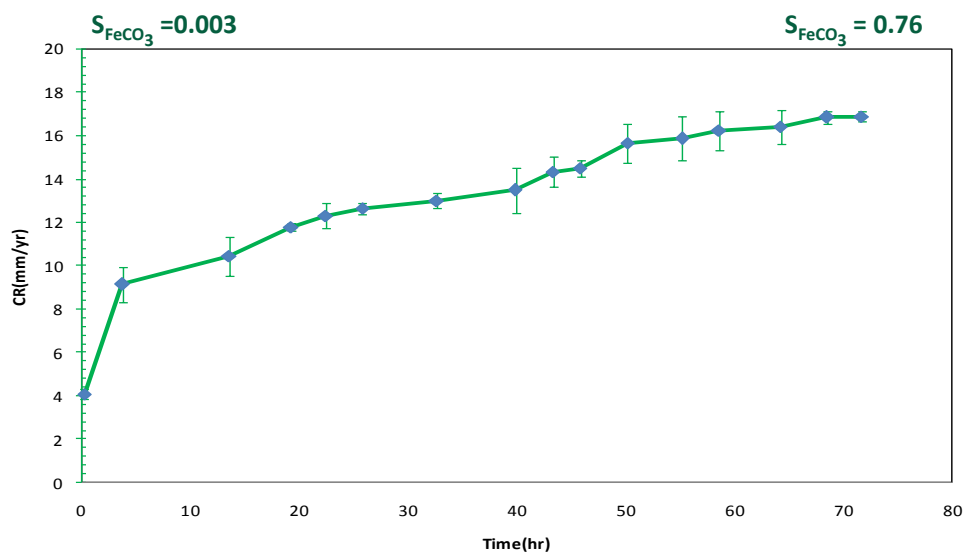


Figure 29. Corrosion rate vs. time for experiments conducted at pH 5.0 and 60°C with C1018 quenched-tempered steel.

As for the previous samples, LPR is measured multiple times per day and the area under the CR versus time curve is integrated for a value. Again, this did not correspond to the weight loss corrosion rate, as shown in Figure 30, for the same reasons as stated above.

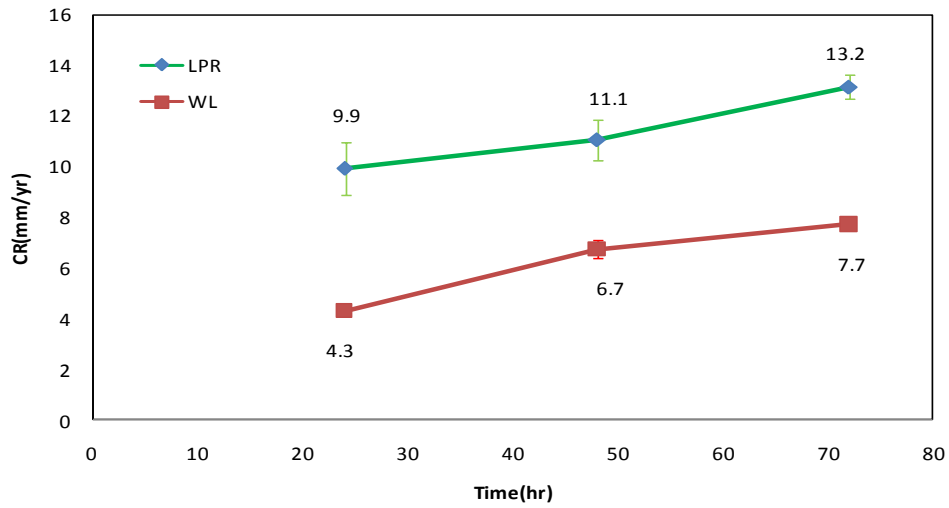


Figure 30. LPR and weight loss corrosion rate vs. time for experiments conducted at pH 5.0 and 60°C on C1018 quenched-tempered steel.

- X65 (0.14 wt. % C) steel:

Figure 31 shows that the corrosion rate (CR) increased with time for the X65 (0.14 wt. % C) material and that the saturation limit of FeCO_3 was not exceeded.

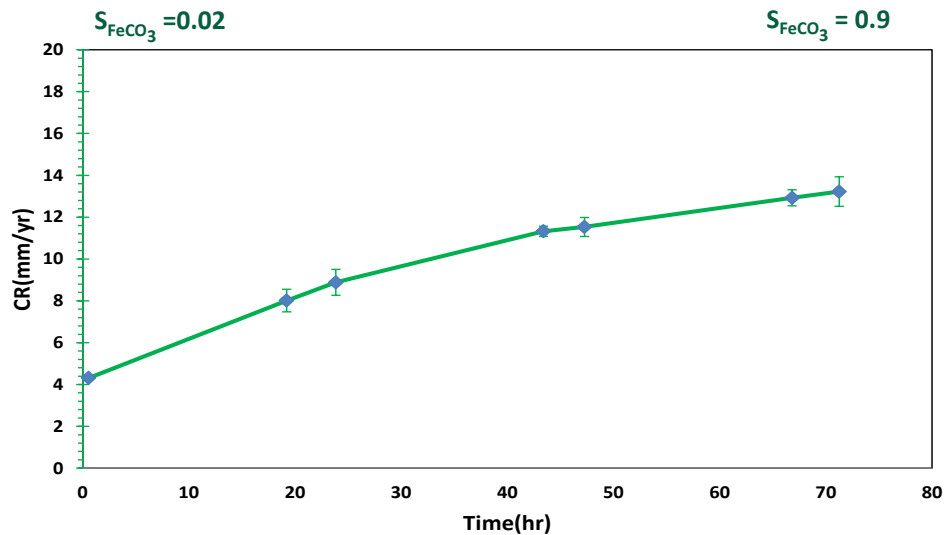


Figure 31. Corrosion rate vs. time for experiments conducted at pH 5.0 and 60°C with X65 (0.14 wt.% C) steel.

Figure 32 again shows that the integrated LPR corrosion rate does not match the weight loss corrosion rate for the same reasons as mentioned above.

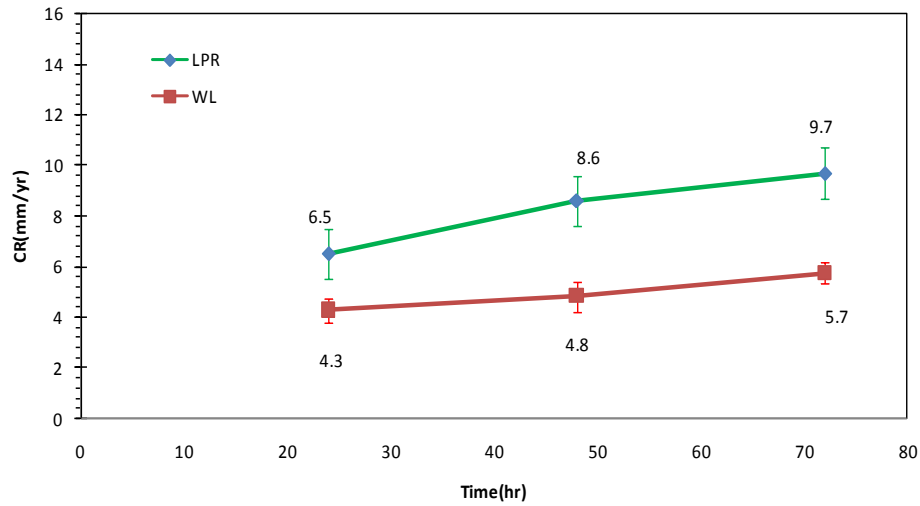


Figure 32. LPR and weight loss corrosion rate vs. time for experiments conducted at pH 5.0 and 60°C on X65 (0.14 wt.% C) steel.

- X65 (0.05 wt. % C) steel:

Figure 33 shows that the corrosion rate (CR) increased with time for the X65 (0.05 wt.% C) material. Figure 31 and Figure 33 show that the corrosion rate increases in each case, but there is a higher corrosion rate for X65 (0.05 wt.% C). Also, the saturation limit of FeCO_3 was not exceeded in either case.

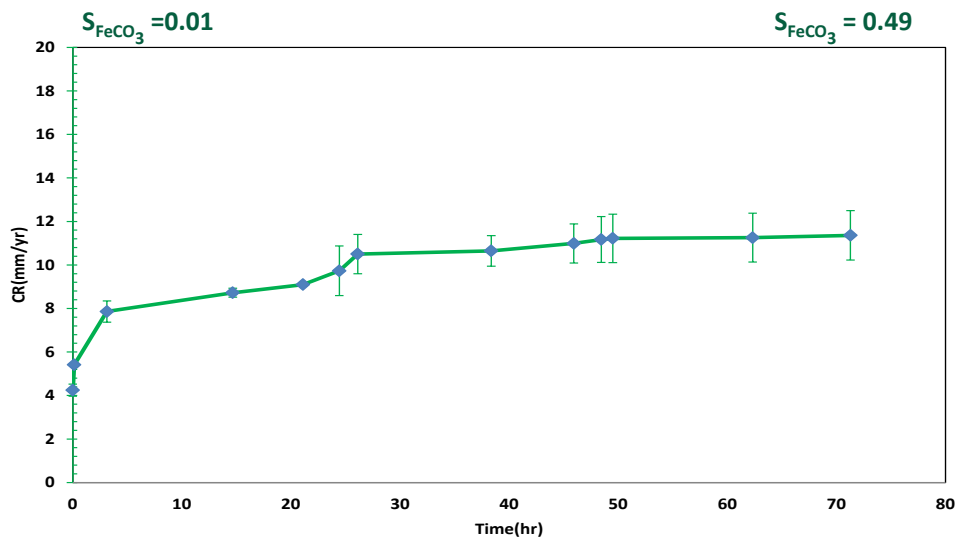


Figure 33. Corrosion rate vs. time for experiments conducted at pH 5.0 and 60°C with X65 (0.05 wt.% C) steel.

Figure 34 again shows that the integrated LPR corrosion rate does not match the weight loss corrosion rate; the reasons being described above.

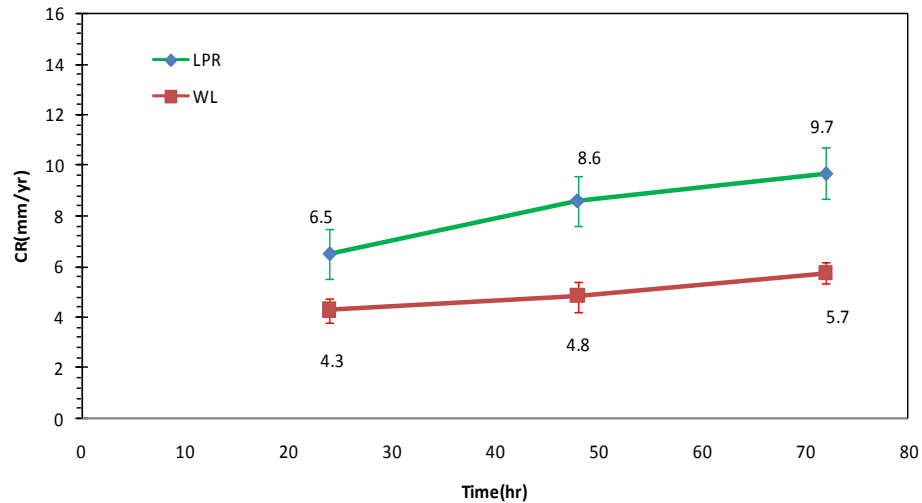


Figure 34. LPR and weight loss corrosion rate vs. time for experiments conducted at pH 5.0 and 60°C on X65 (0.14 wt.% C) steel.

- X65 (0.05 wt. % C) spheroidized steel:

Figure 35 shows that the corrosion rate (CR) increased with time for the X65 (0.05 wt.% C) spheroidized material. Figure 33 and Figure 35 show that the corrosion rate increases for the untreated and heat treated steel, with similar corrosion rates observed in each case. In addition, Figure 27 and Figure 35 show that the corrosion rate increases for each spheroidized steel; however, there is a higher corrosion rate for C1018 spheroidized steel than for X65 (0.05wt. % C) spheroidized steel. Also, the saturation limit of FeCO_3 was not exceeded in either case.

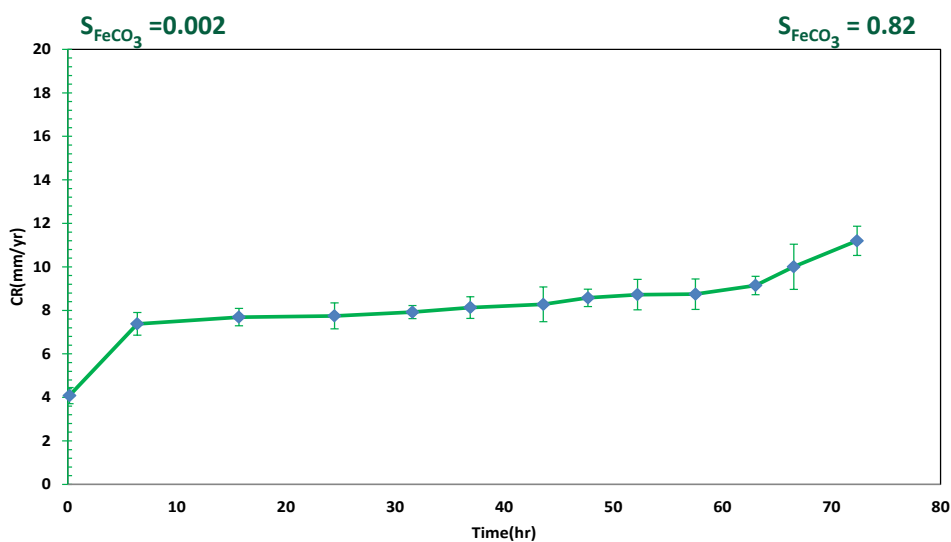


Figure 35. Corrosion rate vs. time for experiments conducted at pH 5.0 and 60°C with X65 (0.05 wt.% C) spheroidized steel.

Figure 36 also shows that the integrated LPR corrosion rate does not match the weight loss corrosion rate. As stated before, the reason these rates do not match is that the LPR value could be related to an incorrect B value, 26 mV/decade, since the surface area has changed with development of iron carbide. Therefore, use of this B value is also likely incorrect.

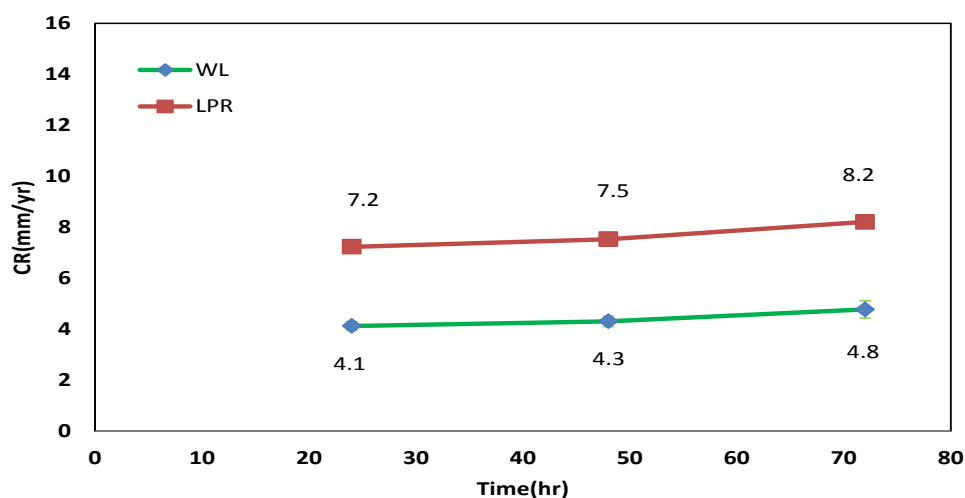


Figure 36. LPR and weight loss corrosion rate vs. time for experiments conducted at pH 5.0 and 60°C on X65 (0.05 wt.% C) spheroidized steel.

Surface Analysis:

- C1018 Ferrite-pearlite steel:

SEM images of top surface areas and cross-sections, respectively, for the pH 5.0 tests at 60°C on C1018 ferrite-pearlite are shown in Figure 37. The surface morphology shows uniform corrosion and no scattered crystals of iron carbonate on the surface. The thickness of the iron carbide increased with time. Figure 37 (d), Figure 37 (e), and Figure 37 (f) show that the iron carbide is present on the surface. This results in higher corrosion rates with time, as shown in Figure 25. The depth of the iron carbide layer for the pH 5.0 tests at 60°C for exposed samples after 1 day, 2 days, and 3 days are shown in Table 10. Corrosion rates were calculated based on the depth of the iron carbide layer for the pH 5.0 tests at 60°C for the exposed sample after days 1, 2, and 3 and are presented in Table

10. Also, Table 10 shows integrated LPR corrosion rates for the pH 5.0 tests at 60°C for the exposed sample after days 1, 2, and 3. Weight loss corrosion rates for the pH 5.0 tests at 60°C for the exposed sample after days 1, 2, and 3 are also displayed in Table 10.

Again, the integrated LPR corrosion rate does not match the depth of the iron carbide and weight loss corrosion rate. However, the uniform corrosion rate calculated from depth of the iron carbide layer matches the weight loss corrosion rate (WL). As a result, it has been possible to calculate a similar corrosion rate to WL by measuring the depth of iron carbide in cross-sectional analysis. Figure 38 shows that when a ferritic-pearlitic microstructure steel, C1018, is corroded, a layer of cementite lamellae containing cavities remains on the steel surface. Figure 39 shows that the iron carbide developed from C1018 steel has carbon and iron, with some oxygen detected.

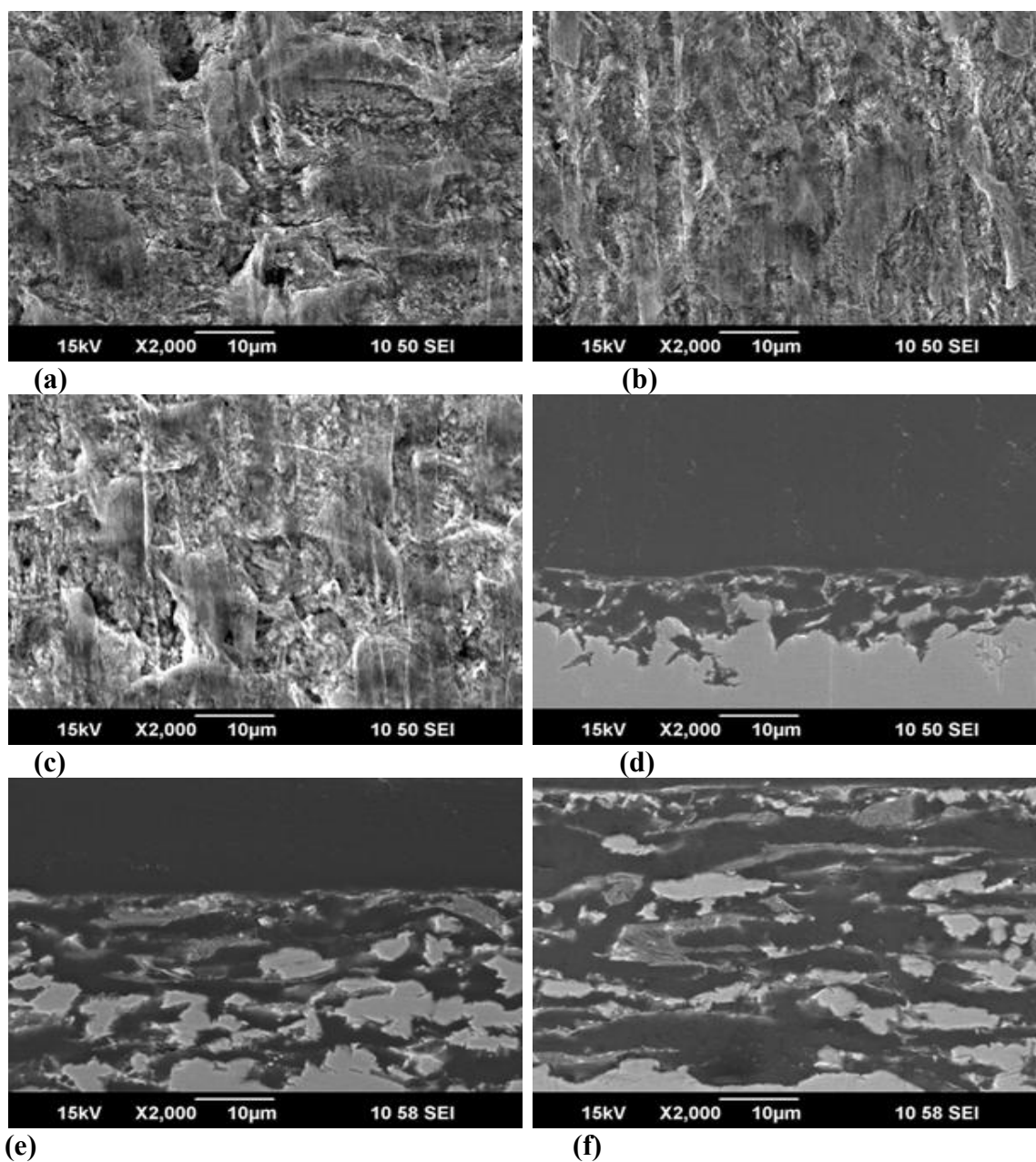


Figure 37. Sample (C1018 Ferrite-Pearlite Steel) for bulk solution pH 5.0 at 60°C (a) SEM image for the surface after 1 day exposure, (b) SEM image for the surface after two day exposure, (c) SEM image for the surface after 3 day exposure, (d) SEM image for the cross-section after 1 day exposure, (e) SEM image for the cross-section after two day exposure, and (f) SEM image for the cross-section after 3 day exposure.

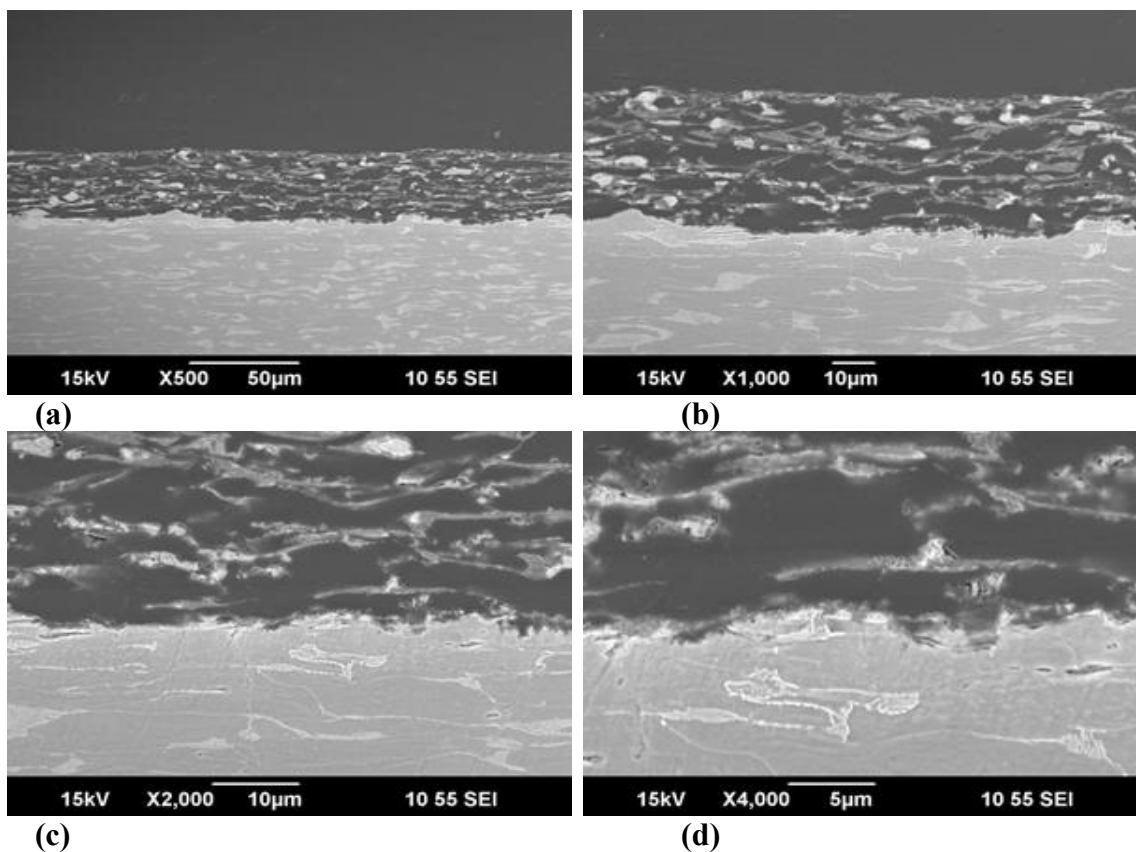


Figure 38. Microstructure of sample (C1018 Ferrite-Pearlite Steel) for bulk solution pH 5.0 at 60°C for the cross-section after 3 days exposure (a) SEM image at 500x magnification , (b) SEM image at 1000x magnification, (c) SEM image at 2000x magnification, and (d) SEM image at 4000x magnification.

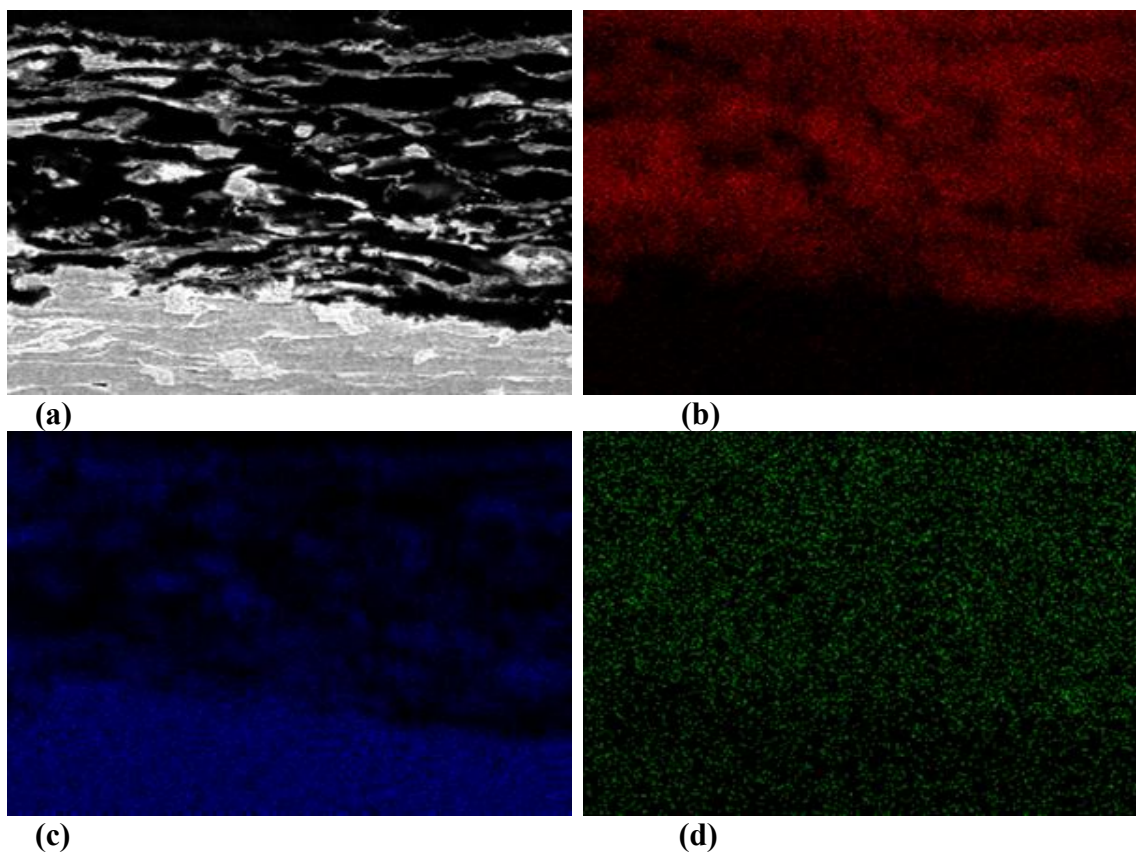


Figure 39. Elemental mapping of C1018 Ferrite-Pearlite Steel sample surface after recovery from bulk solution of pH 5.0 at 60°C for the cross-section after 3 days exposure at 2000x magnification (a) SEM image, (b) carbon distribution map (c) iron map, and (d) oxygen map.

Table 10
Thickness of Iron Carbide for C1018 Ferrite-Pearlite Steel

Test No.	Time	Thickness of Fe ₃ C	Depth CR	Integrated LPR CR	WL
		(μm)	(mm/yr)	(mm/yr)	(mm/yr)
pH=5.0, T=60 °C					
1	1 day	12.2 +0.04/-0.10	4.5 +0.6/-1.7	6.1 \pm 0.5	4.2 \pm 0.05
2	2 days	25.7 +2.3/-4.7	4.7 +0.9/-1.7	7.5 \pm 0.6	4.3 \pm 0.2
3	3 days	42.5 +3.1/-3.6	5.2 +1.1/-1.3	8.2 \pm 0.5	5.2 \pm 0.05

- C1018 spheroidized steel:

SEM images of top surface areas and cross-sections, respectively, for the pH 5.0 tests at 60°C on C1018 spheroidized steel are shown in Figure 40. Uniform corrosion and no scattered crystals of iron carbonate on the surface are shown based on the surface morphology. Also, the thickness of the iron carbide increased with time according to the surface morphology. Figure 40 (d), Figure 40 (e), and Figure 40 (f) show that the iron carbide is present on the surface. This results in higher corrosion rates with time, as shown in Figure 27. The depth of the iron carbide layer for the pH 5.0 tests at 60°C for exposed samples after 1 day, 2 days, and 3 days are presented in Table 11. Corrosion rates were calculated based on the depth of the iron carbide layer for the pH 5.0 tests at 60°C for the exposed sample after days 1, 2, and 3 and are displayed in Table 11. This table also shows integrated LPR and weight loss corrosion rates for the pH 5.0 tests at 60°C for the exposed sample after days 1, 2, and 3. Again, the integrated LPR corrosion

rate does not match with the depth of the iron carbide and weight loss corrosion rate. In addition, the depth of the iron carbide also does not match with the weight loss corrosion rate, unlike for the unspheroidized ferritic-pearlitic parent material. As mentioned, weight loss is the best measurement used to be sure about the corrosion rate. Expected depths of iron carbide layers were back calculated based upon weight loss data for the corroded C1018 spheroidized samples as shown in Figure 41. Figure 42 shows that when a ferrite with large spherical cementite particles in the steel microstructure, C1018 spheroidized steel, is corroded, a layer of large spherical cementite particles remain on the surface. Also, this layer is discontinuous on the surface. In the case of each type of steel, the corrosion rate increases, but there is a higher corrosion rate for C1018 spheroidized. This can be hypothesized to be due to the presence of lamellar carbides in the C1018 ferrite-pearlite, which contain cavities that permit the development of local aqueous conditions that favor FeCO_3 nucleation and crystal growth. Mild steels with such structures have been reported to undergo less severe corrosion as compared to mild steels with ferrite-spheroidized cementite particle structures, such as the C1018 spheroidized steel [32]. However, FeCO_3 was undetected so this is unlikely to be responsible for the difference in corrosion rates. In addition, experiments show that iron carbide layer development is dependent upon the microstructure of the carbon steel from which it is derived. Figure 43 shows that the iron carbide developed from C1018 spheroidized steel has carbon and iron, with some oxygen detected.

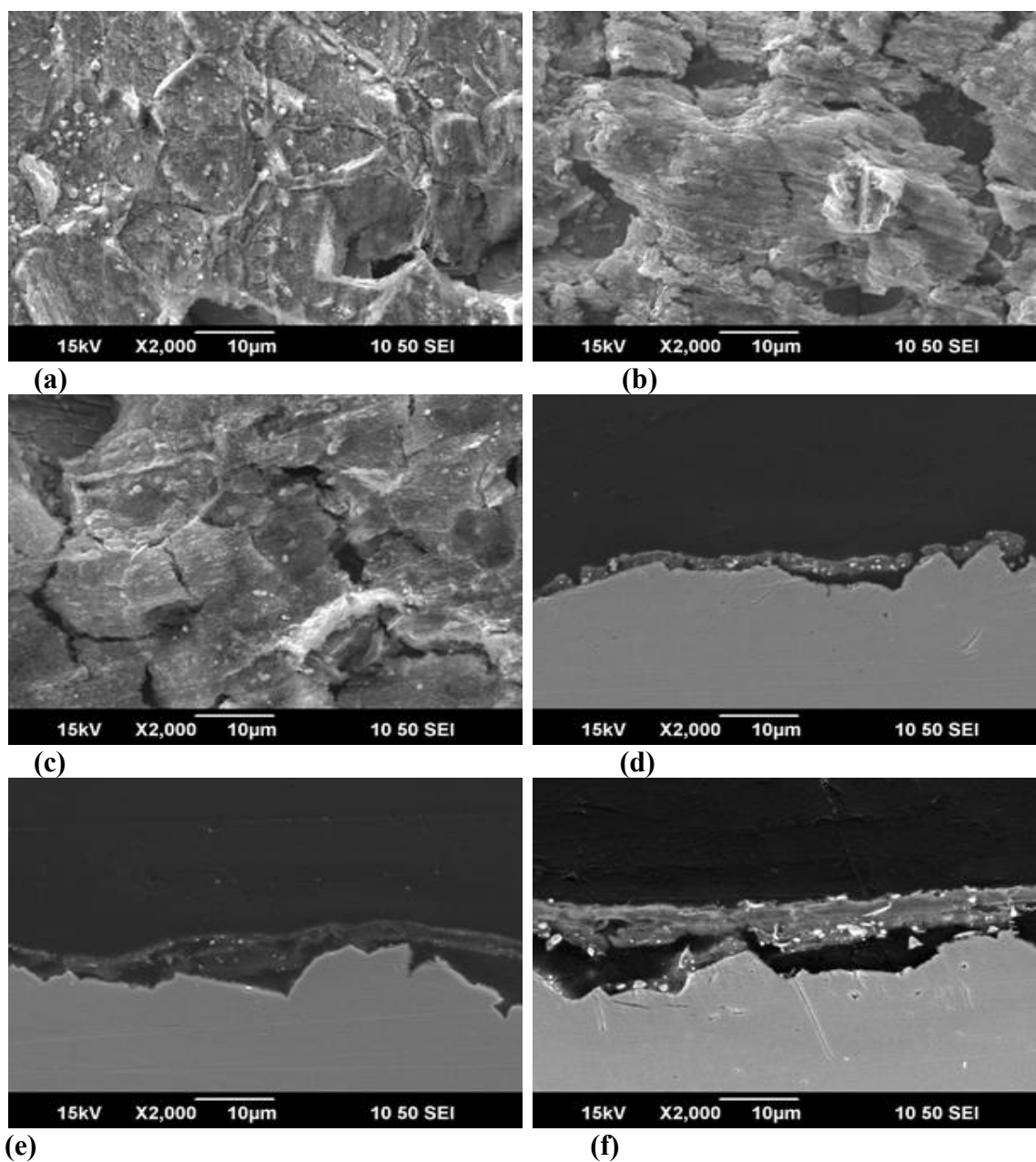
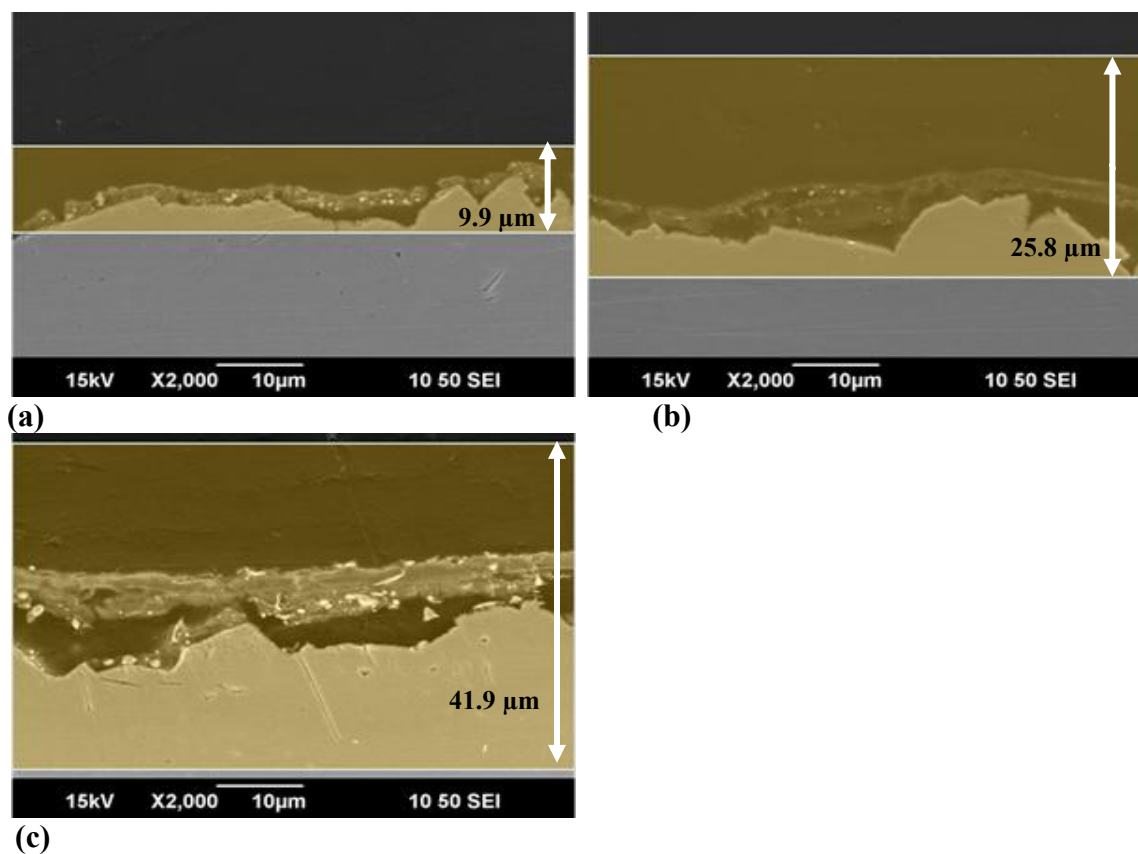


Figure 40. Sample (C1018 spheroidized steel) for bulk solution pH 5.0 at 60°C (a) SEM image for the surface after 1 day exposure, (b) SEM image for the surface after two day exposure, (c) SEM image for the surface after 3 day exposure, (d) SEM image for the cross-section after 1 day exposure, (e) SEM image for the cross-section after two day exposure, and (f) SEM image for the cross-section after 3 day exposure.



(a) **(b)** **(c)**
Figure 41. Expected Fe_3C layer depth on C1018 spheroidized steel from bulk solution pH 5.0 at 60°C (a) SEM image for the cross-section after 1 day exposure, (b) SEM image for the cross-section after 2 day exposure, and (c) SEM image for the cross-section after 3 day exposure.

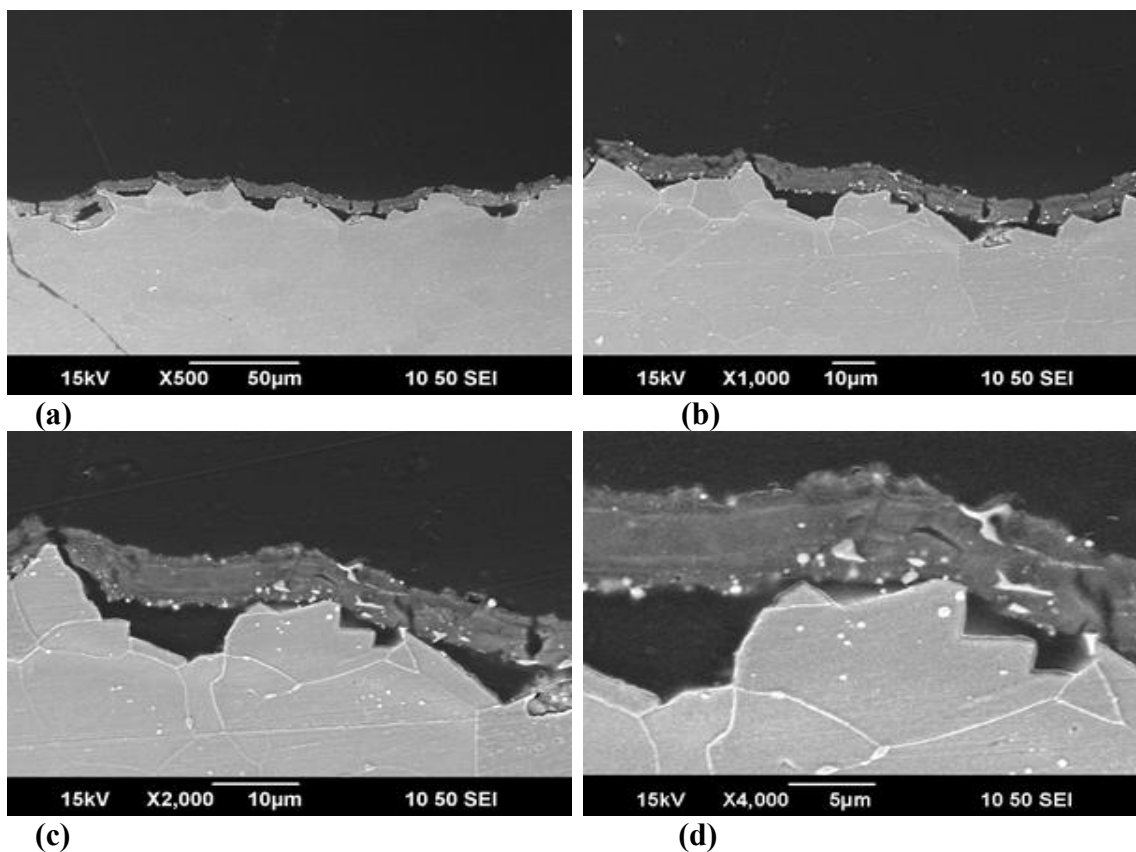


Figure 42. Microstructure of sample (C1018 spheroidized steel) for bulk solution pH 5.0 at 60°C for the cross-section after 3 days exposure (a) SEM image at 500x magnification, (b) SEM image at 1000x magnification, (c) SEM image at 2000x magnification, and (d) SEM image at 4000x magnification.

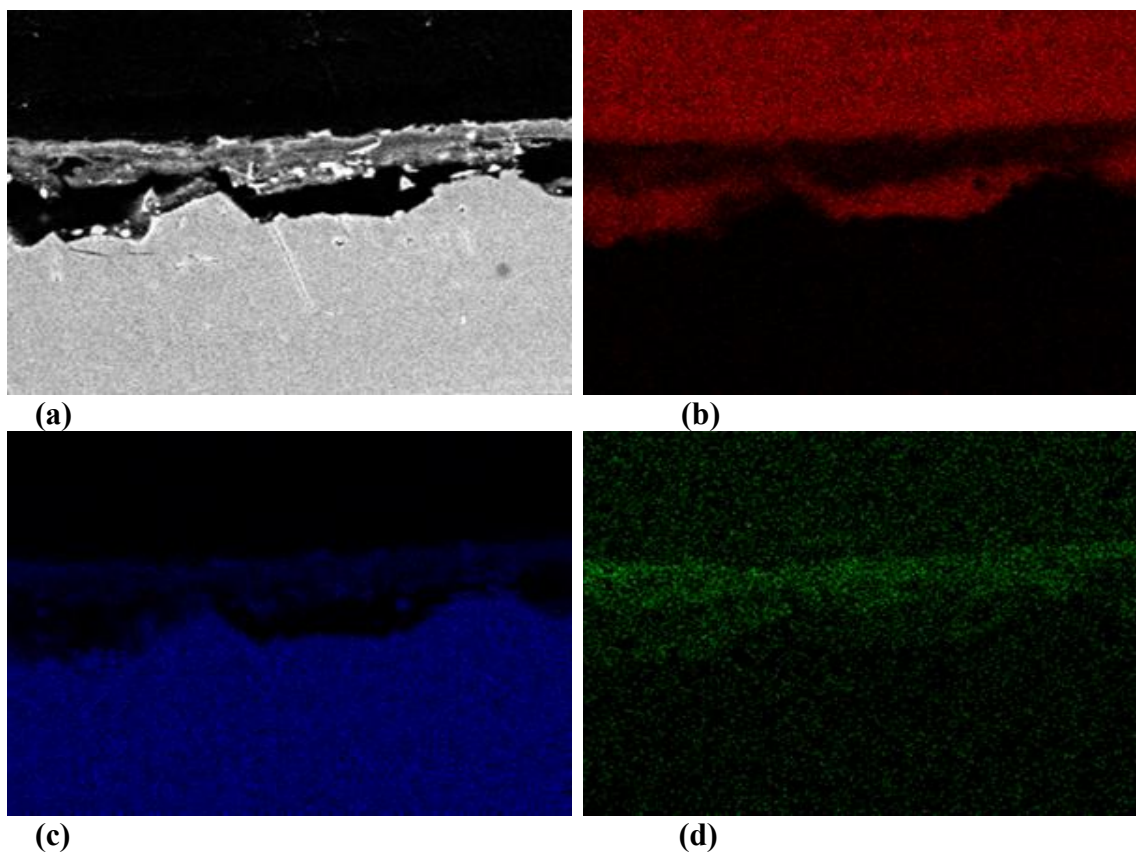


Figure 43. Elemental mapping of C1018 spheroidized steel sample surface after recovery from bulk solution of pH 5.0 at 60°C for the cross-section after 3 days exposure at 2000x magnification (a) SEM image, (b) carbon distribution map (c) iron map, and (d) oxygen map.

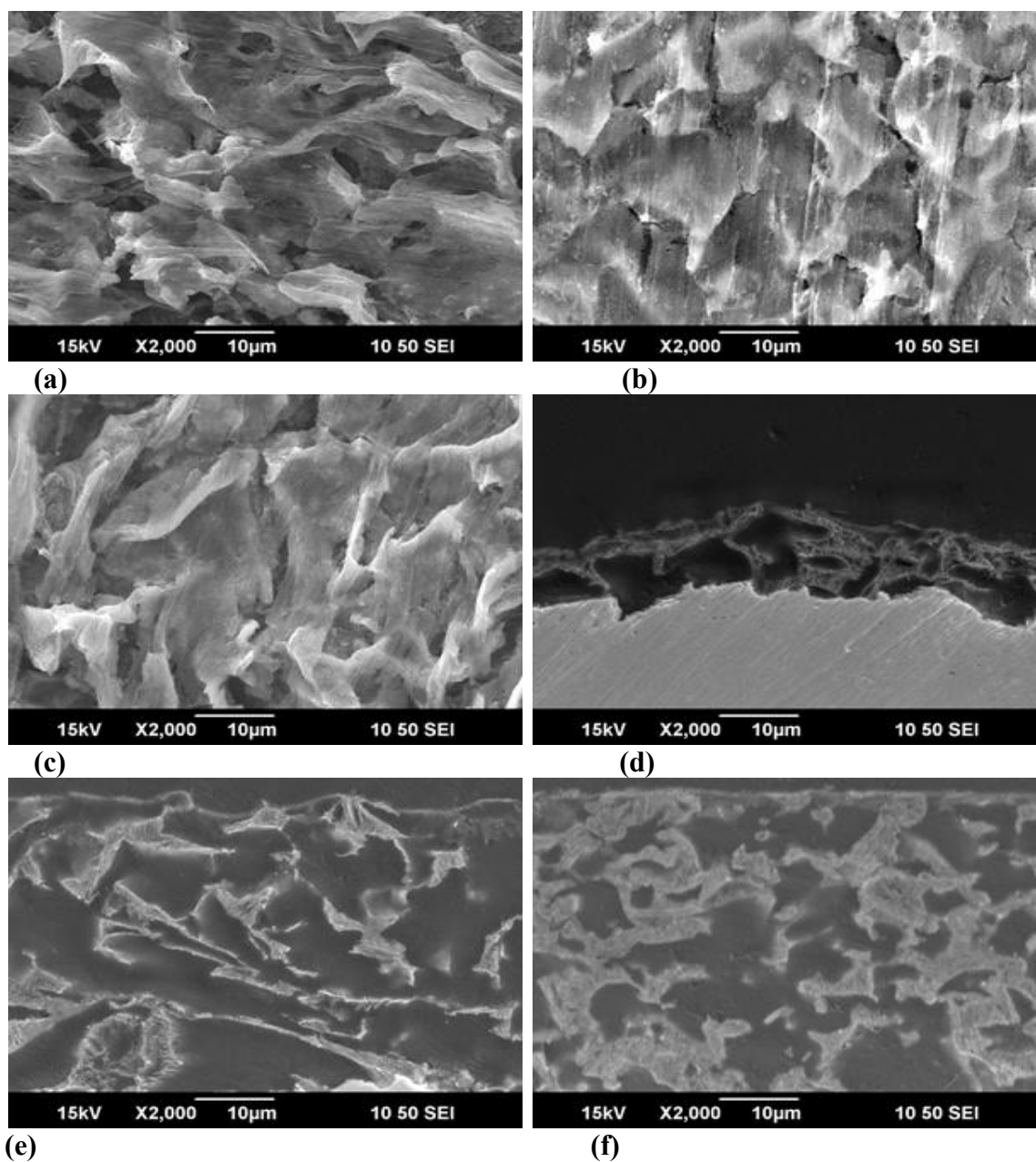
Table 11
Thickness of Iron Carbide for C1018 Spheroidized Steel

Test No.	Time	Thickness of Fe ₃ C	Depth CR	Integrated LPR CR	WL
		(μm)	(mm/yr)	(mm/yr)	(mm/yr)
pH=5.0, T=60 °C					
1	1 day	4.6 +0.9/-0.6	1.7 +0.3/-0.2	7.3 \pm 0.1	3.5 \pm 0.2
2	2 days	7.5 +2.8/-3.5	1.4 +1.0/-1.3	9.2 \pm 0.05	4.6 \pm 0.1
3	3 days	10.5 +1.6/-1.7	1.3 +0.59/-0.63	10.2 \pm 0.3	5.2 \pm 0.2

- C1018 quenched-tempered steel:

SEM images of top surface areas and cross-sections, respectively, for the pH 5.0 tests at 60°C on C1018 quenched-tempered steel are shown in Figure 44. The surface morphology shows uniform corrosion and no present of iron carbonate on the steel surface. The thickness of the iron carbide increased with time. Figure 44 (d), Figure 44 (e), and Figure 44 (f) show that the iron carbide is present on the surface. This results in higher corrosion rates with time, as shown in Figure 29. The depth of the iron carbide layer and calculated corrosion rates based on the depth of the iron carbide layer for the pH 5.0 tests at 60°C for exposed samples after 1 day, 2 days, and 3 days are shown in Table 12. Integrated LPR and WL corrosion rates for the pH 5.0 tests at 60°C for the exposed sample after days 1, 2, and 3 are displayed in Table 12. Again, the integrated LPR corrosion rate does not match the depth of the iron carbide and weight loss corrosion rate. However, the uniform corrosion rate calculated from the depth of the iron carbide layer matches the weight loss corrosion rate (WL). As a result, it has been possible to

calculate a similar corrosion rate to WL by measuring the depth of iron carbide in cross-sectional analysis. Figure 45 shows that when C1018 quenched-tempered steel is corroded, a layer of cementite with a lot of cavities remains on the steel surface. Mild steels with such structures underwent more severe corrosion as compared to mild steels with ferrite-pearlite structures [32]. Again, experiments show that iron carbide layer development is dependent upon the microstructure of the carbon steel from which it is derived. Figure 46 shows the presence of iron carbide developed from C1018 quenched-tempered steel.



(a) **(b)**
(c) **(d)**
(e) **(f)**

Figure 44. Sample (C1018 quenched-tempered steel) for bulk solution pH 5.0 at 60°C (a) SEM image for the surface after 1 day exposure, (b) SEM image for the surface after two day exposure, (c) SEM image for the surface after 3 day exposure, (d) SEM image for the cross-section after 1 day exposure, (e) SEM image for the cross-section after two day exposure, and (f) SEM image for the cross-section after 3 day exposure.

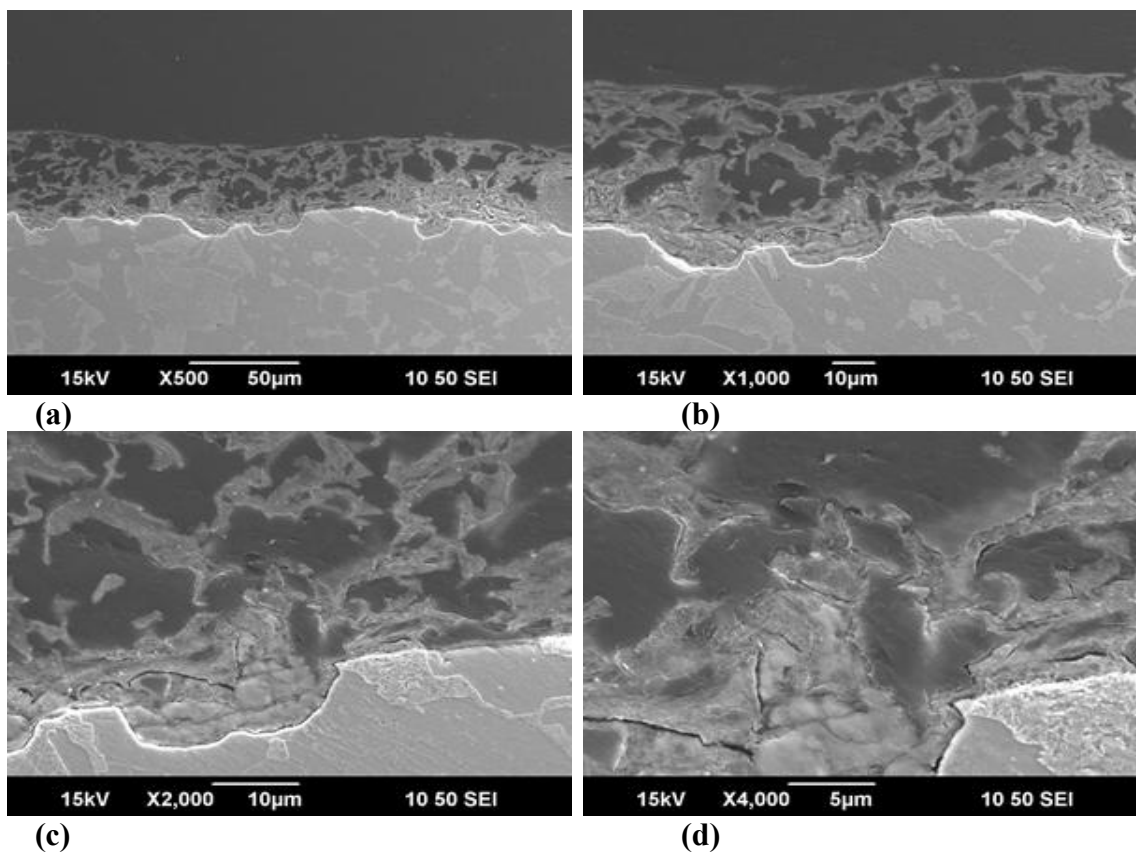


Figure 45. Microstructure of sample (C1018 quenched-tempered steel)) for bulk solution pH 5.0 at 60°C for the cross-section after 3 days exposure (a) SEM image at 500x magnification, (b) SEM image at 1000x magnification, (c) SEM image at 2000x magnification, and (d) SEM image at 4000x magnification.

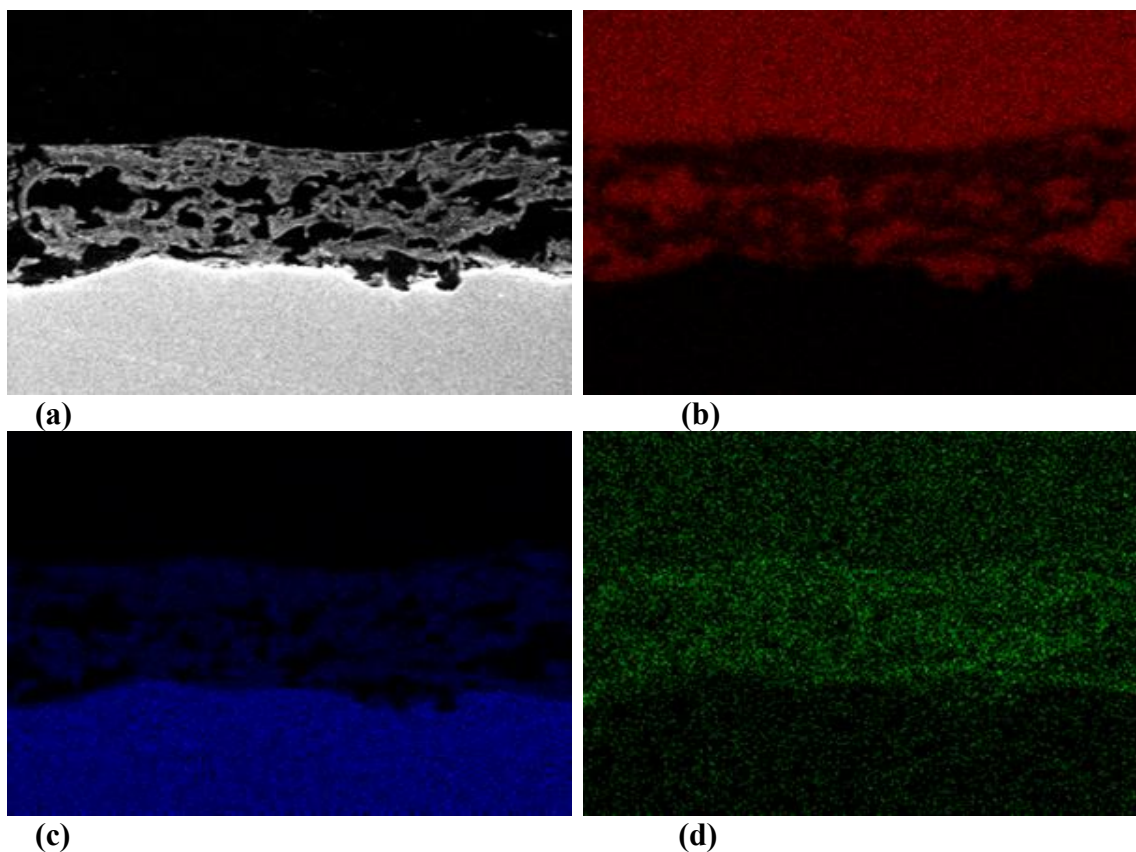


Figure 46. Elemental mapping of C1018 quenched-tempered steel sample surface after recovery from bulk solution of pH 5.0 at 60°C for the cross-section after 3 days exposure at 2000x magnification (a) SEM image, (b) carbon distribution map (c) iron map, and (d) oxygen map.

Table 12
Thickness of Iron Carbide for C1018 Quenched-Tempered Steel

Test No.	Time	Thickness of Fe ₃ C	Depth CR	Integrated LPR CR	WL
		(μm)	(mm/yr)	(mm/yr)	(mm/yr)
pH=5.0, T=60 °C					
1	1 day	11.1 +2.0/-4.1	4.1 +0.7/-1.5	9.9 \pm 0.6	4.3 \pm 0.2
2	2 days	36.8 +0.0/-3.5	6.7 +0.0/-1.3	11.1 \pm 0.4	6.7 \pm 0.2
3	3 days	57.2 +3.5/-3.5	7.0 +1.3/-1.3	13.2 \pm 0.3	7.7 \pm 0.1

- X65 (0.14 wt. % C) steel:

SEM images of top surface areas and cross-sections, respectively, for the pH 5.0 tests at 60°C on X65 (0.14 wt. % C) are shown in Figure 47. The surface morphology shows uniform corrosion and no present of iron carbonate on the surface. Also, the thickness of the iron carbide increased with time. Figure 47 (d), Figure 47 (e), and Figure 47 (f) show that the iron carbide is present on the surface. This results in higher corrosion rates with time, as shown in Figure 31. Table 13 displays the depth of the iron carbide layer and calculated corrosion rates based on the depth of the iron carbide layer for the pH 5.0 tests at 60°C for the exposed samples after 1 day, 2 days, and 3 days. Also, Table 13 presents the integrated LPR and WL corrosion rates for the pH 5.0 tests at 60°C for the exposed sample after days 1, 2, and 3. The integrated LPR corrosion rate does not match with depth of the iron carbide and weight loss corrosion rate. In addition, the depth of the iron carbide also does not match with weight loss corrosion rate. As mentioned,

weight loss measurement is the best measurement used to be sure about the corrosion rate.

Expected depths of iron carbide layers were back calculated based upon weight loss data for the corroded X65 (0.14 wt.% C) samples as shown in Figure 48. Figure 49 shows that when ferrite with discrete cementite particles in the steel microstructure is corroded, a layer of continuous discrete cementite particles remained on the surface. In addition, experiments show that iron carbide layer development is dependent upon the microstructure of the carbon steel from which it is derived. Figure 50 shows that the primarily iron carbide residual layer developed from X65 (0.14 wt.% C) steel has carbon, iron, and oxygen, as well as the alloying elements manganese, and molybdenum.

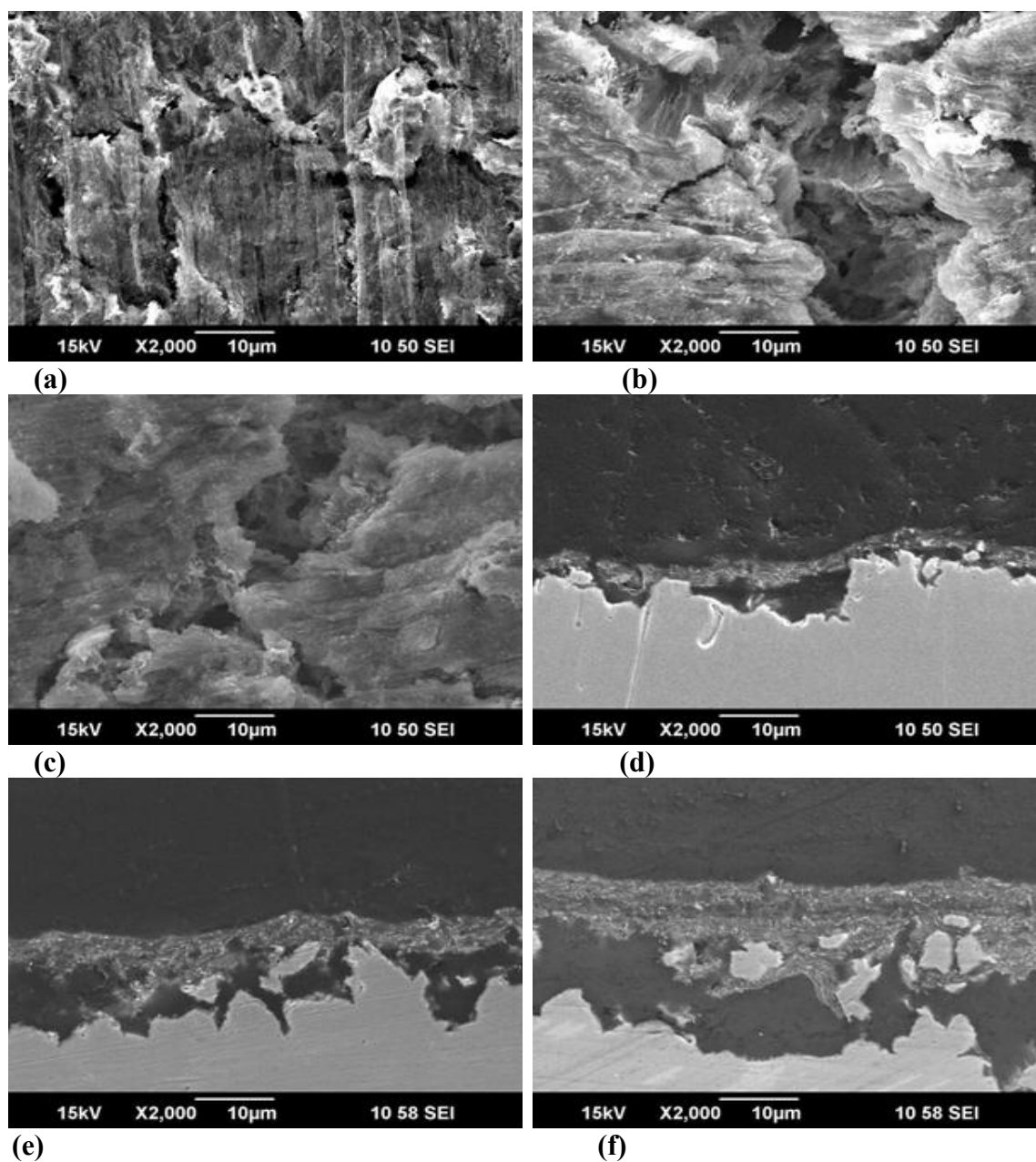
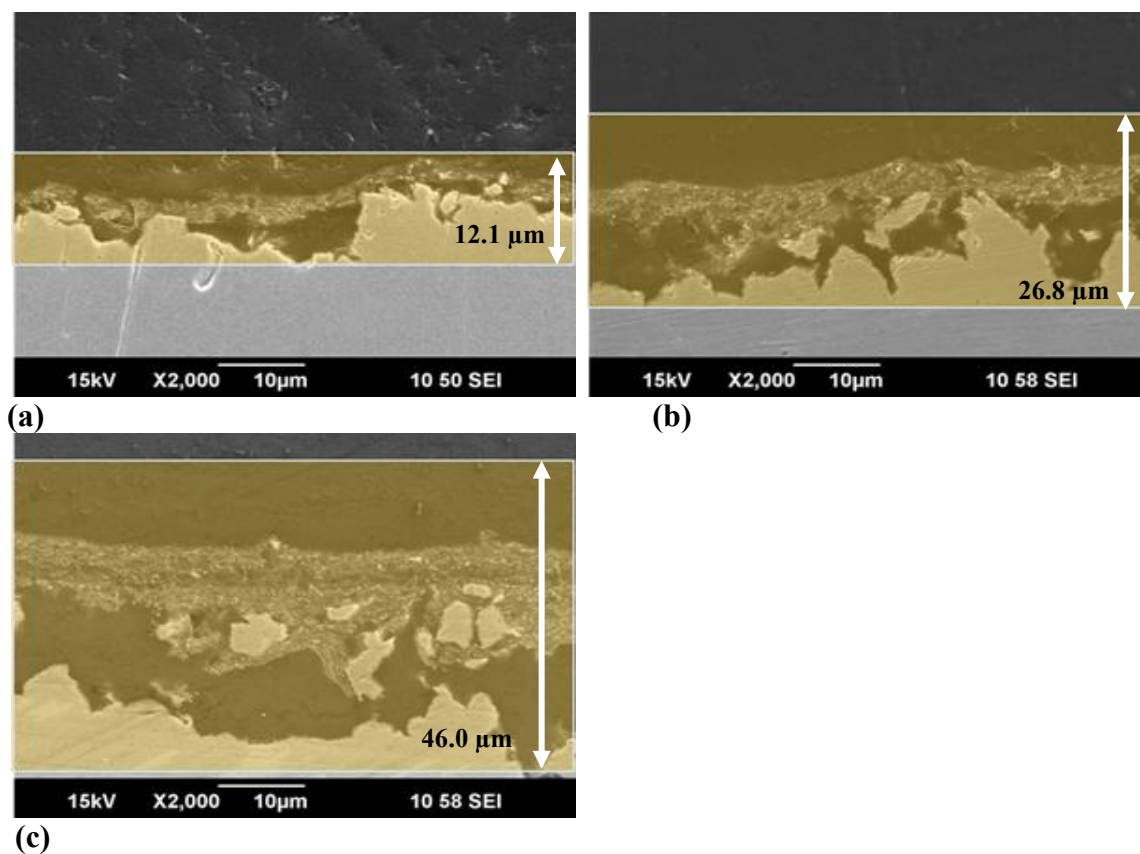


Figure 47. Sample [X65 (0.14 wt.% C)] from bulk solution at pH 5.0 at 60°C (a) SEM image for the surface after 1 day exposure, (b) SEM image for the surface after two day exposure, (c) SEM image for the surface after 3 day exposure, (d) SEM image for the cross-section after 1 day exposure, (e) SEM image for the cross-section after two day exposure, and (f) SEM image for the cross-section after 3 day exposure.



(c)
Figure 48. Expected Fe_3C layer depth on X65 (0.14 wt.% C) from bulk solution pH 5.0 at 60°C (a) SEM image for the cross-section after 1 day exposure, (b) SEM image for the cross-section after 2 day exposure, and (c) SEM image for the cross-section after 3 day exposure.

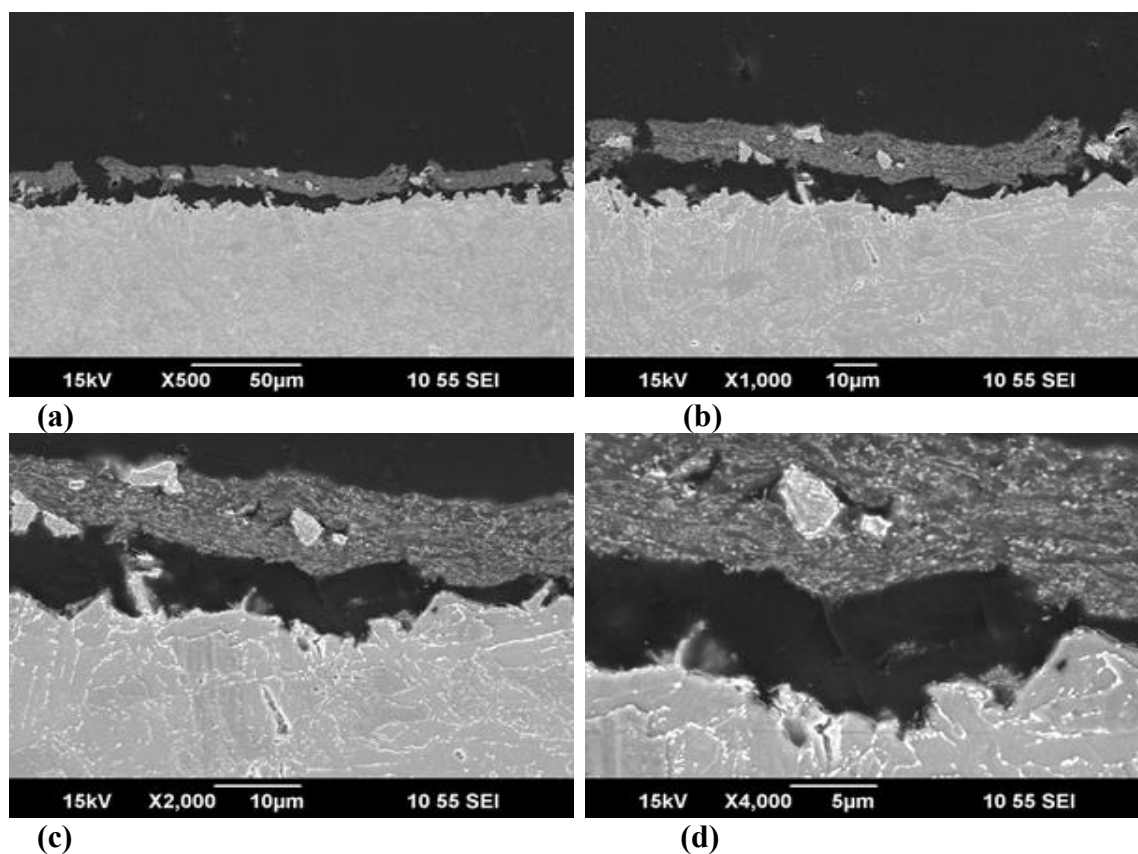
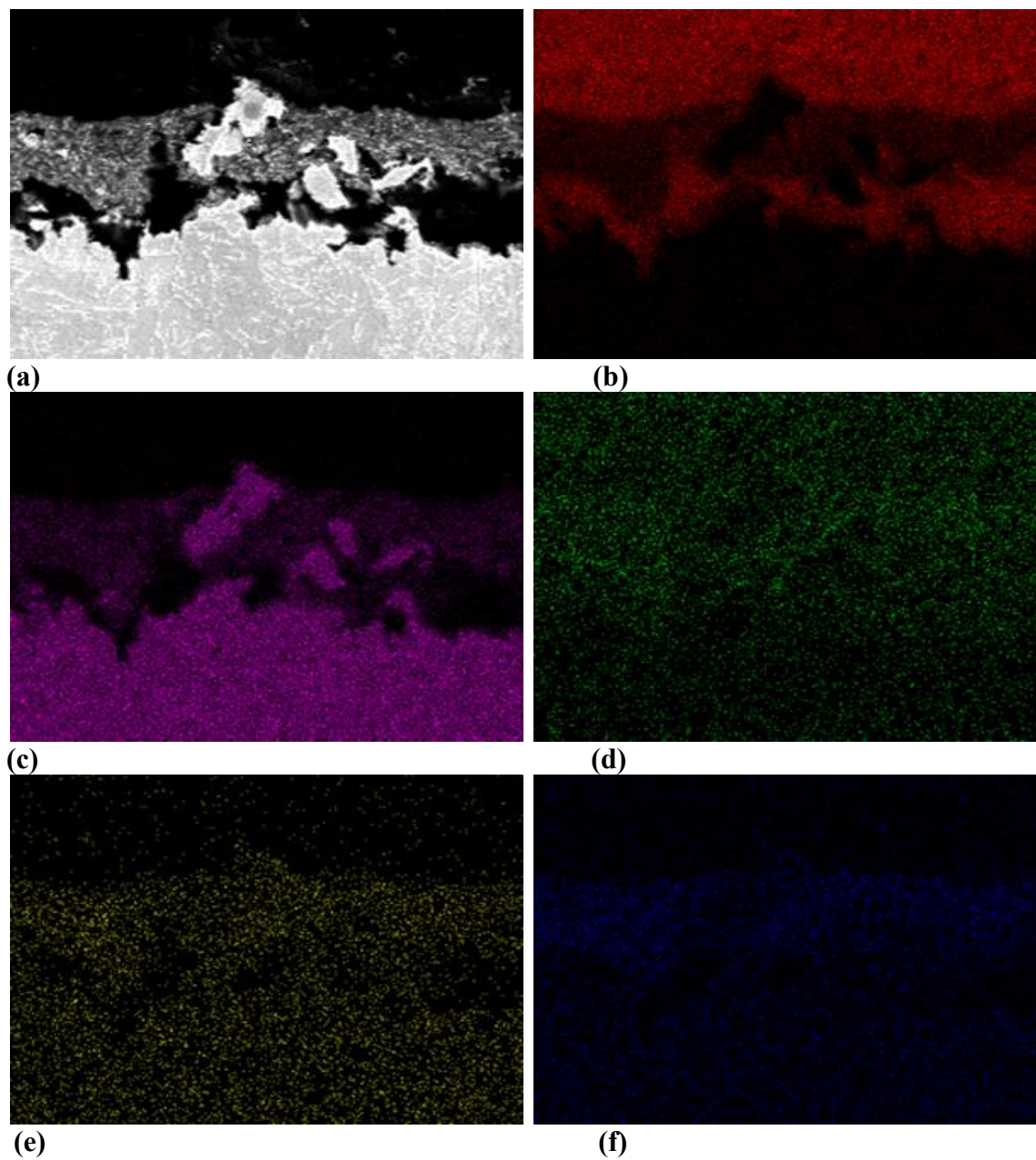


Figure 49. Microstructure of X65 (0.14 wt.% C) recovered from bulk solution at pH 5.0 and 60°C for 3 days of exposure (a) SEM image of cross-section at 500 x magnifications, (b) SEM image at 1000x magnification, (c) SEM image at 2000x magnification, and (d) SEM image at 4000x magnification.



(a) SEM image of cross-section, **(b)** carbon distribution map **(c)** iron map **(d)** oxygen map **(e)** manganese map, and **(f)** molybdenum map.

Figure 50. Elemental mapping of X65 (0.14 wt.% C) sample surface after recovery from bulk solution of pH 5.0 at 60°C for the cross-section after 3 days exposure at 2000x magnification

Table 13
Thickness of Iron Carbide for X65 (0.14 wt. % C) Steel

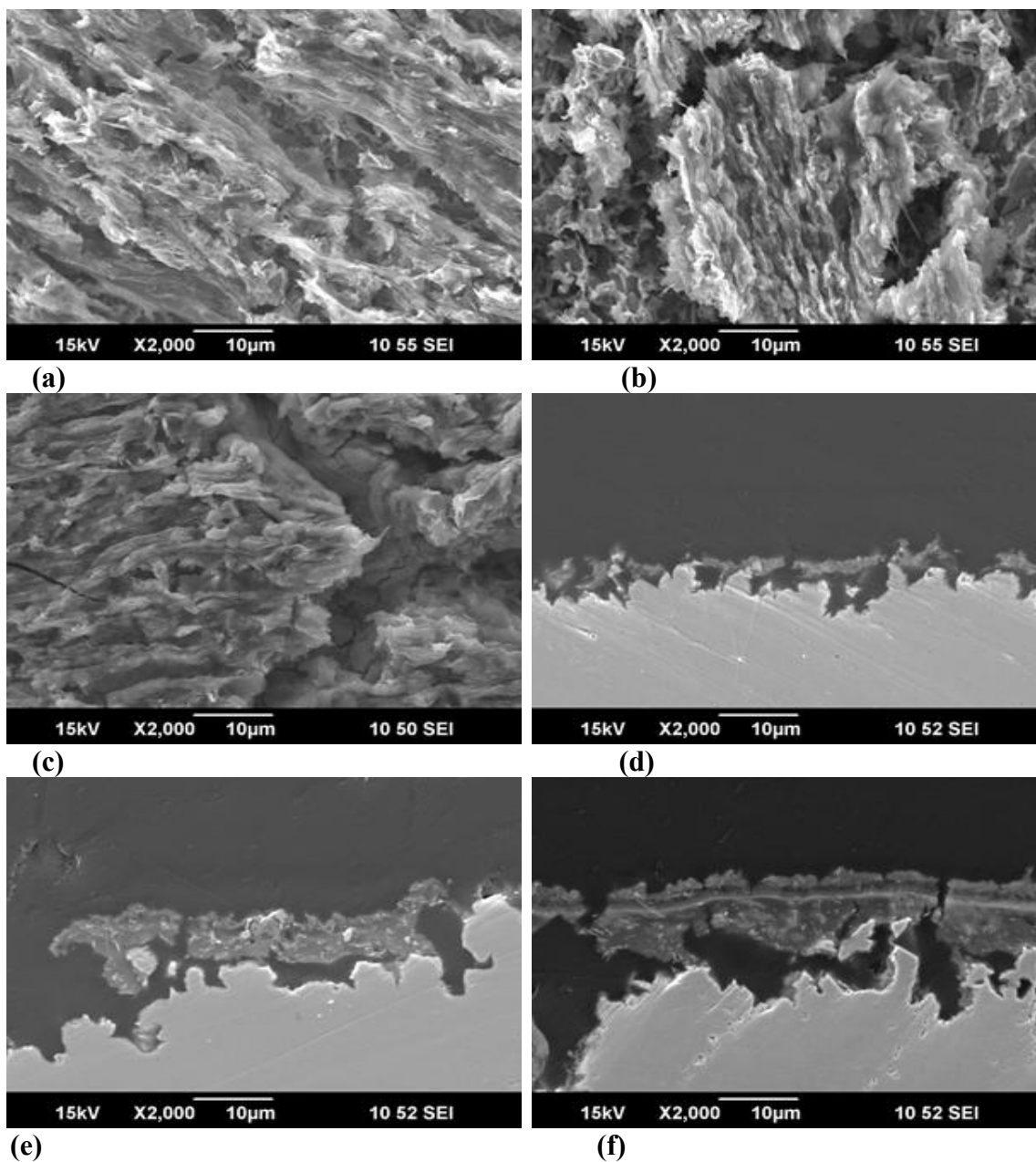
Test No.	Time	Thickness of Fe ₃ C (μm)	Depth CR (mm/yr)	Integrated LPR CR (mm/yr)	WL (mm/yr)
pH=5.0, T=60 °C					
1	1 day	7.7 +2.5/-2.4	2.8 +0.90/-0.88	6.5 \pm 0.2	4.3 \pm 0.3
2	2 days	16.4 +4.6/-4.0	3.0 +1.7/-1.5	8.6 \pm 0.2	4.8 \pm 0.3
3	3 days	32.8 +2.1/-9.0	4.0 +0.8/-3.3	9.7 \pm 0.2	5.7 \pm 0.2

- X65 (0.05 wt. % C) steel:

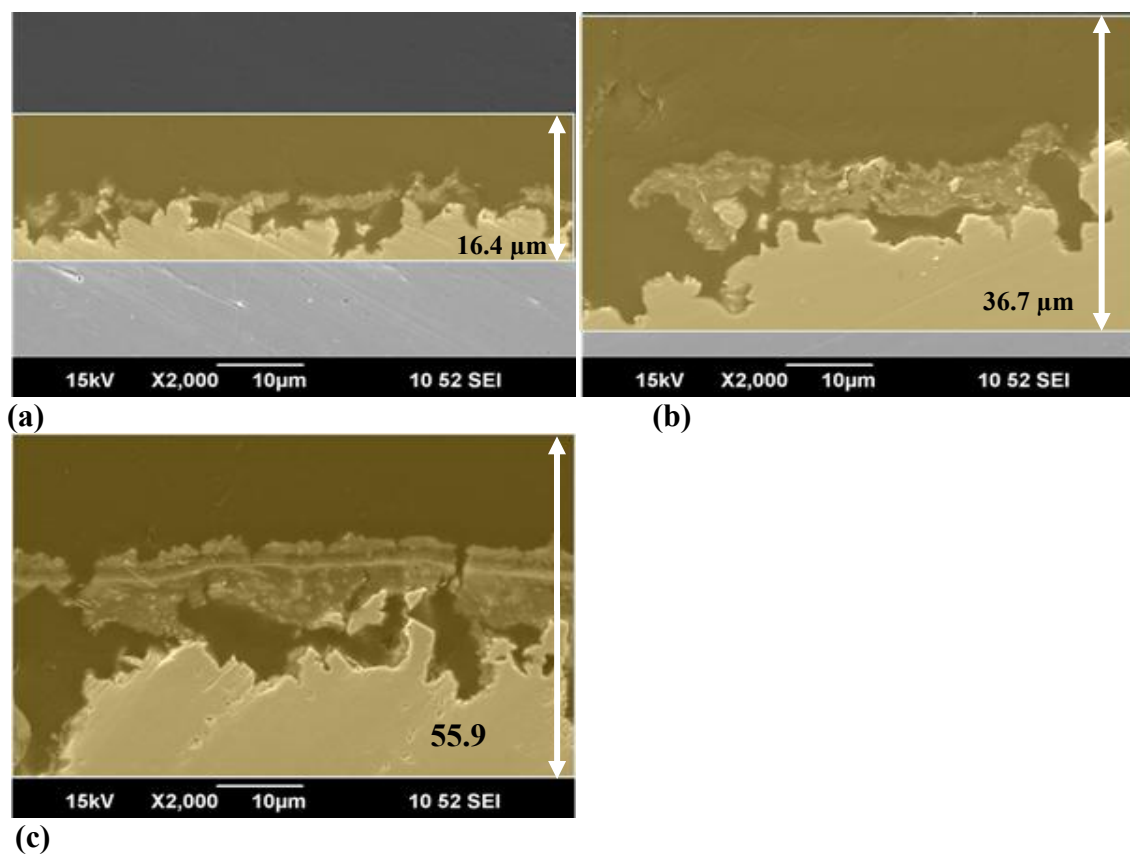
SEM images of top surface areas and cross-sections, respectively, for the pH 5.0 tests at 60°C on X65 (0.05 wt. % C) are shown in Figure 51. The surface morphology shows uniform corrosion and no scattered crystals of the iron carbonate on the surface. The thickness of the iron carbide increased with time. Figure 51 (d), Figure 51 (e), and Figure 51 (f) show that the iron carbide is present on the surface. This results in higher corrosion rates with time, as shown in Figure 33. The depth of the iron carbide layer and calculated corrosion rates based on the depth of the iron carbide layer for the pH 5.0 tests at 60°C for the exposed samples after 1 day, 2 days, and 3 days are presented in Table 14. Also, Table 14 shows the integrated LPR and WL corrosion rates for the pH 5.0 tests at 60°C for the exposed sample after days 1, 2, and 3. The integrated LPR corrosion rate does not match with the depth of the iron carbide and weight loss corrosion rate. In addition, the depth of the iron carbide also does not match with the weight loss corrosion

rate. As mentioned, weight loss measurement is the best measurement used to be sure about the corrosion rate.

Expected depths of iron carbide layers were back calculated based upon weight loss data for the corroded X65 (0.05 wt. % C) samples as shown in Figure 52. Figure 53 shows that when ferrite with discrete cementite particles in the steel microstructure, X65 (0.05 wt. % C), is corroded, a layer of discrete cementite particles remained on the surface. However, this layer is discontinuous on the steel surface. In the case of each type of steel, the corrosion rate increases, but there is a higher corrosion rate for X65 (0.14 wt. % C). In addition, experiments show that iron carbide layer development is dependent upon the microstructure of the carbon steel from which it is derived. Figure 54 shows that the primarily iron carbide layer developed from X65 (0.05 wt. % C) steel has carbon, iron, oxygen, manganese, and molybdenum. Also, the Raman analysis shows that there is no iron carbonate present on the corroded sample after 1, 2, and 3 days, as shown in Figure 55; no vibrational mode is detected at 1086cm^{-1} , which would be indicative of the presence of CO_3^{2-} .



(a) SEM image for the surface after 1 day exposure, **(b)** SEM image for the surface after two day exposure, **(c)** SEM image for the surface after 3 day exposure, **(d)** SEM image for the cross-section after 1 day exposure, **(e)** SEM image for the cross-section after two day exposure, and **(f)** SEM image for the cross-section after 3 day exposure.



(a) (b) (c)
Figure 52. Expected Fe₃C layer depth on X65 (0.05 wt.% C) from bulk solution pH 5.0 at 60°C (a) SEM image for the cross-section after 1 day exposure, (b) SEM image for the cross-section after 2 day exposure, and (c) SEM image for the cross-section after 3 day exposure.

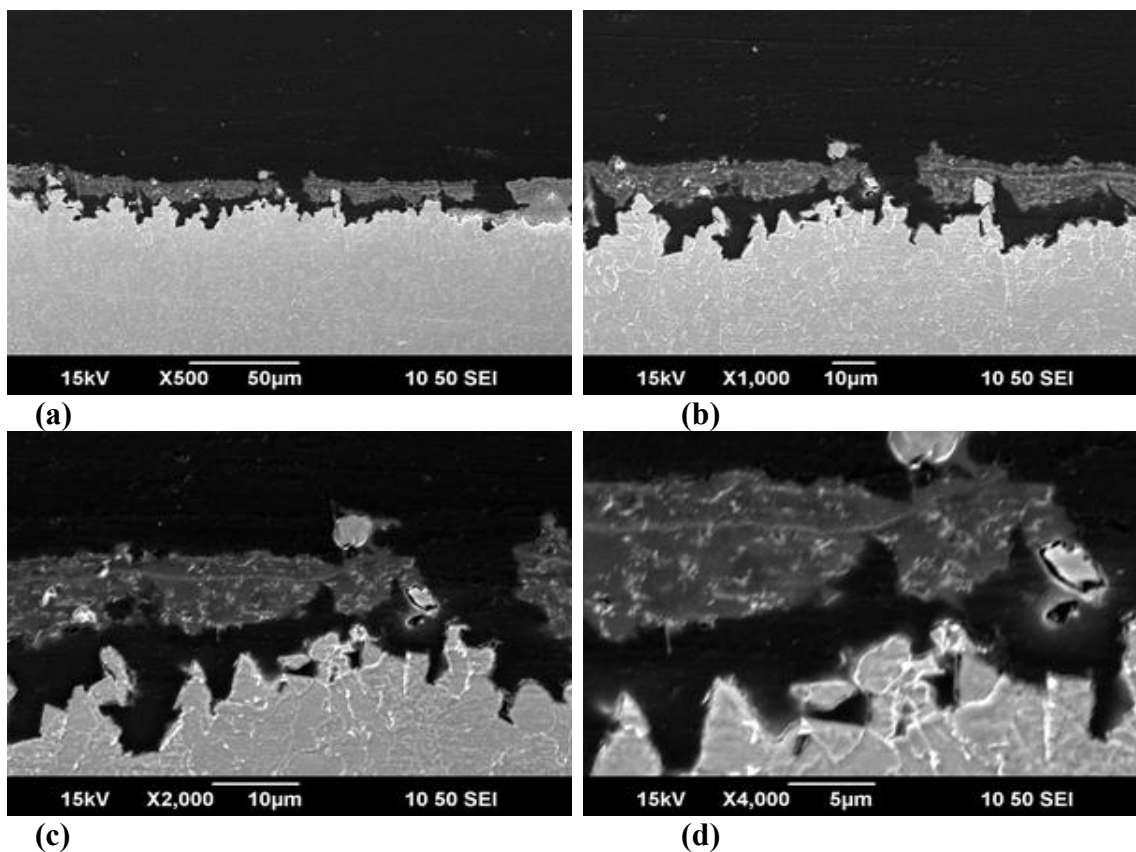
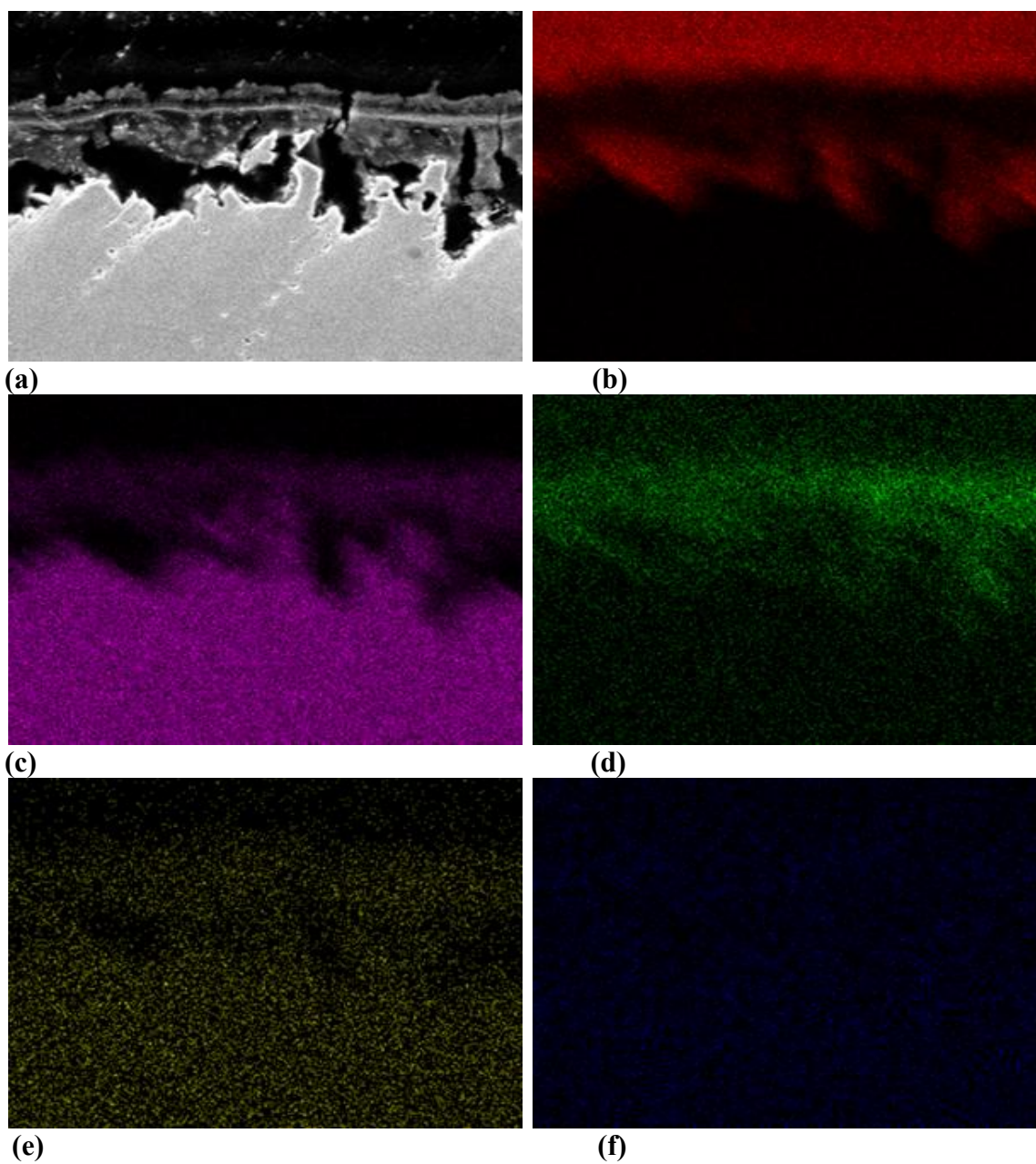


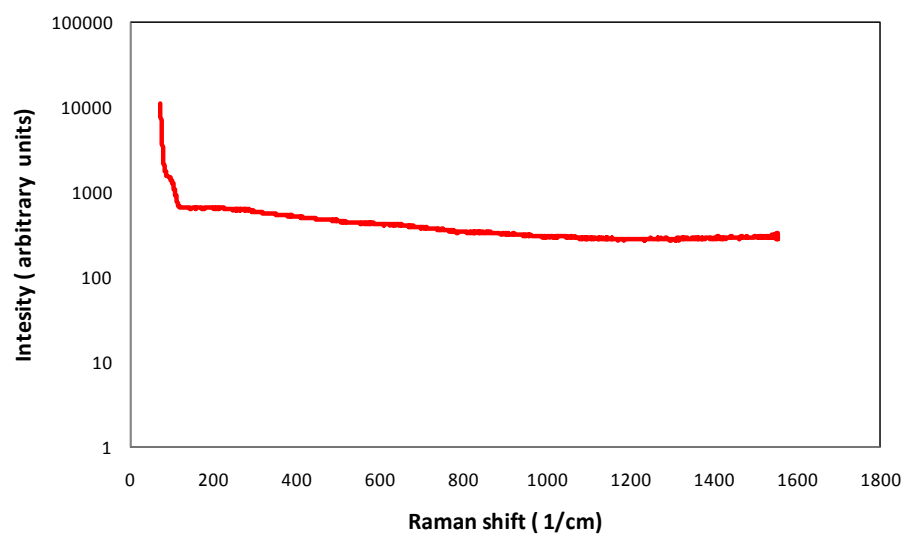
Figure 53. Microstructure of X65 (0.05 wt.% C) recovered from bulk solution at pH 5.0 and 60°C for 3 days of exposure (a) SEM image of cross-section at 500 x magnifications, (b) SEM image at 1000x magnification, (c) SEM image at 2000x magnification, and (d) SEM image at 4000x magnification.



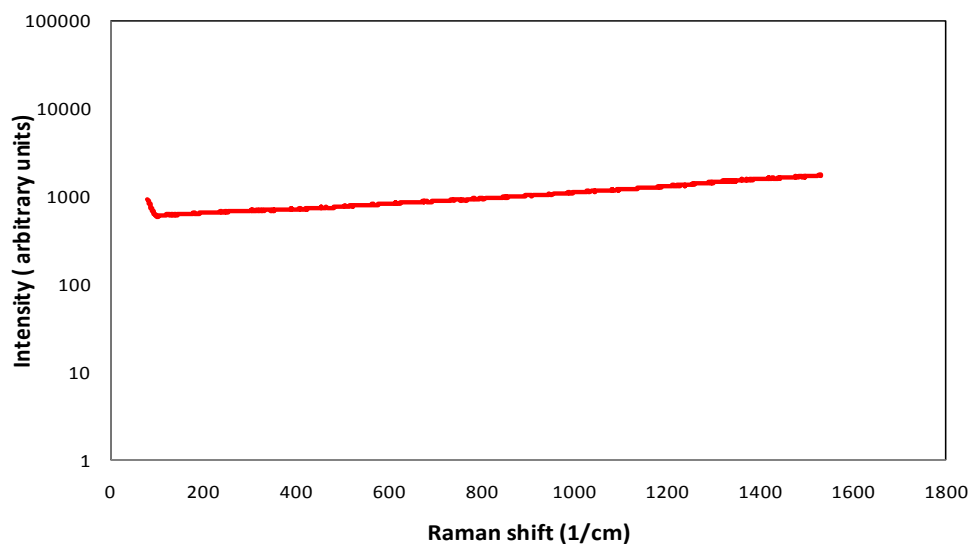
(a) **(b)**
(c) **(d)**
(e) **(f)**
Figure 54. Elemental mapping of X65 (0.05 wt.% C) sample surface after recovery from bulk solution of pH 5.0 at 60°C for the cross-section after 3 days exposure at 2000x magnification (a) SEM image of cross-section, (b) carbon distribution map (c) iron map (d) oxygen map (e) manganese map, and (f) molybdenum map.

Table 14
Thickness of Iron Carbide for X65 (0.05 wt.% C) Steel

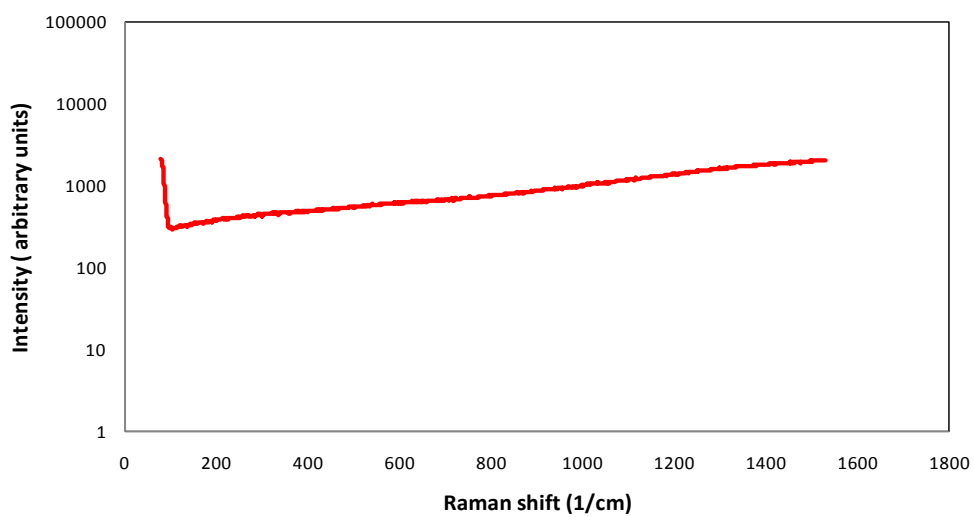
Test No.	Time	Thickness of Fe ₃ C (μm)	Depth CR (mm/yr)	Integrated LPR CR (mm/yr)	WL (mm/yr)
pH=5.0, T=60 °C					
1	1 day	5.6 +1.1/-1.2	2.0 +0.38/-0.45	7.3 \pm 0.05	5.8 \pm 0.2
2	2 days	14.4 +3.8/-3.7	2.6+1.39/-1.37	8.8 \pm 0.2	6.5 \pm 0.2
3	3 days	23.2 +2.5/-3.5	2.8 +0.9/-1.3	9.5 \pm 0.5	6.6 \pm 0.2



(a)



(b)



(c)

Figure 55. Raman analysis of sample [X65 (0.05 wt.% C)] from bulk solution at pH 5.0 at 60°C (a) Raman analysis for the surface after 1 day exposure, (b) Raman analysis for the surface after two day exposure, (c) Raman analysis for the surface after 3 day exposure.

- X65 (0.05 wt. % C) spheroidized steel:

SEM images of top surface areas and cross-sections, respectively, for the pH 5.0 tests at 60°C on X65 (0.05 wt. % C) spheroidized materials are shown in Figure 56. The surface morphology shows uniform corrosion and no scattered crystals of the iron carbonate on the surface. The thickness of the iron carbide increased with time. Figure 56 (d), Figure 56 (e), and Figure 56 (f) show that the iron carbide is present on the surface. This results in higher corrosion rates with time, as shown in Figure 35. Table 15 presents the depth of the iron carbide layer and calculated corrosion rates based on the depth of the iron carbide layer for the pH 5.0 tests at 60°C for the exposed samples after 1 day, 2 days, and 3 days. The integrated LPR and WL corrosion rates for the pH 5.0 tests at 60°C for the exposed sample after days 1, 2, and 3 are displayed in Table 15. The integrated LPR corrosion rate does not match with the depth of the iron carbide and weight loss corrosion rate. In addition, the depth of the iron carbide also does not match with the weight loss corrosion rate. Once again, weight loss measurement is the best measurement used to be sure about the corrosion rate.

Expected depths of iron carbide layers were back calculated based upon weight loss data for the corroded X65 (0.05 wt. % C) spheroidized samples as shown in Figure 57. Figure 58 shows that when a ferrite with a trace percentage of large spherical cementite particles in the steel microstructure, X65 (0.05 wt. % C) spheroidized steel, is corroded, a small population of large spherical cementite particles remains on the surface. The reason that such steel has the trace amount of large spherical cementite particles is attributed to the low carbon content, 0.05wt. % C, in this the steel as compared to the

C1018 spheroidized steel, 0.18 wt. % C. However, this layer is discontinuous on the steel surface. In the case of each type of steel, the corrosion rate increases, but there is a higher corrosion rate for X65 (0.14 wt. % C). In addition, experiments show that iron carbide layer development is dependent upon the microstructure and chemical composition, particularly carbon content, of the carbon steel from which it is derived. Figure 59 shows that the primarily iron carbide layer developed from X65 (0.05 wt. % C) spheroidized steel has carbon, iron, oxygen, manganese, and molybdenum.

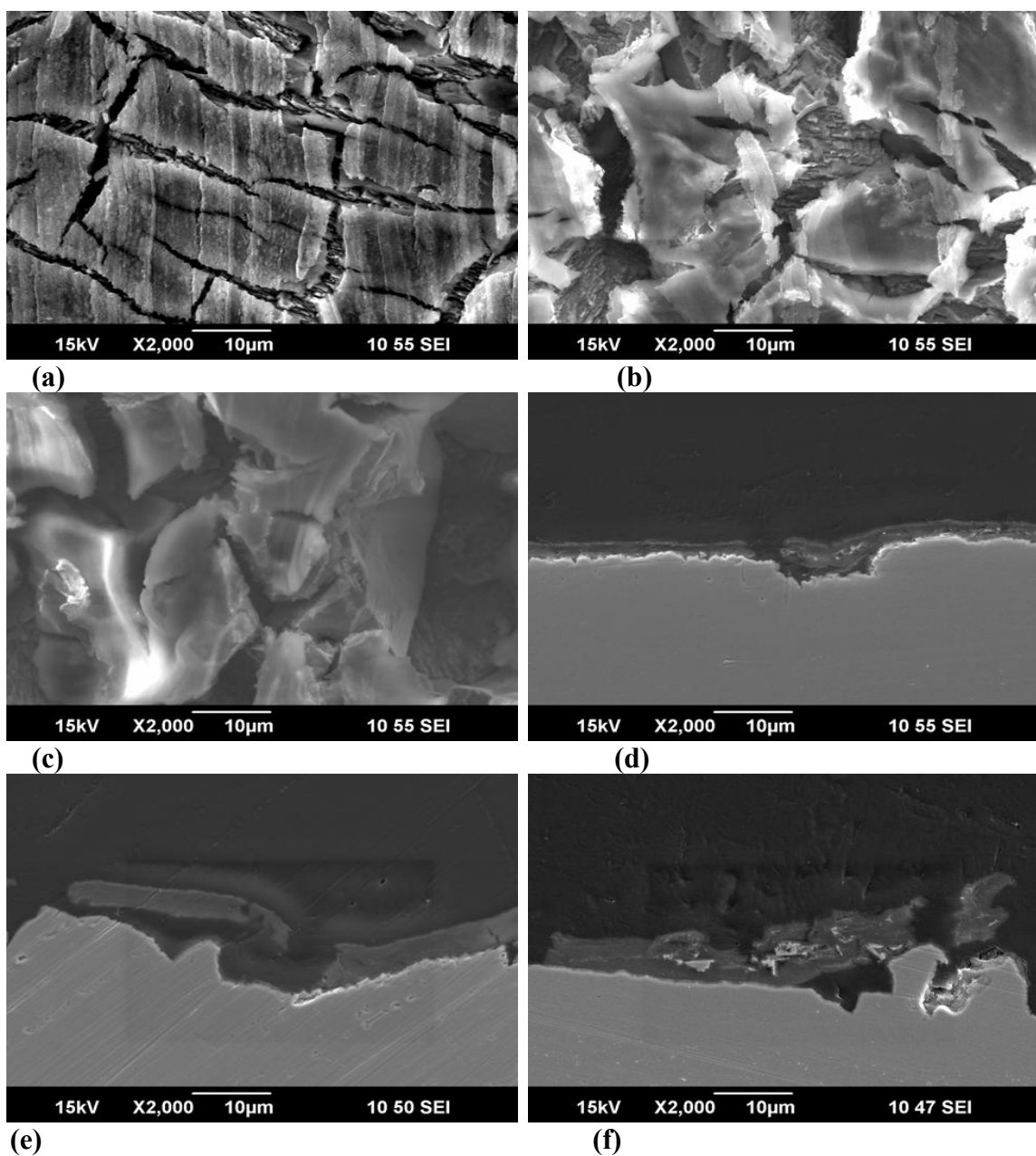
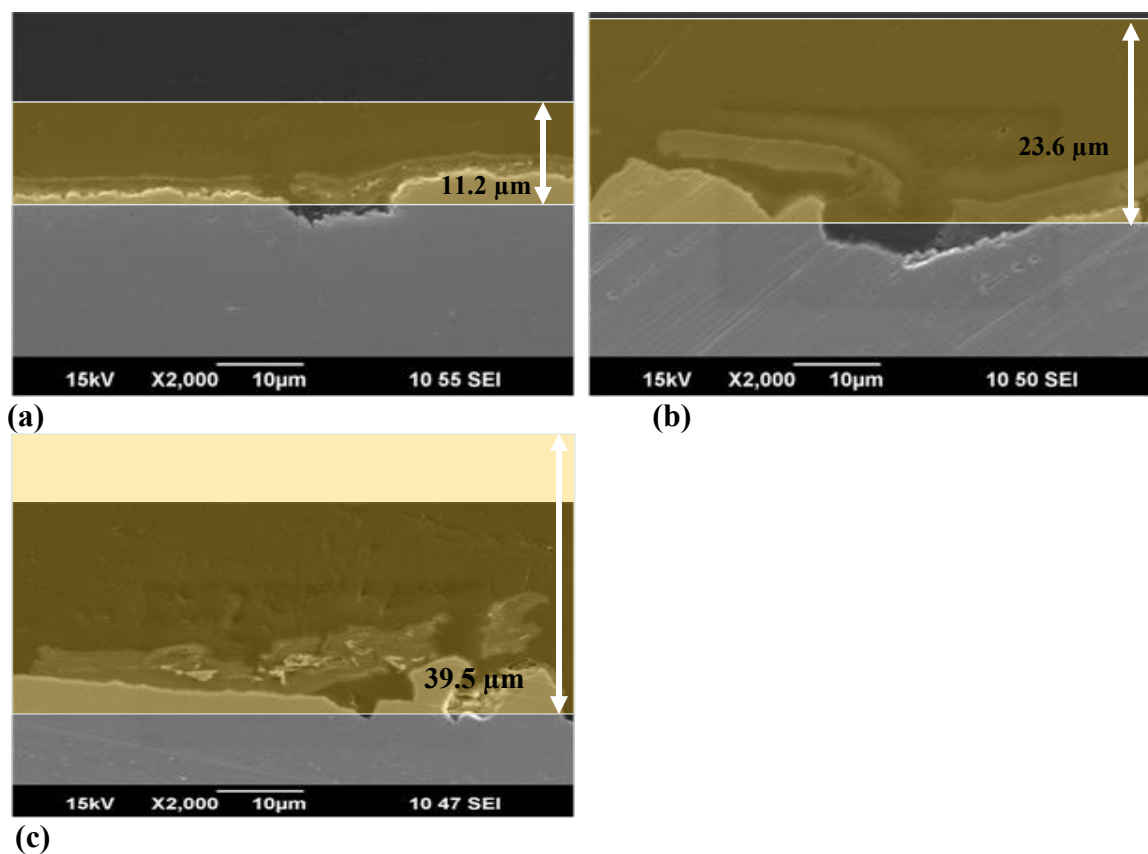


Figure 56. Sample [X65 (0.05 wt.% C)] spheroidized from bulk solution at pH 5.0 at 60°C (a) SEM image for the surface after 1 day exposure, (b) SEM image for the surface after two day exposure, (c) SEM image for the surface after 3 day exposure, (d) SEM image for the cross-section after 1 day exposure, (e) SEM image for the cross-section after two day exposure, and (f) SEM image for the cross-section after 3 day exposure.



(c)
Figure 57. Expected Fe₃C layer depth on X65 (0.05 wt.% C) spheroidized from bulk solution pH 5.0 at 60°C (a) SEM image for the cross-section after 1 day exposure, (b) SEM image for the cross-section after 2 day exposure, and (c) SEM image for the cross-section after 3 day exposure.

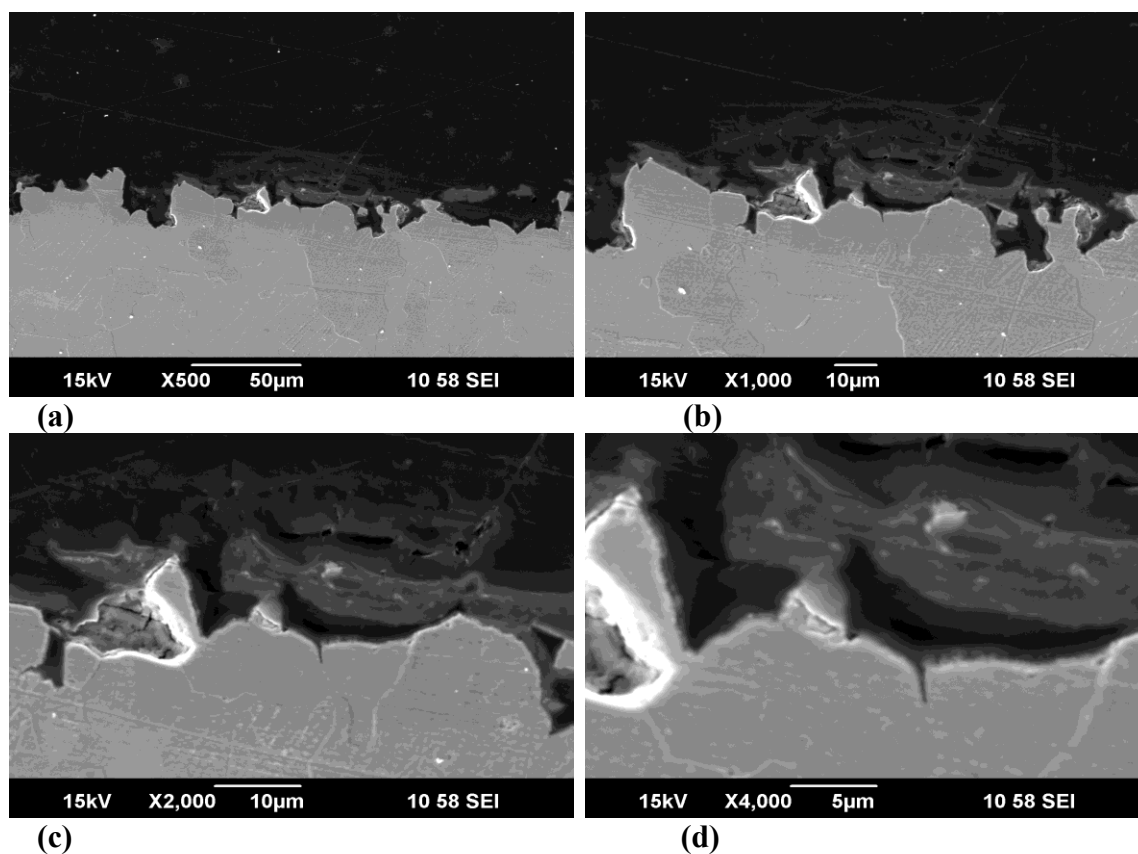
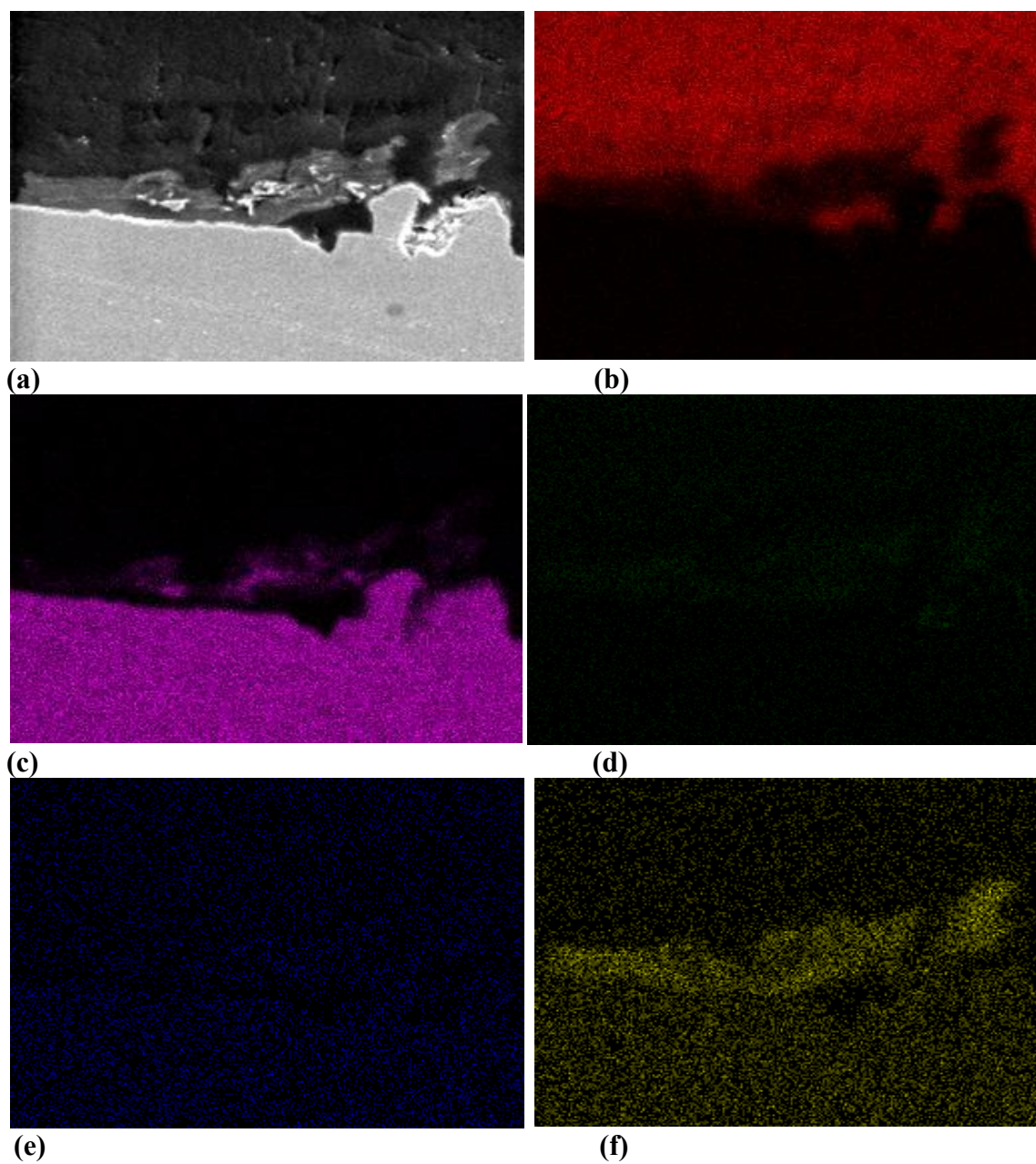


Figure 58. Microstructure of X65 (0.05 wt.% C) spheroidized recovered from bulk solution at pH 5.0 and 60°C for 3 days of exposure (a) SEM image of cross-section at 500 x magnifications, (b) SEM image at 1000x magnification, (c) SEM image at 2000x magnification, and (d) SEM image at 4000x magnification.



(a) **(b)**
(c) **(d)**
(e) **(f)**
Figure 59. Elemental mapping of X65 (0.05 wt.% C) spheroidized sample surface after recovery from bulk solution of pH 5.0 at 60°C for the cross-section after 3 days exposure at 2000x magnification (a) SEM image of cross-section, (b) carbon distribution map (c) iron map (d) oxygen map (e) manganese map, and (f) molybdenum map.

Table 15
Thickness of Iron Carbide for X65 (0.05 wt.% C) Spheroidized Steel

Test No.	Time	Thickness of Fe ₃ C	Depth CR	Integrated LPR CR	WL
		(μm)	(mm/yr)	(mm/yr)	(mm/yr)
pH=5.0, T=60 °C					
1	1 day	3.5 +0.9/-1.4	1.3 +0.3/-0.5	7.2 \pm 0.1	4.1 \pm 0.1
2	2 days	8.6 +4.2/-4.4	1.6 +0.8/-0.8	7.7 \pm 0.1	4.3 \pm 0.1
3	3 days	13.0 +2.5/-3.5	1.7 +0.3/-0.4	8.2 \pm 0.1	4.8 \pm 0.2

5.3.2.1 Summary for Fe₃C Characteristics & Corrosion

The corrosion rate increases for each type of steel with time, but there is a higher corrosion rate for C1018 quenched-tempered steel. In addition, experiments show that iron carbide layer development is dependent upon the microstructure and chemical composition, particularly carbon content, of the carbon steel from which it is derived as shown in Table 16.

The integrated LPR corrosion rate does not match the depth of the iron carbide and weight loss corrosion rate for days 1, 2, and 3 at the pH 5.0 tests at 60°C on each type of steel. However, the depth of iron carbide matches the weight loss corrosion on C1018 ferrite-pearlite and C1018 quenched-tempered steels due to present of more coherent iron carbide layer structures. The best match is observed for day 3 at the pH 5.0 tests at 60°C, on C1018 ferrite-pearlite and c1018 quenched-tempered steels. The depth of iron carbide does not match the weight loss corrosion on C1018 spheroidized, X65 (0.14 wt. % C),

X65 (0.05 wt. % C), and X65 (0.05 wt. % C) spheroidized steel because of no present of coherent iron carbide layer structures

Table 16
Summary for Fe_3C Characteristics of Corroded X65 and C1018 Steels

No.	Test Materials	Microstructure of steel	Microstructure of Fe_3C
pH=5.0, T=60 °C			
1	C1018 (F-P)	ferritic-pearlitic	a layer of cementite lamellae containing cavities remains on the steel surface
2	C1018 (Sph.)	ferrite with large spherical cementite particles	a layer of large spherical cementite particles remains on the surface, but is discontinuous
3	C1018 (Q-T)	quenched-tempered martensitic	a layer of cementite with a lot of cavities remains on the steel surface
4	X65 (0.14 wt.% C) (Q-T)	ferrite with discrete cementite particles	a layer of discrete cementite particles remains on the surface
5	X65 (0.05 wt.% C) (Q-T)	ferrite with discrete cementite particles	a layer of discrete cementite particles remains on the surface, but is discontinuous
6	X65 (0.05 wt.% C) Sph.	ferrite with a trace percentage of large spherical cementite particles	a layer of this a trace percentage of large spherical cementite particles on the surface; but is also discontinuous

5.3.3 Investigating The Effect of Residual Fe₃C on Inhibitor Performance:

The goal of this part of the study is to observe the difference between X65 and C1018 steels with respect to iron carbide development and the variation in inhibitor performance on pre-corroded specimens. This was the main objective of this research.

The inhibitor used in this study is an imidazoline-type inhibitor. Its molecular structure consists of three components, a heterocyclic head group, long hydrocarbon tail, and pendant side chain, as shown in Figure 60 [42].

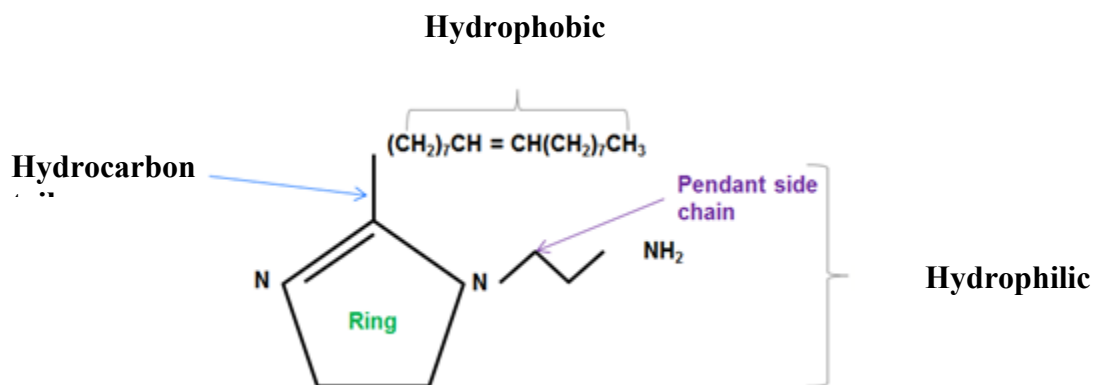


Figure 60. Characteristic structure of an imidazoline-type inhibitor [40].

In addition, the hydrophobic part is not soluble in water; however, the hydrophilic head is soluble, as illustrated in Figure 60.

Methodology

- ❖ Test 1:
 - ❖ 1 day pre-corrosion to develop Fe₃C
 - ❖ Add inhibitor and monitor for 2 more days

- ❖ Test 2:
 - ❖ Inhibited samples without pre-corrosion.
 - ❖ Comparison of results with each other and with uninhibited tests.

Effect of residual Fe_3C on inhibitor performance:

- C1018 ferrite-pearlite steel:

Figure 61 shows that corrosion rates obtained without pre-corrosion in the presence of twice the critical micelle concentration ($2 \times \text{CMC}$, 72 ppm) of imidazoline-type inhibitor on C1018 ferrite-pearlite steel decreases from 0.5 ± 0.09 mm/yr to 0.02 ± 0.01 mm/yr. Also, Figure 61 shows that corrosion rate obtained with 1 day pre-corrosion in the presence of 72 ppm of imidazoline-type inhibitor decreases from 5.9 ± 0.8 mm/yr to 0.3 ± 0.01 mm/yr after 2 days of inhibition. This indicates that the performance of inhibitor was impaired after 1 day of pre-corrosion due to the presence of iron carbide lamellae derived from pearlite.

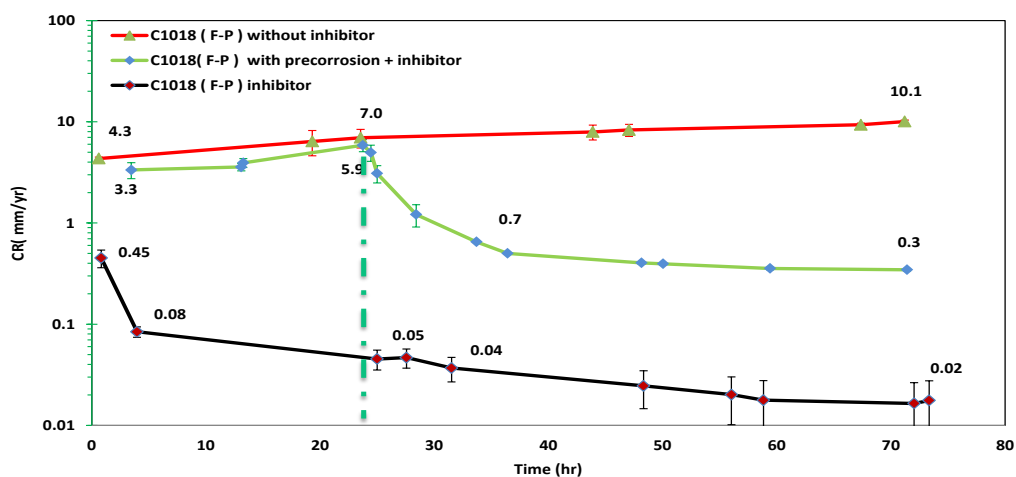


Figure 61. Corrosion rate vs. time for experiments conducted with C1018 ferrite-pearlite steel at pH 5.0 and 60°C for injection 72 ppm of imidazoline-type inhibitor

- C1018 spheroidized steel:

Figure 62 shows that corrosion rates obtained without pre-corrosion in the presence of twice the critical micelle concentration ($2 \times \text{CMC}$, 72 ppm) of imidazoline-type inhibitor on C1018 spheroidized steel decreases from 1.4 ± 0.05 mm/yr to 0.03 ± 0.01 mm/yr. Also, Figure 62 shows that corrosion rates obtained with 1 day pre-corrosion in the presence of 72 ppm of imidazoline-type inhibitor decrease from 8.5 ± 0.8 mm/yr to 0.11 ± 0.01 mm/yr after 2 days of inhibition. This also indicates that the performance of inhibitor was impaired after 1 day of pre-corrosion due to the presence of iron carbide. However, the performance of the inhibitor on C1018 spheroidized steel was less impaired than the performance of the inhibitor on C1018 ferrite-pearlite steel. Therefore, the

performance of the inhibitor after 1 day pre-corrosion is also dependent on the microstructure of the steel.

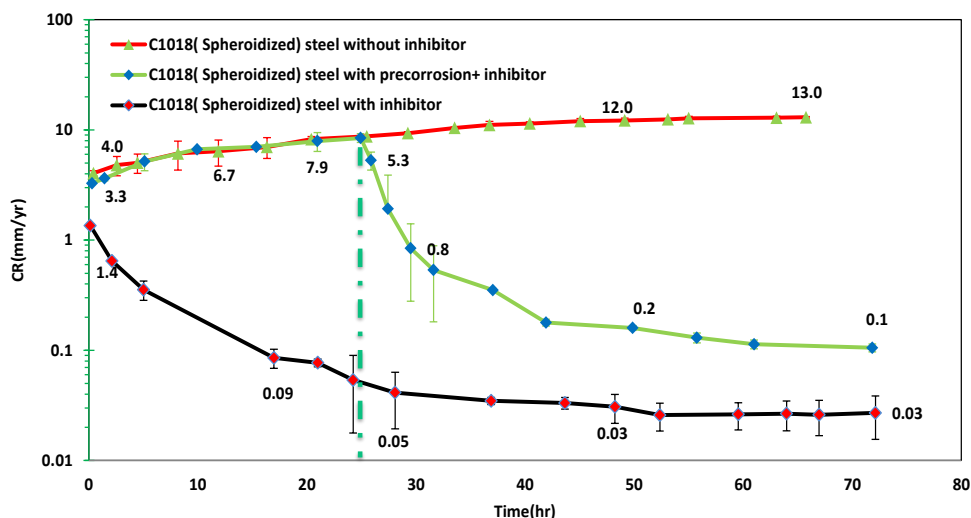


Figure 62. Corrosion rate vs. time for experiments conducted with C1018 spheroidized steel at pH 5.0 and 60°C for injection 72 ppm of imidazoline-type inhibitor.

- C1018 quenched-tempered steel:

Figure 63 shows that corrosion rates obtained without pre-corrosion in the presence of twice the critical micelle concentration ($2 \times \text{CMC}$, 72 ppm) of imidazoline-type inhibitor on C1018 quenched-tempered steel decreases from 2.6 ± 0.03 mm/yr to 0.07 ± 0.01 mm/yr. Also, Figure 63 shows that corrosion rate obtained with 1 day pre-corrosion in the presence of 72 ppm of imidazoline-type inhibitor decreases from 11.6 ± 0.1 mm/yr to 0.18 ± 0.01 mm/yr after 2 days of inhibition. This also indicates that the performance of inhibitor was impaired after 1 day of pre-corrosion due to the presence of

iron carbide. However, the performance of the inhibitor on C1018 quenched-tempered steel was more impaired than the performance of the inhibitor on C1018 spheroidized steel, but not more impaired than the performance of the inhibitor on C1018 ferrite-pearlite steel. Therefore, the performance of the inhibitor after 1 day pre-corrosion is also dependent on the microstructure of the steel.

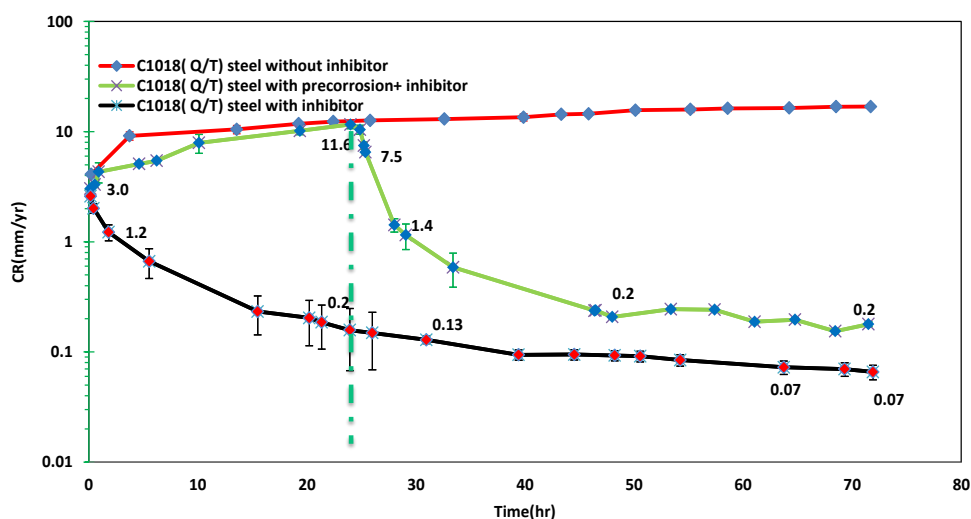


Figure 63. Corrosion rate vs. time for experiments conducted with C1018 quenched-tempered steel at pH 5.0 and 60°C for injection 72 ppm of imidazoline-type inhibitor.

- X65 (0.14 wt. % C) steel:

Figure 64 shows that corrosion rate obtained without pre-corrosion in the presence of 2 CMC (72 ppm) of imidazoline-type inhibitor on X65 (0.14 wt.% C) decreases from 0.9 ± 0.2 mm/yr to 0.02 ± 0.01 mm/yr. Also, Figure 64 shows that corrosion rate obtained after 1 day pre-corrosion in the presence of 2 CMC (72 ppm) of

imidazoline type inhibitor decreases from 10.1 ± 0.9 mm/yr to 1.7 ± 0.06 mm/yr after 2 days of inhibition. This also indicates that the performance of the inhibitor was impaired after 1 day of pre-corrosion due to the presence of iron carbide.

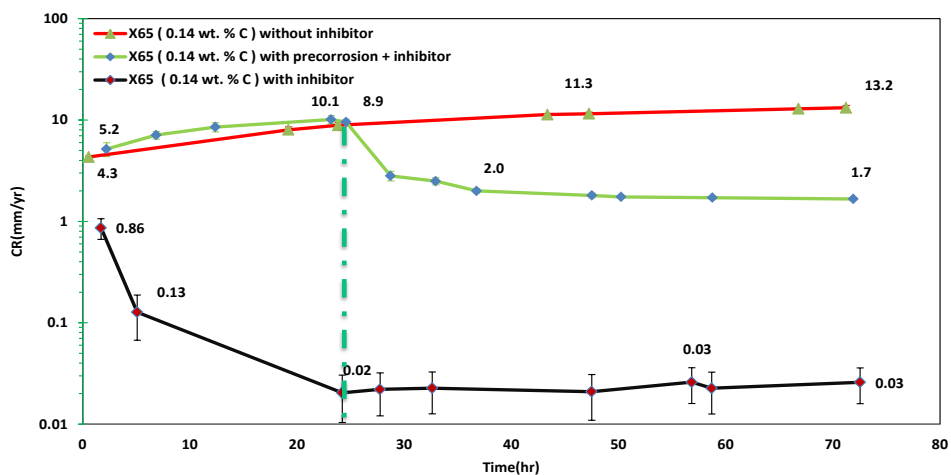


Figure 64. Corrosion rate vs. time for experiments conducted with X65 (0.14 wt.% C) steel at pH 5.0 and 60°C for injection 72 ppm of imidazoline-type inhibitor.

- X65 (0.05 wt. % C) steel:

Figure 65 shows that corrosion rate obtained without pre-corrosion in the presence of 2 CMC (72 ppm) of imidazoline-type inhibitor on X65 (0.05 wt.% C) decreases from 1.9 ± 0.1 mm/yr to 0.11 ± 0.01 mm/yr. Also, Figure 65 shows that corrosion rate obtained after 1 day pre-corrosion in the presence of 2 CMC (72 ppm) of imidazoline type inhibitor decreases from 8.5 ± 0.9 mm/yr to 0.57 ± 0.02 mm/yr after 2

days of inhibition. This also indicates that the performance of the inhibitor was impaired after 1 day of pre-corrosion due to the presence of iron carbide. However, the performance of the inhibitor on X65 (0.05 wt.% C) steel was less impaired than the performance of the inhibitor on C1018 X65 (0.14 wt.% C) steel. Therefore, the performance of the inhibitor after 1 day pre-corrosion is also dependent on the microstructure of the steel.

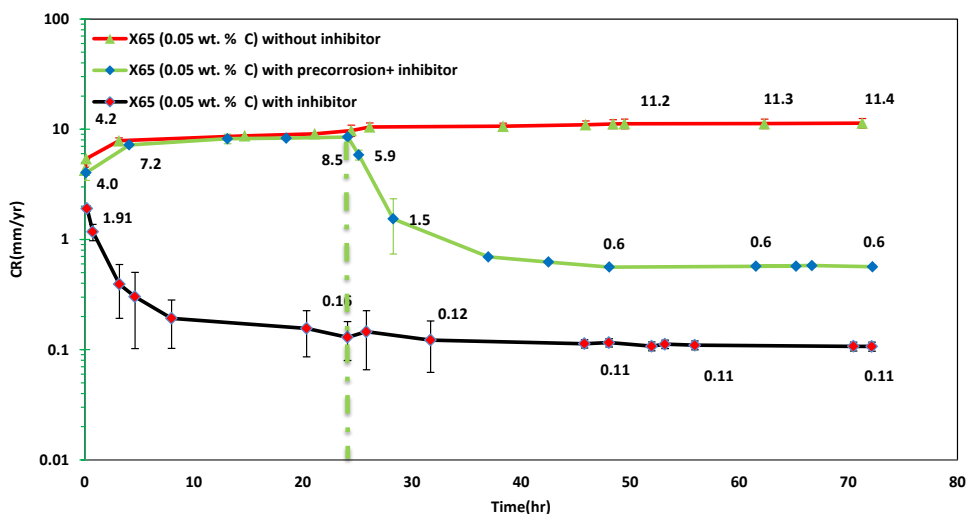


Figure 65. Corrosion rate vs. time for experiments conducted with X65 (0.05 wt.% C) steel at pH 5.0 and 60°C for injection 72 ppm of imidazoline-type inhibitor.

- X65 (0.05 wt. % C) spheroidized steel:

Figure 66 shows that corrosion rate obtained without pre-corrosion in the presence of 2 CMC (72 ppm) of imidazoline-type inhibitor on X65 (0.05 wt. % C)

spheroidized decreases from 1.6 ± 0.9 mm/yr to 0.005 ± 0.001 mm/yr. Also, Figure 66 shows that corrosion rate obtained after 1 day pre-corrosion in the presence of 2 CMC (72 ppm) of imidazoline type inhibitor decreases from 8.7 ± 0.8 mm/yr to 0.07 ± 0.005 mm/yr after 2 days of inhibition. This also indicates that the performance of the inhibitor on X65 (0.05 wt. % C) spheroidized steel was more impaired after 1 day of pre-corrosion than other type of steels due to the presence of iron carbide having a trace percentage of large spherical cementite particles in the steel microstructure. Therefore, the performance of the inhibitor after 1 day pre-corrosion is also dependent on the microstructure and chemical composition of the steel. However, it had the least effect on inhibition of all the studied steels.

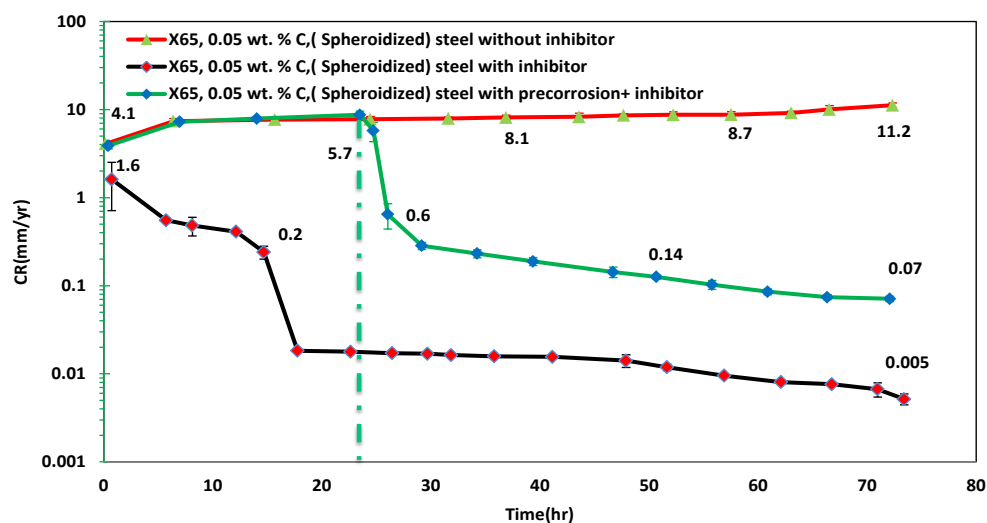


Figure 66. Corrosion rate vs. time for experiments conducted with X65 (0.05 wt.% C) spheroidized steel at pH 5.0 and 60°C for injection 72 ppm of imidazoline-type inhibitor.

Surface Analysis:

- C1018 ferrite-pearlite steel:

SEM images of top surface areas and cross-sections, respectively, for the pH 5.0 tests at 60°C on C1018 ferrite-pearlite steel with 1 day pre-corrosion in the presence of 2 CMC (72 ppm) of imidazoline type inhibitor are shown in Figure 67. The surface morphology shows no difference between the samples removed after each 24 hour interval. The surface morphology shows uniform corrosion and no scattered crystals of iron carbonate on the surface. The thickness of the iron carbide increased with time after 1 day of pre-corrosion. When the inhibitor was added, the thickness of the iron carbide still increased with time after 1 day inhibited and 2 days inhibited, but not as much compared to the samples corroded without the inhibitor for the same time interval. Figure 67 (d), Figure 67 (e), and Figure 67 (f) show that the iron carbide is present on the surface. Figure 68 shows that the depth of the iron carbide layer increased with time after 1 day pre-corrosion. The depth still increased after the inhibitor was added, but did not increase as much compared to the depth of the iron carbide layer for the experiment conducted with pre-corrosion and without inhibitor. This resulted in a higher corrosion rate with time after 1 day pre-corrosion, and then decreased after the inhibitor was added due to the action of the inhibitor, but did not decrease as much compared to the corrosion rate for the experiment conducted without pre-corrosion and with inhibitor, as shown in Figure 61. The depth of the iron carbide layer and calculated corrosion rate based on the depth of the iron carbide layer for the pH 5.0 tests at 60°C on C1018 ferrite-pearlite steel with 1 day pre-corrosion in the presence of 2 CMC (72 ppm) of imidazoline-type

inhibitor for the exposed sample after days 1, 2, and 3 are shown in Table 17. Integrated LPR corrosion rates for the pH 5.0 tests at 60°C on C1018 with 1 day pre-corrosion in the presence of 2 CMC (72 ppm) of imidazoline-type inhibitor for the exposed sample after days 1, 2, and 3 are also presented in Table 17. The integrated LPR corrosion rate does not match the corrosion rates derived from the depth of the iron carbide. In addition, iron carbide impairs the performance of the inhibitor.

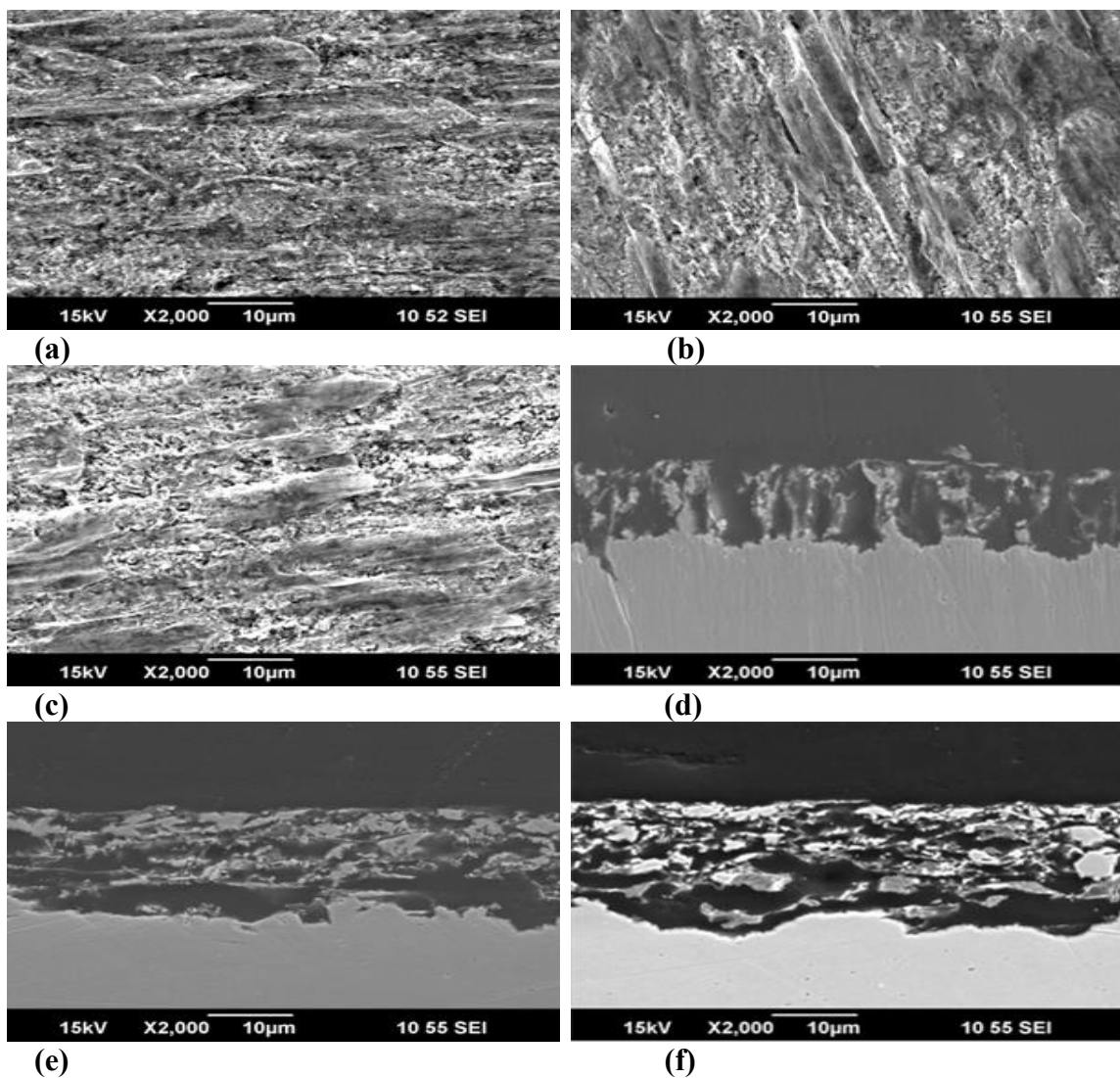


Figure 67. C1018 ferrite-pearlite steel samples recovered from bulk solution pH 5.0 at 60°C (a) SEM image for the surface after 1 day pre-corrosion, (b) SEM image for the surface after 1 day pre-corrosion and after 1 day inhibition, (c) SEM image for the surface after 1 day pre-corrosion and after 2 days inhibition, (d) SEM image for the cross-section after 1 day pre-corrosion, (e) SEM image for the cross-section after 1 day pre-corrosion and after 1 day inhibition, and (f) SEM image for the cross-section after 1 day pre-corrosion and after 2 days inhibition.

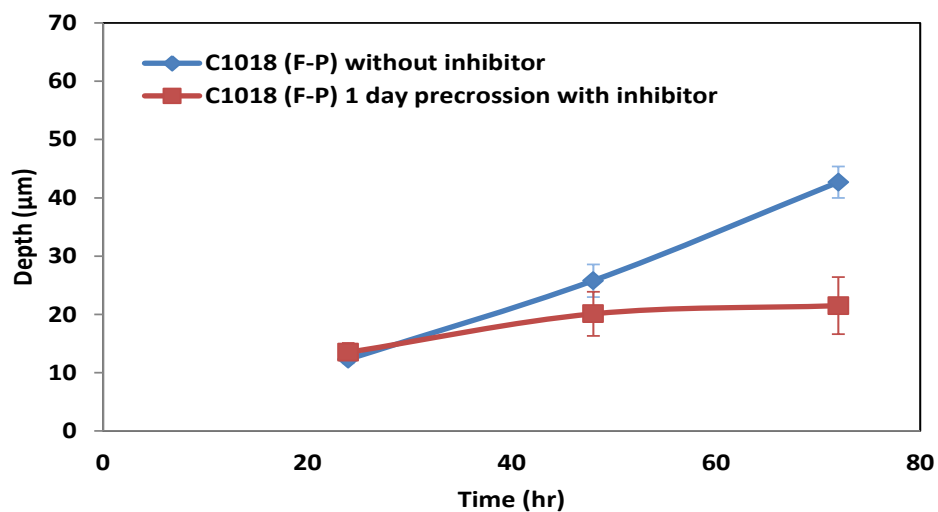


Figure 68. Depth of Fe_3C without and with imidazoline-type inhibitor vs. time for experiments conducted at pH 5.0 and 60°C with C1018 ferrite-pearlite steel.

Table 17

Thickness of Iron Carbide with Imidazoline-Type Inhibitor for C1018 Ferrite-Pearlite Steel

Test No.	Time	Thickness of Fe_3C	Depth CR	Integrated LPR CR
		(μm)	(mm/yr)	(mm/yr)
pH=5.0, T=60 °C				
1	1 day	13.5 +2.5/-1.6	4.9 +0.9/-0.6	3.7 \pm 0.3
2	2 days	6.6 +0.4/-0.2	2.4 +0.8/-0.5	1.0 \pm 0.05
3	3 days	8.0 +0.3/-0.2	1.5 +0.05/-0.03	0. \pm 0.003

- C1018 spheroidized steel:

SEM images of top surface areas and cross-sections, respectively, for the pH 5.0 tests at 60°C on C1018 spheroidized with 1 day pre-corrosion in the presence of 2 CMC (72 ppm) of imidazoline type inhibitor are shown in Figure 69. The surface morphology shows no difference between the samples removed after each 24 hour interval. The surface morphology presents uniform corrosion and no scattered crystals of iron carbonate on the surface. The thickness of the iron carbide increased with time after 1 day of pre-corrosion. When the inhibitor was added, the thickness of the iron carbide still increased with time after 1 day inhibited and 2 days inhibited, but not as much compared to the samples corroded without the inhibitor for the same time interval. Figure 69 (d), Figure 69 (e), and Figure 69 (f) show that the iron carbide is present on the surface. Figure 70 shows that the depth of the iron carbide layer increased with time after 1 day pre-corrosion. The depth still increased after the inhibitor was added, but did not increase as much compared to the depth of the iron carbide layer for the experiment conducted with pre-corrosion and without inhibitor. This resulted in a higher corrosion rate with time after 1 day pre-corrosion, and then decreased after the inhibitor was added due to the action of the inhibitor, but did not decrease as much compared to the corrosion rate for the experiment conducted without pre-corrosion and with inhibitor, as shown in Figure 62. Table 18 displays the depth of the iron carbide layer and calculated corrosion rates based on the depth of the iron carbide layer for the pH 5.0 tests at 60°C on C1018 spheroidized with 1 day pre-corrosion in the presence of 2 CMC (72 ppm) of imidazoline-type inhibitor for the exposed sample after days 1, 2, and 3. Integrated LPR

corrosion rates for the pH 5.0 tests at 60°C on C1018 with 1 day pre-corrosion in the presence of 2 CMC (72 ppm) of imidazoline-type inhibitor for the exposed sample after days 1, 2, and 3 are presented in Table 18. The integrated LPR corrosion rate does not match the corrosion rates derived from the depth of the iron carbide. In addition, iron carbide impairs the performance of the inhibitor. The Fe₃C developed from C1018 spheroidized steel has less of an effect on the performance of the inhibitors than the Fe₃C developed from C1018 ferrite-pearlite steel due to the fact that when C1018 spheroidized steel is corroded, a layer of large spherical cementite particles remained on the surface. Also, this layer is discontinuous on the steel surface that permits the inhibitor to penetrate easily through this layer. Mild steels with such structures appear to undergo more severe corrosion as compared to mild steels with ferrite-pearlite in their structures, as is the case for the C1018 ferrite-pearlite steel in the current study. Consequently, the corrosion rate for the pH 5.0 tests at 60°C on C1018 ferrite-pearlite steel with 1 day pre-corrosion in the presence of 2 CMC (72 ppm) of imidazoline type inhibitor does not decrease as much compared to the corrosion rate for the pH 5.0 tests at 60°C on C1018 spheroidized steel with 1 day pre-corrosion in the presence of 2 CMC (72 ppm) of imidazoline type inhibitor due to differences in their microstructural features that govern the nature of the residual layer.

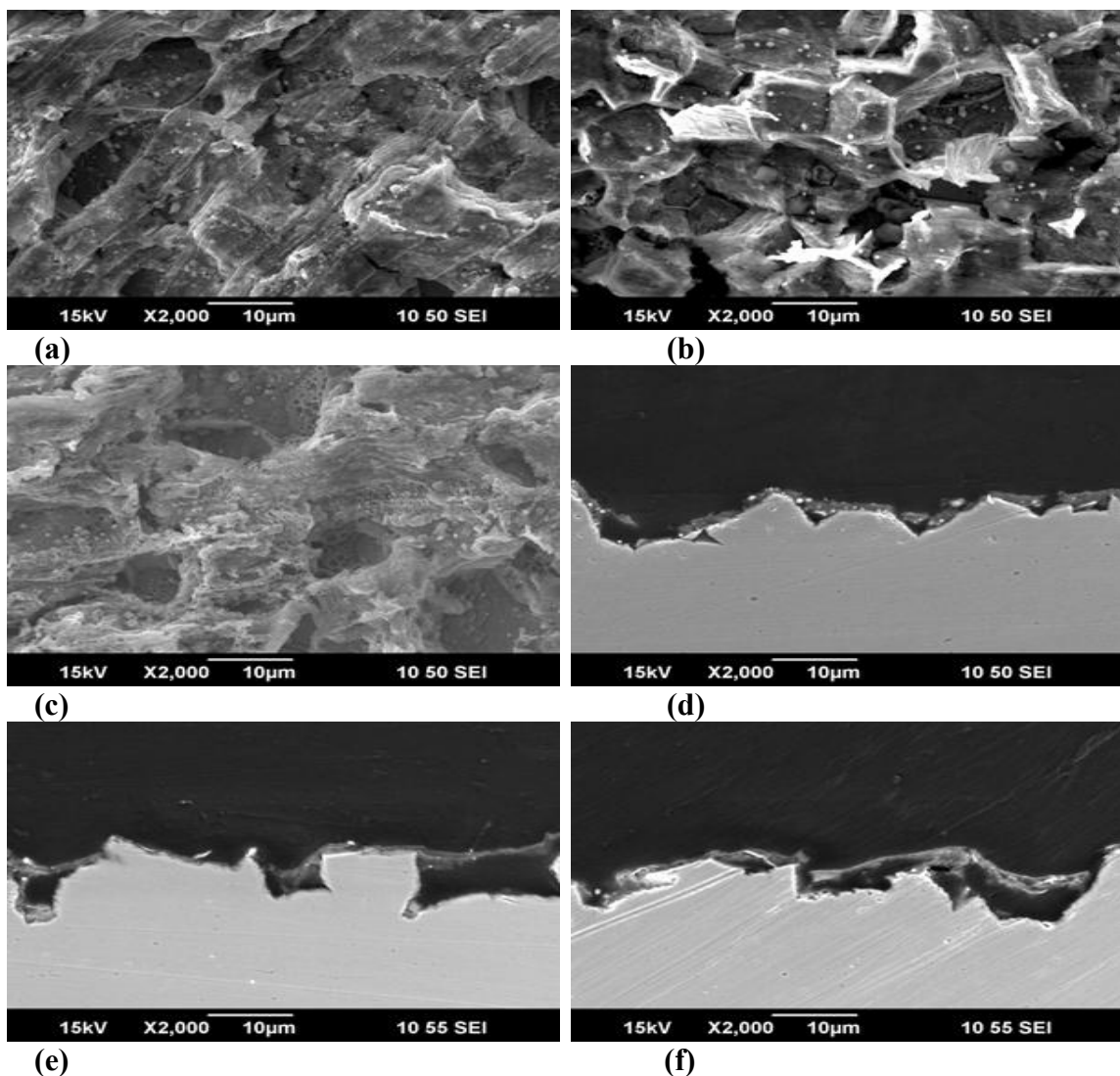


Figure 69. C1018 spheroidized samples recovered from bulk solution pH 5.0 at 60°C (a) SEM image for the surface after 1 day pre-corrosion, (b) SEM image for the surface after 1 day pre-corrosion and after 1 day inhibition, (c) SEM image for the surface after 1 day pre-corrosion and after 2 days inhibition, (d) SEM image for the cross-section after 1 day pre-corrosion, (e) SEM image for the cross-section after 1 day pre-corrosion and after 1 day inhibition, and (f) SEM image for the cross-section after 1 day pre-corrosion and after 2 days inhibition.

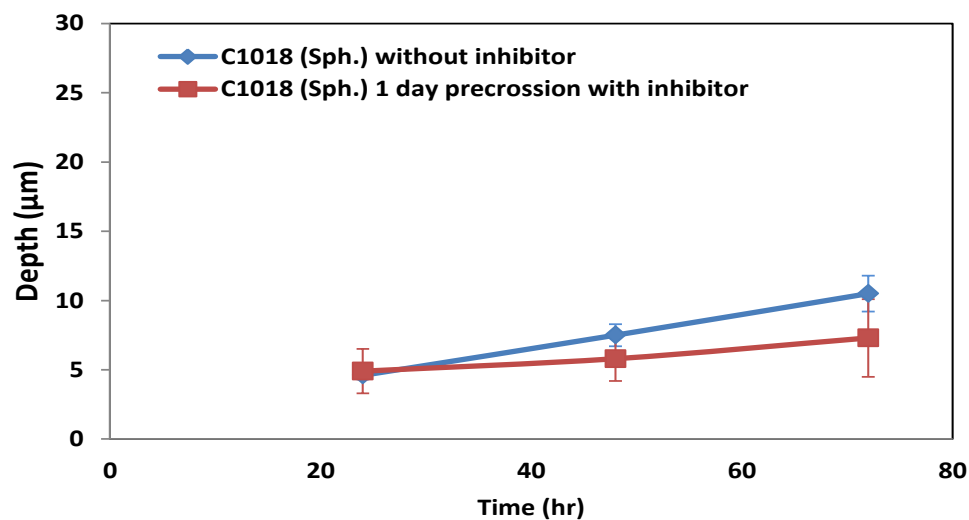


Figure 70. Depth of Fe_3C without and with imidazoline-type inhibitor vs. time for experiments conducted at pH 5.0 and 60°C with C1018 spheroidized steel.

Table 18

Thickness of Iron Carbide with Imidazoline-Type Inhibitor for C1018 Spheroidized

Test No.	Time	Thickness of Fe_3C (μm)	Depth CR (mm/yr)	Integrated LPR CR (mm/yr)
pH=5.0, T=60 °C				
1	1 day	4.6 +1.6/-1.2	1.8 +0.6/-0.4	6.4 ± 0.3
2	2 days	0.9 +0.22/-0.23	0.34 +0.08/-0.09	3.3 ± 0.4
3	3 days	2.4 +0.2/-0.1	0.4 +0.03/-0.02	0.1 ± 0.005

- C1018 quenched-tempered steel:

SEM images of top surface areas and cross-sections, respectively, for the pH 5.0 tests at 60°C on C1018 quenched-tempered steel with 1 day pre-corrosion in the presence of 2 CMC (72 ppm) of imidazoline type inhibitor are shown in Figure 71. The surface morphology shows no difference between the samples removed after each 24 hour interval. The surface morphology shows uniform corrosion and no scattered crystals of iron carbonate on the surface. The thickness of the iron carbide increased with time after 1 day of pre-corrosion. When the inhibitor was added, the thickness of the iron carbide still increased with time after 1 day inhibited and 2 days inhibited, but not as much compared to the samples corroded without the inhibitor for the same time interval. Figure 71 (d), Figure 71 (e), and Figure 71 (f) show that the iron carbide is present on the surface. Figure 72 shows that the depth of the iron carbide layer increased with time after 1 day pre-corrosion. The depth still increased after the inhibitor was added, but did not increase as much compared to the depth of the iron carbide layer for the experiment conducted with pre-corrosion and without inhibitor. This resulted in a higher corrosion rate with time after 1 day pre-corrosion, and then decreased after the inhibitor was added due to the action of the inhibitor, but did not decrease as much compared to the corrosion rate for the experiment conducted without pre-corrosion and with the inhibitor, as shown in Figure 63. The depth of the iron carbide layer and calculated corrosion rates based on the depth of the iron carbide layer for the pH 5.0 tests at 60°C on C1018 quenched-tempered steel with 1 day pre-corrosion in the presence of 2 CMC (72 ppm) of imidazoline-type inhibitor for the exposed sample after days 1, 2, and 3 are shown in

Table 19. Also, Table 19 presents integrated LPR corrosion rates for the pH 5.0 tests at 60°C on C1018 quenched-tempered steel with 1 day pre-corrosion in the presence of 2 CMC (72 ppm) of imidazoline-type inhibitor for the exposed sample after days 1, 2, and 3. The integrated LPR corrosion rate does not match the corrosion rates derived from the depth of the iron carbide. In addition, iron carbide impairs the performance of the inhibitor. The Fe₃C developed from C1018 quenched-tempered steel has less of an effect on the performance of the inhibitors than the Fe₃C developed from C1018 ferrite-pearlite and C1018 spheroidized steels due to the fact that structure of the Fe₃C developed from C1018 quenched-tempered steel contain a lot of cavities that permit inhibitor to penetrate more easily through this layer. Mild steels with such structures appear to undergo more severe corrosion as compared to mild steels with ferrite-pearlite in their structures, as is the case for the C1018 ferrite-pearlite steel in the current study. Consequently, the corrosion rate for the pH 5.0 tests at 60°C on C1018 spheroidized steel with 1 day pre-corrosion in the presence of 2 CMC (72 ppm) of imidazoline type inhibitor decreased more as compared to the corrosion rate for the pH 5.0 tests at 60°C on C1018 ferrite-pearlite and C1018 quenched-tempered steels with 1 day pre-corrosion in the presence of 2 CMC (72 ppm) of imidazoline type inhibitor due to such differences in their microstructural features.

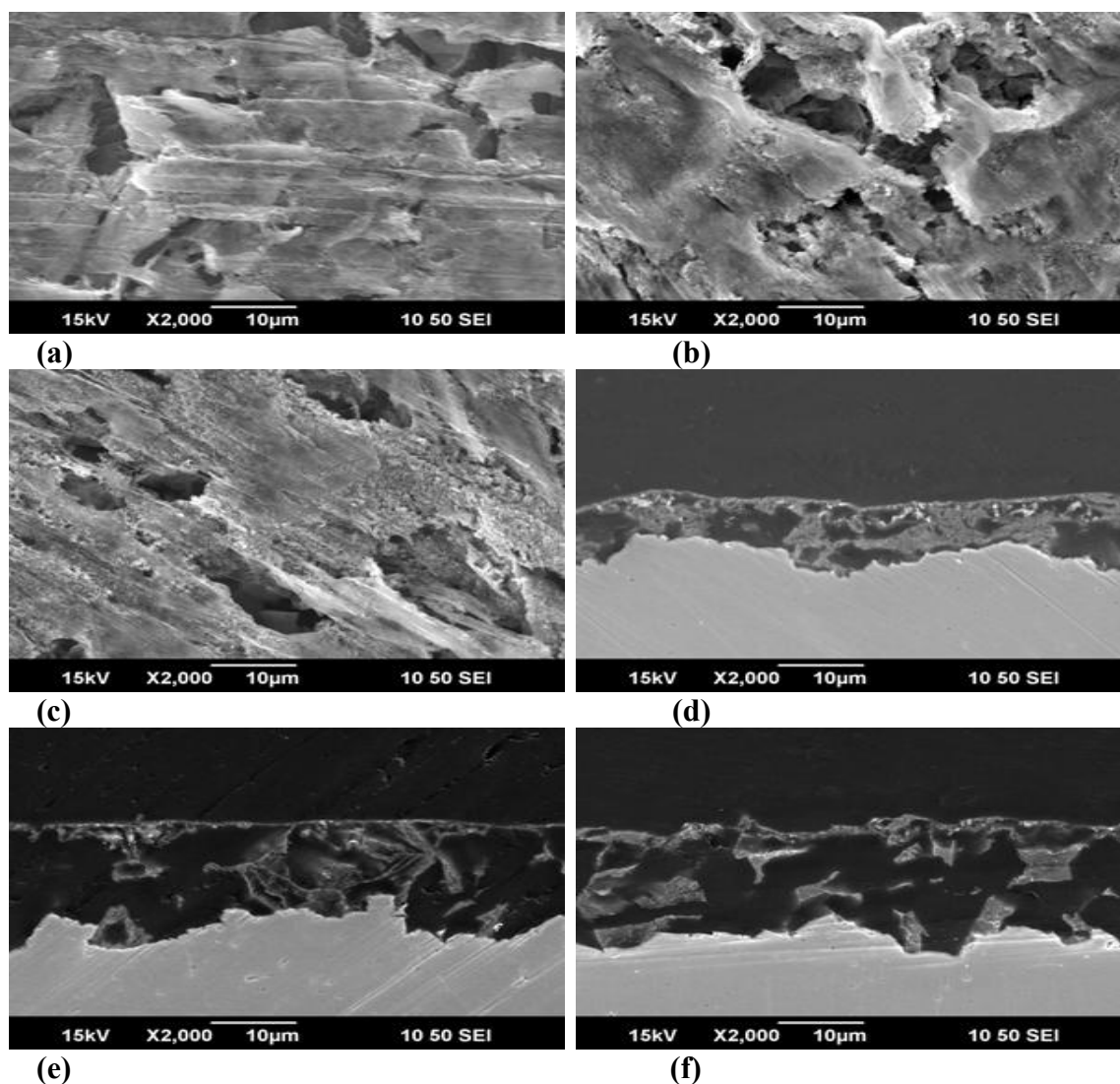


Figure 71. C1018 quenched-tempered steel samples recovered from bulk solution pH 5.0 at 60°C (a) SEM image for the surface after 1 day pre-corrosion, (b) SEM image for the surface after 1 day pre-corrosion and after 1 day inhibition, (c) SEM image for the surface after 1 day pre-corrosion and after 2 days inhibition, (d) SEM image for the cross-section after 1 day pre-corrosion, (e) SEM image for the cross-section after 1 day pre-corrosion and after 1 day inhibition, and (f) SEM image for the cross-section after 1 day pre-corrosion and after 2 days inhibition.

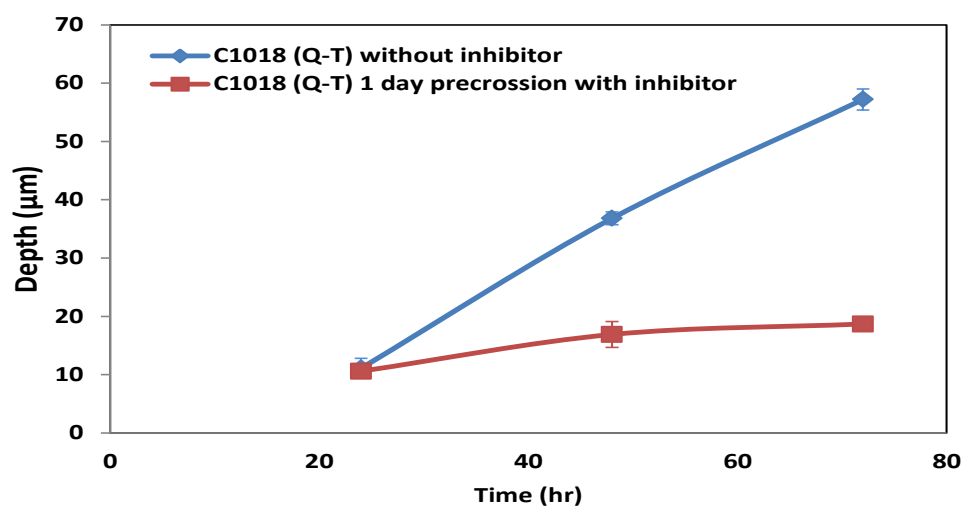


Figure 72. Depth of Fe_3C without and with imidazoline-type inhibitor vs. time for experiments conducted at pH 5.0 and 60°C with C1018 quenched-tempered steel.

Table 19

Thickness of Iron Carbide with Imidazoline-Type Inhibitor for C1018 Quenched-Tempered

Test No.	Time	Thickness of Fe_3C (μm)	Depth CR (mm/yr)	Integrated LPR CR (mm/yr)
pH=5.0, T=60 °C				
1	1 day	10.6 +1.5/-0.6	3.9 +0.5/-0.2	7.9 ± 0.5
2	2 days	6.2 +0.1/-0.2	2.3 +0.05/-0.09	3.6 ± 0.2
3	3 days	8.0 +0.10/-0.06	1.5 +0.02/-0.01	0.1 ± 0.003

- X65 (0.14 wt. % C) steel:

SEM images of top surface areas and cross-sections, respectively, for the pH 5.0 tests at 60°C on X65 (0.14 wt. % C) with 1 day pre-corrosion in the presence of 2 CMC (72 ppm) of imidazoline-type inhibitor are shown in Figure 73. The surface morphology also shows no difference between the samples removed after each 24 hour interval. The surface morphology shows uniform corrosion and no scattered crystals of iron carbonate on the surface. The thickness of the iron carbide increased with time after 1 day pre-corrosion. When the inhibitor was added, the thickness of the iron carbide also continued to increase with time after 1 day inhibited and 2 days inhibited, but not as much compared to the samples corroded without inhibitor for the same time interval. Figure 73 (d), Figure 73 (e), and Figure 73f) show that the iron carbide is present on the surface. Figure 74 shows that the depth of the iron carbide layer increased with time after 1 day of pre-corrosion. Then, it still increased after inhibitor was added, but did not increase as much compared to the depth of the iron carbide layer for the experiment conducted with pre-corrosion and without the inhibitor. This resulted in higher corrosion rates with time after 1 day pre-corrosion, and then decreased after the inhibitor was added due to the action of inhibitor, but did not decrease as much compared to the corrosion rate for the experiment conducted without pre-corrosion and with the inhibitor, as shown in Figure 64. The depth of the iron carbide layer and depth corrosion rates for the pH 5.0 tests at 60°C on X65 (0.14 wt.% C) with 1 day pre-corrosion in the presence of 2 CMC (72 ppm) of imidazoline-type inhibitor for the exposed sample after days 1, 2, and 3 are presented in Table 20. The integrated LPR corrosion rates for the pH 5.0 tests at 60°C on X65

(0.14 wt.% C) with 1 day pre-corrosion in the presence of 2 CMC (72 ppm) of imidazoline type inhibitor for the exposed sample after days 1, 2, and 3 are also shown in Table 20. The integrated LPR corrosion rate does not match the corrosion rates derived from the depth of the iron carbide. Again, iron carbide impairs the performance of the inhibitor.

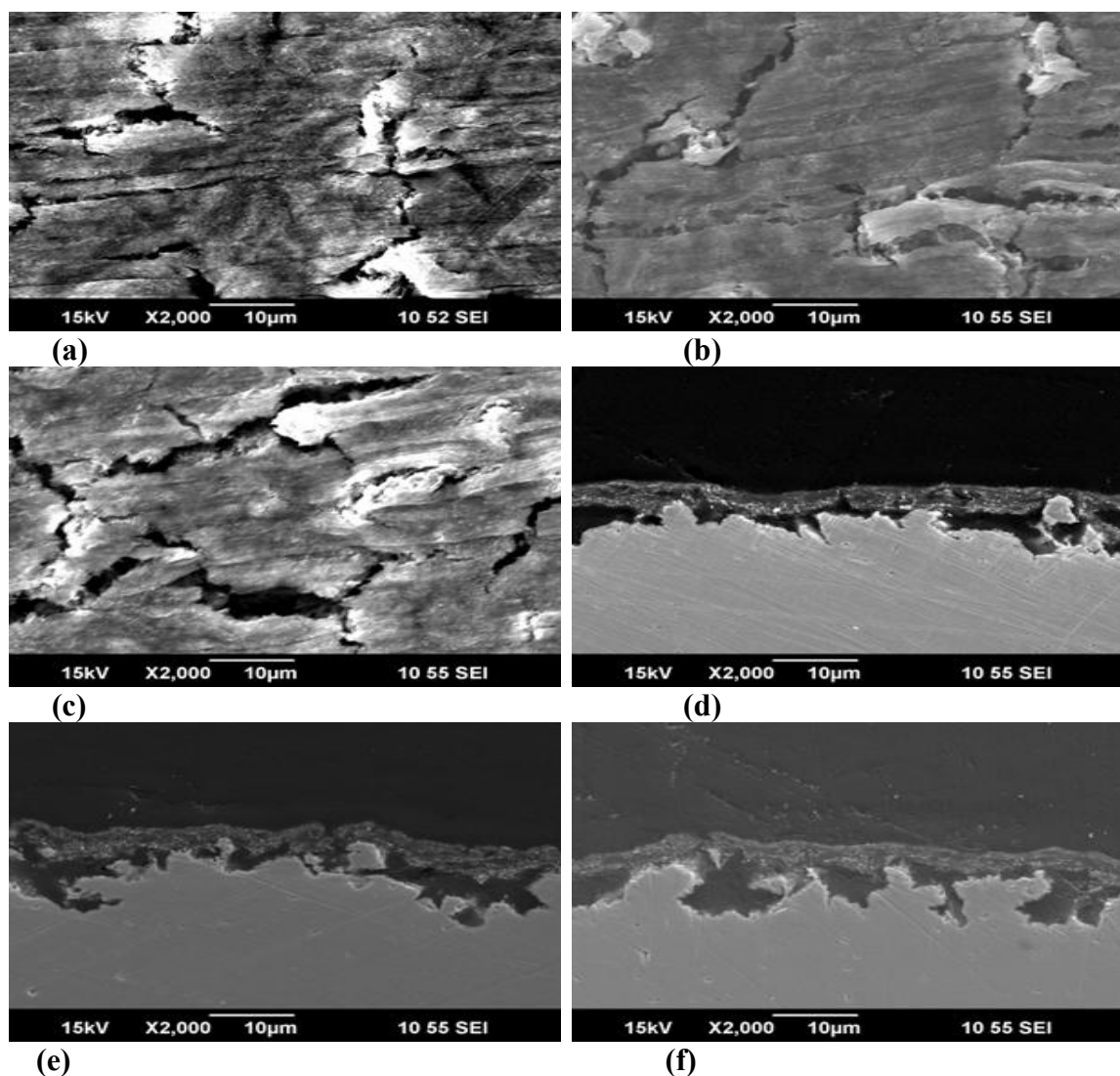


Figure 73. X65 (0.14 wt.% C) samples recovered from bulk solution at pH 5 and 60°C
 (a) SEM image for the surface after 1 day pre-corrosion, (b) SEM image for the surface after 1 day pre-corrosion and after 1 day inhibition, (c) SEM image for the surface after 1 day pre-corrosion after 2 days inhibition, (d) SEM image for the cross-section after 1 day pre-corroded, (e) SEM image for the cross-section after 1 day pre-corroded and after 1 day inhibition, and (f) SEM image for the cross-section after 1 day pre-corroded and after 2 days inhibition.

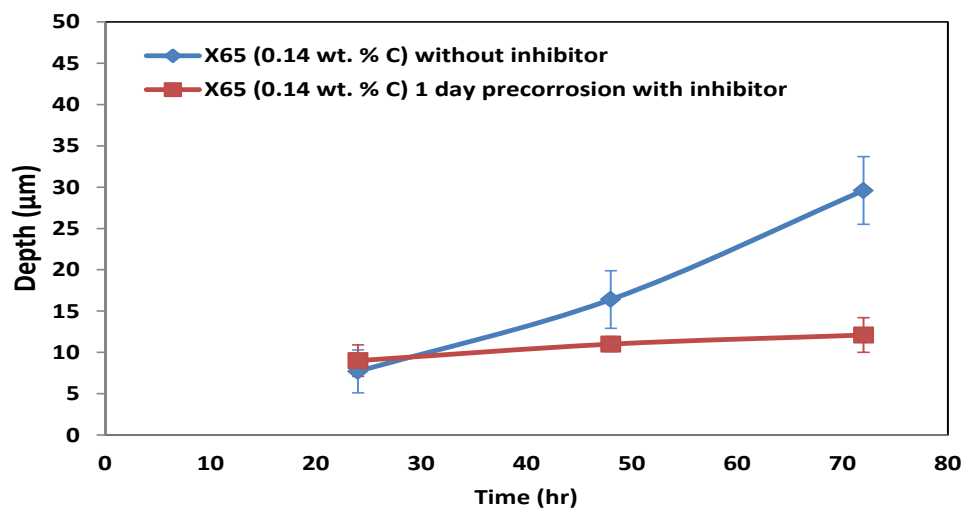


Figure 74. Depth of Fe_3C without and with imidazoline type inhibitor vs. time for experiments conducted at pH 5.0 and 60°C on X65 (0.14 wt. % C) steel.

Table 20

Thickness of Iron Carbide with Imidazoline-Type Inhibitor for X65 (0.14 wt. % C)

Test No.	Time	Thickness of Fe_3C (μm)	Depth CR (mm/yr)	Integrated LPR CR (mm/yr)
pH=5.0, T=60 °C				
1	1 day	9.0 +3.5/-2.5	3.3 +1.3/-1.0	7.8 \pm 0.4
2	2 days	2.0 +0.20/-0.23	0.7 +0.07/-0.08	3.3 \pm 0.1
3	3 days	3.1 +0.1/-0.2	0.6 +0.02/-0.03	1.3 \pm 0.05

- X65 (0.05 wt. % C) steel:

SEM images of top surface areas and cross-sections, respectively, for the pH 5.0 tests at 60°C on X65 (0.05 wt.% C) with 1 day pre-corrosion in the presence of 2 CMC (72 ppm) of imidazoline-type inhibitor are shown in Figure 75. The surface morphology also shows no difference between the samples removed after each 24 hour interval. The surface morphology shows uniform corrosion and no scattered crystals of iron carbonate on the surface. The thickness of the iron carbide increased with time after 1 day pre-corrosion. When the inhibitor was added, the thickness of the iron carbide also continued to increase with time after 1 day inhibited and 2 days inhibited, but not as much compared to the samples corroded without inhibitor for the same time interval. Figure 75 (d), Figure 75 (e), and Figure 75 (f) show that the iron carbide is present on the surface. Figure 76 shows that the depth of the iron carbide layer increased with time after 1 day of pre-corrosion. Then, it still increased after inhibitor was added, but did not increase as much compared to the depth of the iron carbide layer for the experiment conducted with pre-corrosion and without the inhibitor. This resulted in higher corrosion rates with time after 1 day pre-corrosion, and then decreased after the inhibitor was added due to the action of inhibitors, but did not decrease as much compared to the corrosion rate for the experiment conducted without pre-corrosion and with the inhibitor, as shown in Figure 65. Table 21 shows the depth of the iron carbide layer and depth corrosion rate for the pH 5.0 tests at 60°C on X65 (0.05 wt. % C) with 1 day pre-corrosion in the presence of 2 CMC (72 ppm) of imidazoline-type inhibitor for the exposed sample after days 1, 2, and 3. The integrated LPR corrosion rates for the pH 5.0 tests at 60°C on X65 (0.05 wt.% C)

with 1 day pre-corrosion in the presence of 2 CMC (72 ppm) of imidazoline type inhibitor for the exposed sample after days 1, 2, and 3 are presented in Table 21. The integrated LPR corrosion rate does not match the corrosion rates derived from the depth of the iron carbide. Again, iron carbide impairs the performance of the inhibitor. The Fe_3C developed from X65 (0.14 wt.% C) steel has more of an effect on the performance of the inhibitors than the Fe_3C developed from X65 (0.05 wt.% C) steel due to the fact that the layer of the iron carbide developed from X65 (0.14 wt.% C) seems to remain a homogenous layer on the steel surface; however, the layer of the iron carbide developed from X65 (0.05 wt.% C) is discontinuous on the corroded surface and permits the inhibitor to penetrate easily through this layer. Mild steels with such an amount of carbon appear to undergo less severe corrosion as compared to mild steels with a greater amount of carbon in their chemical composition, as is the case for the X65 (0.14 wt.% C) steel in the current study, due to the fact that iron carbide seems to remain a homogenous layer on the steel surface. Consequently, the corrosion rate for the pH 5.0 tests at 60°C on X65 (0.14 wt.% C) with 1 day pre-corrosion in the presence of 2 CMC (72 ppm) of imidazoline type inhibitor does not decrease as much compared to the corrosion rate for the pH 5.0 tests at 60°C on X65 (0.05 wt.% C) steel with 1 day pre-corrosion in the presence of 2 CMC (72 ppm) of imidazoline type inhibitor due to such differences in their microstructural features.

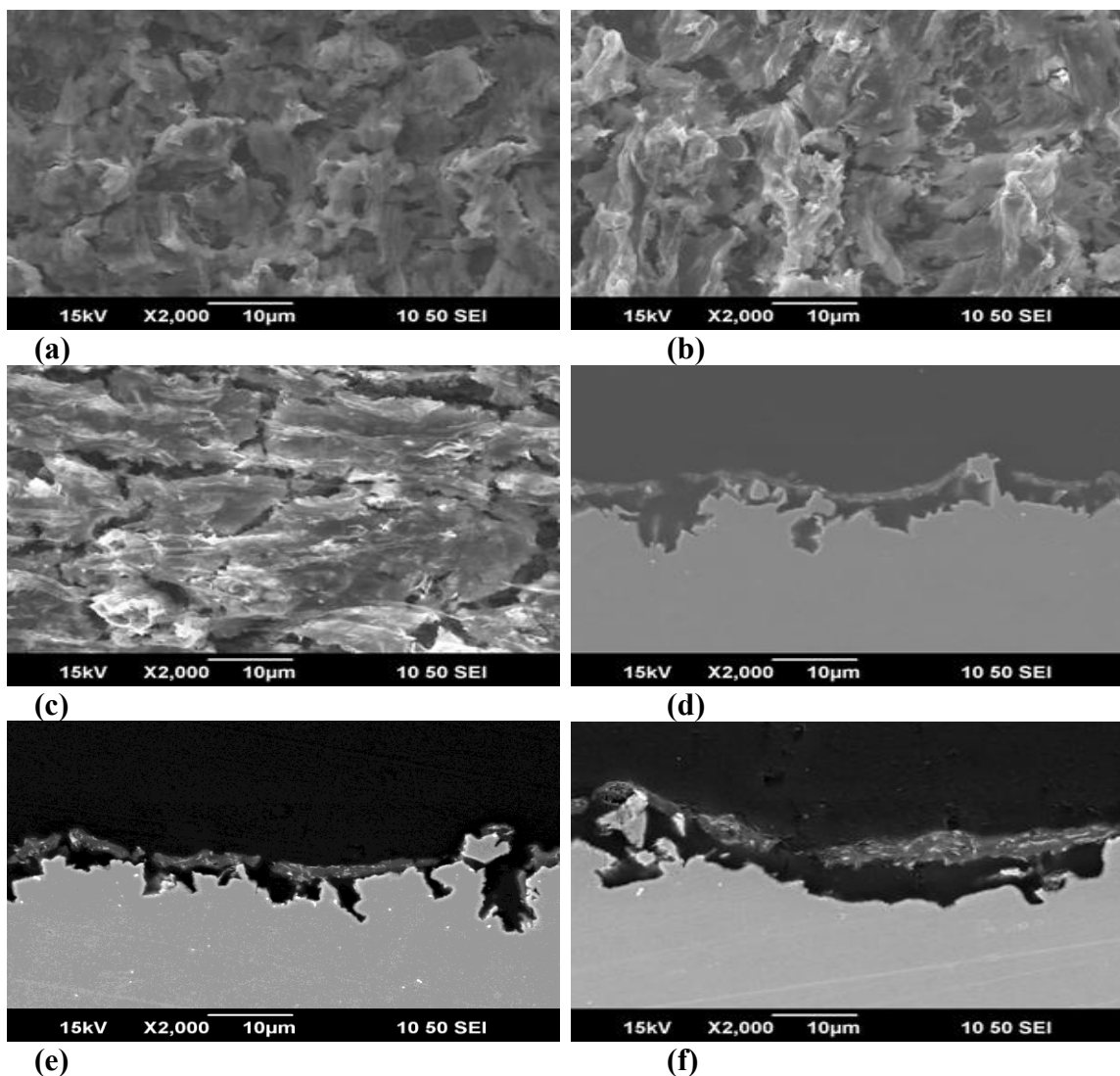


Figure 75. X65 (0.05 wt.% C) samples recovered from bulk solution at pH 5 and 60°C
 (a) SEM image for the surface after 1 day pre-corrosion, (b) SEM image for the surface after 1 day pre-corrosion and after 1 day inhibition, (c) SEM image for the surface after 1 day pre-corrosion after 2 days inhibition, (d) SEM image for the cross-section after 1 day pre-corrosion, (e) SEM image for the cross-section after 1 day pre-corrosion and after 1 day inhibition, and (f) SEM image for the cross-section after 1 day pre-corrosion and after 2 days inhibition.

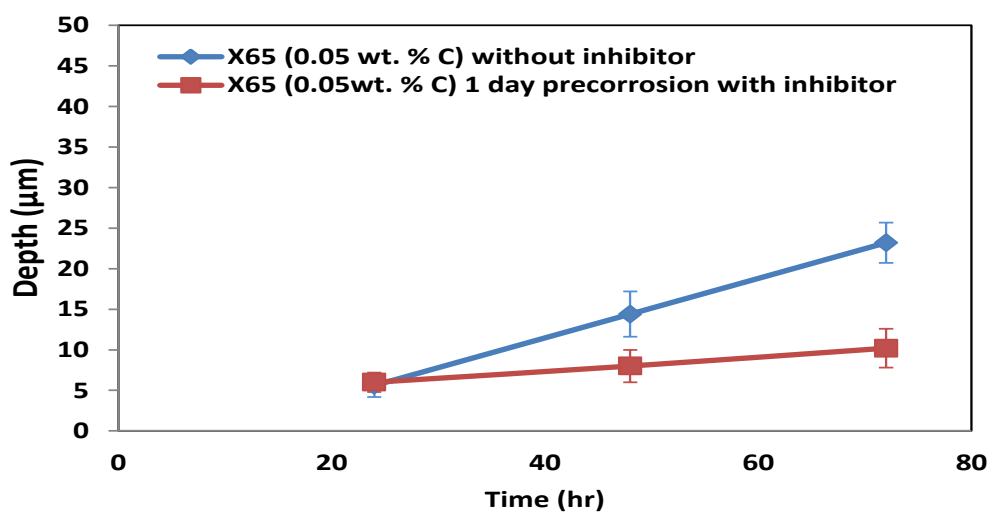


Figure 76. Depth of Fe_3C without and with imidazoline type inhibitor vs. time for experiments conducted at pH 5.0 and 60°C on X65 (0.05 wt. % C) steel.

Table 21

Thickness of Iron Carbide with Imidazoline-Type Inhibitor for X65 (0.05 wt.% C)

Test No.	Time	Thickness of Fe_3C (μm)	Depth CR (mm/yr)	Integrated LPR CR (mm/yr)
pH=5.0, T=60 °C				
1	1 day	6.0 +1.9/-2.5	2.2 +0.7/-0.9	7.6 ± 0.01
2	2 days	2.0 +0.3/-0.1	0.7 +0.10/-0.04	3.3 ± 0.01
3	3 days	4.2 +0.3/-0.1	0.8 +0.06/-0.02	0.5 ± 0.001

- X65 (0.05 wt. % C) spheroidized steel:

SEM images of top surface areas and cross-sections, respectively, for the pH 5.0 tests at 60°C on X65 (0.05 wt.% C) spheroidized steel with 1 day pre-corrosion in the presence of 2 CMC (72 ppm) of imidazoline-type inhibitor are shown in Figure 77. The surface morphology also shows no difference between the samples removed after each 24 hour interval. The surface morphology shows uniform corrosion and no scattered crystals of iron carbonate on the surface. The thickness of the iron carbide increased with time after 1 day pre-corrosion. When the inhibitor was added, the thickness of the iron carbide also slightly continued to increase with time after 1 day inhibited and 2 days inhibited, but not as much compared to the samples corroded without inhibitor for the same time interval. Figure 77 (d), Figure 77 (e), and Figure 77 (f) show that the iron carbide is present on the surface. Figure 78 shows that the depth of the iron carbide layer increased with time after 1 day of pre-corrosion. Then, it still slightly increased after inhibitor was added, but did not increase as much compared to the depth of the iron carbide layer for the experiment conducted with pre-corrosion and without the inhibitor. This resulted in higher corrosion rates with time after 1 day pre-corrosion, and then decreased after the inhibitor was added due to the action of inhibitors, but did not decrease as much compared to the corrosion rate for the experiment conducted without pre-corrosion and with the inhibitor, as shown in Figure 66. The depth of the iron carbide layer and depth corrosion rates for the pH 5.0 tests at 60°C on X65 (0.05 wt. % C) with 1 day pre-corrosion in the presence of 2 CMC (72 ppm) of imidazoline-type inhibitor for the exposed sample after days 1, 2, and 3 are shown in Table 22. Also, Table 22 represents the

integrated LPR corrosion rates for the pH 5.0 tests at 60°C on X65 (0.05 wt.% C) with 1 day pre-corrosion in the presence of 2 CMC (72 ppm) of imidazoline type inhibitor for the exposed sample after days 1, 2, and 3. The integrated LPR corrosion rate does not match the corrosion rates derived from the depth of the iron carbide. In addition, iron carbide impairs the performance of the inhibitor. The Fe₃C developed from C1018 spheroidized steel, high carbon content 0.18 wt. %, has more of an effect on the performance of the inhibitors than the Fe₃C developed from X65 (0.05 wt. % C), low carbon content, spheroidized steel due to the fact that when C1018 spheroidized steel is corroded, a layer of large spherical cementite particles remained on the surface. Also, this layer is discontinuous on the steel surface that permits the inhibitor to penetrate easily through this layer. However, when X65 (0.05 wt. % C) spheroidized steel is corroded, a layer of the trace percentage of the large spherical cementite particles remained on the surface. Also, this layer is also discontinuous on the steel surface and permits the inhibitor to penetrate more easily through this layer. Furthermore, mild steels with such structures appear to undergo more severe corrosion as compared to mild steels with ferrite and large spherical cementite particles in their structures, as is the case for the C1018 spheroidized steel, high carbon content 0.18 wt. %, in the current study. Consequently, the corrosion rate for the pH 5.0 tests at 60°C on C1018 spheroidized steel with 1 day pre-corrosion in the presence of 2 CMC (72 ppm) of imidazoline type inhibitor does not decrease as much compared to the corrosion rate for the pH 5.0 tests at 60°C on X65 (0.05 wt. % C) spheroidized steel with 1 day pre-corrosion in the presence of 2 CMC (72 ppm) of imidazoline type inhibitor due to such differences in their

microstructural features and chemical composition. Therefore, the performance of inhibitor after 1 day pre-corrosion is dependent on both the microstructure and chemical composition of the steel from which it is derived.

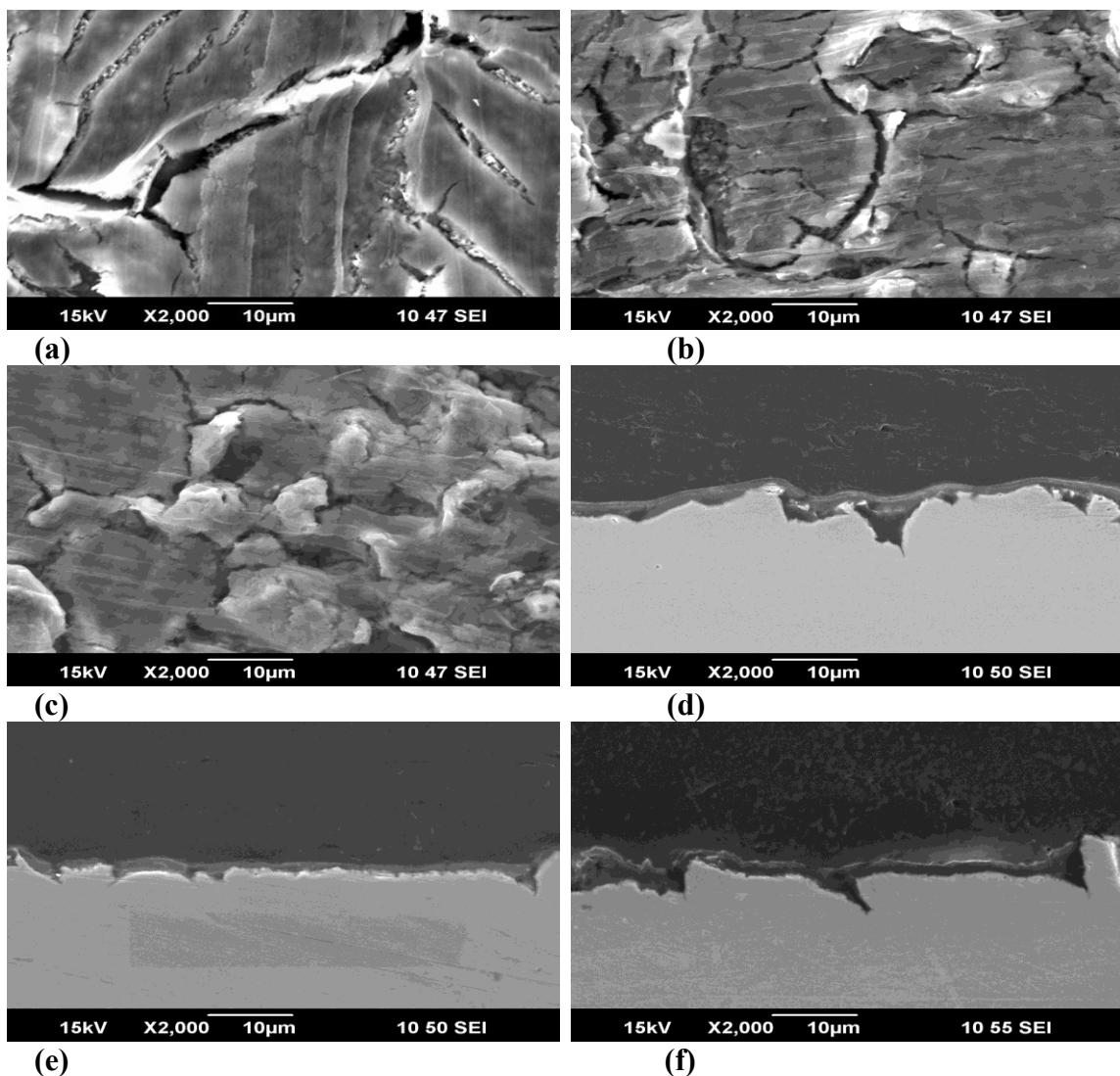


Figure 77. X65 (0.05 wt.% C) spheroidized samples recovered from bulk solution at pH 5 and 60°C (a) SEM image for the surface after 1 day pre-corrosion, (b) SEM image for the surface after 1 day pre-corrosion and after 1 day inhibition, (c) SEM image for the surface after 1 day pre-corrosion after 2 days inhibition, (d) SEM image for the cross-section after 1 day pre-corroded, (e) SEM image for the cross-section after 1 day pre-corroded and after 1 day inhibition, and (f) SEM image for the cross-section after 1 day pre-corroded and after 2 days inhibition.

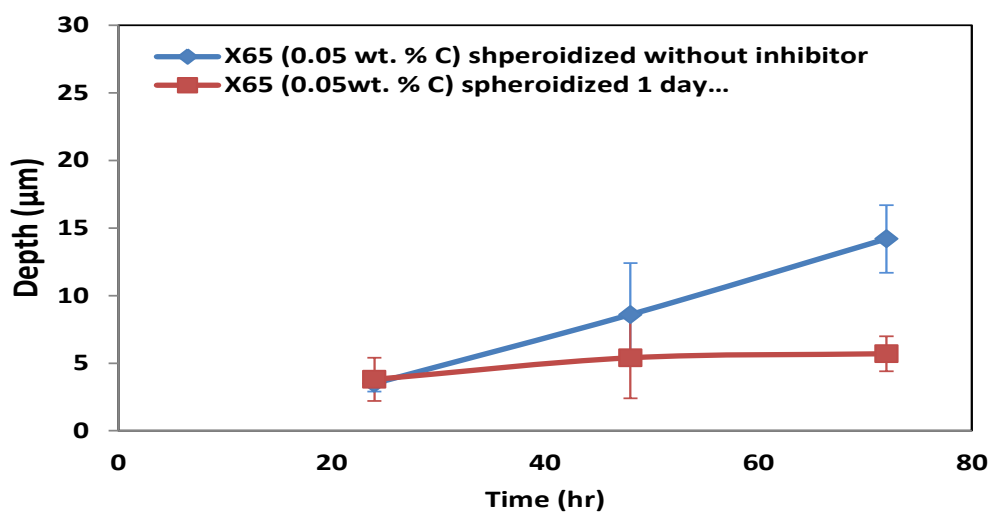


Figure 78. Depth of Fe_3C without and with imidazoline type inhibitor vs. time for experiments conducted at pH 5.0 and 60°C on X65 (0.05 wt. % C) spheroidized steel.

Table 22

Thickness of Iron Carbide with Imidazoline-Type Inhibitor for X65 (0.05 wt.% C) Spheroidized

Test No.	Time	Thickness of Fe_3C (μm)	Depth CR (mm/yr)	Integrated LPR CR (mm/yr)
pH=5.0, T=60 °C				
1	1 day	3.8 +3.1/-1.1	1.4 +1.1/-0.4	7.0 ± 0.03
2	2 days	1.6 +0.1/-0.1	0.6 +0.04/-0.04	2.7 ± 0.5
3	3 days	1.9 +0.1/-0.1	0.4 +0.02/-0.02	0.1 ± 0.01

5.3.3.1 Summary for Effect of Residual Fe₃C on Corrosion Inhibition

The performance of inhibitor on each type of steel was impaired after 1 day of pre-corrosion due to the presence of iron carbide derived from steel. However, the performance of the inhibitor on X65 (0.14 wt. % C) spheroidized was more impaired than the performance of the inhibitor on other type of steels. The performance of the inhibitor on X65 (0.05 wt. % C) spheroidized was less impaired than the performance of the inhibitor on other type of steels. Therefore, the performance of the inhibitor after 1 day pre-corrosion is also dependent on the microstructure and chemical composition of the steel.

The Fe₃C developed from X65 (0.14 wt. % C) steel has the greatest effect on the performance of the inhibitors than the Fe₃C developed from other types of steel due to the fact that the layer of the iron carbide developed from X65 (0.14 wt. % C) seems to remain a homogenous layer on the steel surface that does not permit the inhibitor to penetrate easily through this layer. However, The Fe₃C developed from X65 (0.05 wt. % C) spheroidized steel has a lowest effect on the performance of the inhibitors than the Fe₃C developed from other types of steel due to the fact that the layer of the iron carbide developed from X65 (0.05 wt. % C) spheroidized steel is present as a discontinuous layer on the steel surface that permits the inhibitor to penetrate more easily through this layer.

The integrated LPR corrosion rate does not match the depth of iron carbide for days 1, 2, and 3 for the pH 5.0 tests at 60°C on each type of steel with 1 day pre-corrosion in the presence of 2 CMC (72 ppm) of imidazoline-type inhibitor.

CHAPTER 6: CONCLUSIONS AND FUTURE WORK

6.1 Conclusions

A summary of the corrosion rate data for X65 and C1018 steels using different methods is shown in Table 23, Table 24, and Table 25. Subsequently, conclusions are drawn relating to the development of experimental procedures, role of Fe₃C on corrosion and effect of Fe₃C on inhibition.

Table 23

Summary of Corrosion Rate Data for X65 and C1018 Using Different Methods

Test No.	Initial pH, Temperature, and Time	Test Material	Integrated LPR CR	Depth CR	WL	CR comparison
			(mm/yr)	(mm/yr)	(mm/yr)	
Step1: Develop Experimental Procedure (X65 (0.14 wt.% C))						
1	pH=6.0, T=80 °C, 23 hr.	X65	3.3 ± 0.4	2.9 +2.2/-1.4	Unavailable	LPR= Depth
2	pH=6.0, T=60 °C, 24 hr.	X65	2.5 ± 1.1	2.2 +2.2/-1.1	Unavailable	LPR= Depth
3	pH=6.0, T=40 °C, 24 hr.	X65	2.0 ± 0.4	1.8 +0.9/-0.5	Unavailable	LPR= Depth
4	pH=5.0, T=60 °C, 24 hr.	X65	5.2 ± 0.9	3.1 +2.3/-1.6	4.3 ± 0.5	LPR≠ Depth≠WL

Table 24

Summary of Corrosion Rate Data for X65 and C1018 Using Different Methods

Time	Test Material	Integrated LPR CR	Depth CR	WL	CR comparison
(days)		(mm/yr)	(mm/yr)	(mm/yr)	
1	C1018 (F-P)	6.1 ± 0.5	4.5 +0.6/-1.7	4.2 ± 0.05	LPR≠ Depth=WL
2	C1018 (F-P)	7.5 ± 0.6	4.7 +0.9/-1.7	4.3 ± 0.2	LPR≠ Depth=WL
3	C1018 (F-P)	8.2 ± 0.5	5.2 +1.1/-1.3	5.2 ± 0.05	LPR≠ Depth=WL
1	C1018 (Sph.)	7.3 ± 0.1	1.7 +0.3/-0.2	3.5 ± 0.2	LPR≠ Depth≠WL
2	C1018 (Sph.)	9.2 ± 0.05	1.4 +1.0/-1.3	4.6 ± 0.1	LPR≠ Depth≠WL
3	C1018 (Sph.)	10.2 ± 0.3	1.3 +0.59/-0.63	5.2 ± 0.2	LPR≠ Depth≠WL
1	C1018 (Q-T)	9.9 ± 0.6	4.1 +0.7/-1.5	4.3 ± 0.2	LPR≠ Depth=WL
2	C1018 (Q-T)	11.1 ± 0.4	6.7 +0.0/-1.3	6.7 ± 0.2	LPR≠ Depth=WL
3	C1018 (Q-T)	13.2 ± 0.3	7.0 +1.3/-1.3	7.7 ± 0.1	LPR≠ Depth=WL
1	X65 (0.14 wt.% C)	6.5 ± 0.2	2.8 +0.90/-0.88	4.3 ± 0.3	LPR≠ Depth≠WL
2	X65 (0.14 wt.% C)	8.6 ± 0.2	3.0 +1.7/-1.5	4.8 ± 0.3	LPR≠ Depth≠WL
3	X65 (0.14 wt.% C)	9.7 ± 0.2	4.0 +0.8/-3.3	5.7 ± 0.2	LPR≠ Depth≠WL
1	X65 (0.05 wt.% C)	7.3 ± 0.05	2.0 +0.38/-0.45	5.8 ± 0.2	LPR≠ Depth≠WL
2	X65 (0.05 wt.% C)	8.8 ± 0.2	2.6+1.39/-1.37	6.5 ± 0.2	LPR≠ Depth≠WL
3	X65 (0.05 wt.% C)	9.5 ± 0.5	2.8 +0.9/-1.3	6.6 ± 0.2	LPR≠ Depth≠WL
1	X65 (0.05 wt.% C) Sph.	7.2 ± 0.1	1.3 +0.3/-0.5	4.1 ± 0.1	LPR≠ Depth≠WL
2	X65 (0.05 wt.% C) Sph.	7.7 ± 0.1	1.6 +0.8/-0.8	4.3 ± 0.1	LPR≠ Depth≠WL
3	X65 (0.05 wt.% C) Sph.	8.2 ± 0.1	1.7 +0.3/-0.4	4.8 ± 0.2	LPR≠ Depth≠WL

Table 25

Summary of Corrosion Rate Data for X65 and C1018 Using Different Methods

Time and Condition	Test Material	Integrated LPR CR (mm/yr)	Depth CR (mm/yr)	CR comparison
1 day	C1018 (F-P)	3.7 ± 0.3	$4.9 +0.9/-0.6$	LPR \neq Depth
Inhibitor, 2 days	C1018 (F-P)	1.0 ± 0.05	$2.4 +0.8/-0.5$	LPR \neq Depth
Inhibitor, 3 days	C1018 (F-P)	0.0 ± 0.003	$1.5 +0.05/-0.03$	LPR \neq Depth
1 day	C1018 (Sph.)	6.4 ± 0.3	$1.8 +0.6/-0.4$	LPR \neq Depth
Inhibitor, 2 days	C1018 (Sph.)	3.3 ± 0.4	$0.34 +0.08/-0.09$	LPR \neq Depth
Inhibitor, 3 days	C1018 (Sph.)	0.1 ± 0.005	$0.4 +0.03/-0.02$	LPR \neq Depth
1 day	C1018 (Q-T)	7.9 ± 0.5	$3.9 +0.5/-0.2$	LPR \neq Depth
Inhibitor, 2 days	C1018 (Q-T)	3.6 ± 0.2	$2.3 +0.05/-0.09$	LPR \neq Depth
Inhibitor, 3 days	C1018 (Q-T)	0.1 ± 0.003	$1.5 +0.02/-0.01$	LPR \neq Depth
1 day	X65 (0.14 wt.% C)	7.8 ± 0.4	$3.3 +1.3/-1.0$	LPR \neq Depth
Inhibitor, 2 days	X65 (0.14 wt.% C)	3.3 ± 0.1	$0.7 +0.07/-0.08$	LPR \neq Depth
Inhibitor, 3 days	X65 (0.14 wt.% C)	1.3 ± 0.05	$0.6 +0.02/-0.03$	LPR \neq Depth
1 day	X65 (0.05 wt.% C)	7.6 ± 0.01	$2.2 +0.7/-0.9$	LPR \neq Depth
Inhibitor, 2 days	X65 (0.05 wt.% C)	3.3 ± 0.01	$0.7 +0.10/-0.04$	LPR \neq Depth
Inhibitor, 3 days	X65 (0.05 wt.% C)	0.5 ± 0.001	$0.8 +0.06/-0.02$	LPR \neq Depth
1 day	X65 (0.05 wt.% C) Sph.	7.0 ± 0.03	$1.4 +1.1/-0.4$	LPR \neq Depth
Inhibitor, 2 days	X65 (0.05 wt.% C) Sph.	2.7 ± 0.5	$0.6 +0.04/-0.04$	LPR \neq Depth
Inhibitor, 3 days	X65 (0.05 wt.% C) Sph.	0.1 ± 0.01	$0.4 +0.02/-0.02$	LPR \neq Depth

Development of Experimental Procedures:

The pH 5.0 test at 60°C has a higher corrosion rate as compared to pH=6.0 tests at 80°C, 60°C, and 40°C because of the formation of a progressively thicker, high surface area iron carbide layer on which cathodic reduction reactions take place.

Supersaturation of iron carbonate is rapidly achieved for the pH 6.0 tests at 40°C, 60°C, and 80°C. The saturation limit relating to the bulk condition was not exceeded for the pH 5.0 test at 60°C. This means that there is a low probability for formation of an iron carbonate corrosion product layer that can confer protection [13]. Therefore, in order to avoid precipitation of an iron carbonate layer, pH 5.0 at 60°C was judged to be the best condition for this study. The absence of FeCO_3 was confirmed using Raman spectroscopy.

The thickness of the iron carbide decreased with time at low temperature and increased with time at high temperature. Also, this indicates that temperature has an effect on the development of the iron carbide. The thickness of iron carbide increased with time more for the pH 5.0 tests at 60°C than for pH 6.0 tests at 60°C. Also, this indicates that pH has an effect on the development of the iron carbide. It is also noteworthy that the thickest iron carbide was observed for the pH 5.0 tests at 60°C.

Integrated LPR corrosion rate matches depth of the iron carbide for the pH 6.0 tests at 80°C, 60°C, and 40°C, as shown in Table 23. However, the integrated LPR corrosion rate does not match depth corrosion rate at pH 5.0 for the test at 60°C, 24 hr.

Investigation of Post-Corrosion Fe_3C Characteristics Related to Material Microstructure:

The corrosion rate increases for each type of steel with time, but there is a higher corrosion rate for C1018 quenched-tempered. Consequently, experiments show that iron carbide layer development and corrosion rate are dependent upon the microstructure and chemical composition, particularly carbon content, of the carbon steel from which it is derived. The integrated LPR corrosion rate does not match the depth of the iron carbide and weight loss corrosion rate for days 1, 2, and 3 at the pH 5.0 tests at 60°C on each type of steel as shown in Table 24. However, the depth of iron carbide matches the weight loss corrosion on C1018 ferrite-pearlite and C1018 quenched-tempered steels. The best match is observed for day 3 at the pH 5.0 tests at 60°C, on C1018 ferrite-pearlite steel. The depth of iron carbide does not match the weight loss corrosion on C1018 spheroidized, X65 (0.14 wt. % C), X65 (0.05 wt. % C), and X65 (0.05 wt. % C) spheroidized steel.

Investigation of the Effect of Residual Fe_3C on Inhibitor Performance:

The performance of the inhibitor on each type of steel was impaired after 1 day of pre-corrosion due to the presence of iron carbide derived from steel. Figure 79 shows the trend of corrosion inhibitor performance based on LPR corrosion rate measurements for the studies steels. The corrosion rates derived from the depth of the iron carbide are also shown. In this Figure, it is important to mention that the depth corrosion rate is calculated based on the difference between the thickness of the iron carbide after one and two days inhibition. This differential value is believed somehow comparable with the final LPR reading. Based upon LPR, the performance of the inhibitor on X65 (0.14 wt. %

C) was more impaired than the performance of the inhibitor on other types of steel that were studied in this work. The performance of the inhibitor on X65 (0.05 wt. % C) spheroidized was least impaired. This steel has the lowest amount of residual carbide. Therefore, the performance of the inhibitor after 1 day pre-corrosion is also dependent on the microstructure and chemical composition of the steel. Therefore, in the field, corrosion inhibition can be adversely affected by the presence of carbide residues on the surfaces of production tubulars.

The Fe_3C developed from the X65 steel with the highest carbon content has the greatest effect on the performance of the inhibitors, as compared to the Fe_3C developed from the other types of studied steels. This is due to the fact that the layer of the iron carbide developed from X65 (0.14 wt. % C) is continuous and does not permit the inhibitor to penetrate to the steel below. However, the Fe_3C developed from X65 (0.05 wt. % C) spheroidized steel has the lowest effect on the performance of the inhibitor as the generated iron carbide layer is discontinuous and permits the inhibitor to penetrate more easily through this layer.

The integrated LPR corrosion rate does not match the depth of iron carbide for days 1, 2, and 3 for the pH 5.0 tests at 60°C on each type of steel with 1 day pre-corrosion in the presence of 2 CMC (72 ppm) of imidazoline-type inhibitor as shown in Table 25.

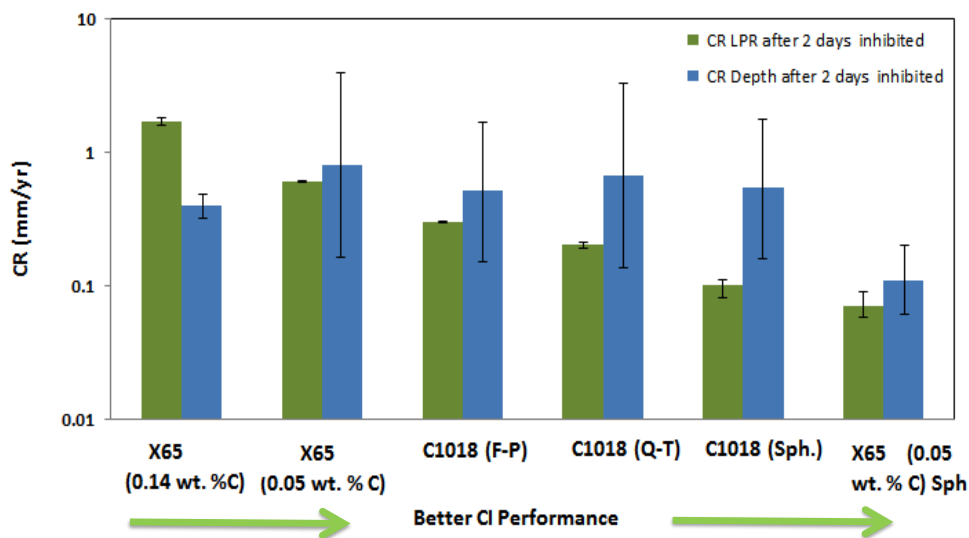


Figure 79. Trend of corrosion inhibitor performance with steel type.

6.2 Future Work

- 1- In order to observe and measure the effect of the iron carbide on corrosion inhibition, different types of inhibitor should be studied. It may be that an inhibitor can be identified that is more effective in the presence of carbide.
- 2- Do more heat treatments to a wider range of steels in order to observe the differences between them with respect to the thickness and morphology of the iron carbide layer. Also, observe their effect on the performance of inhibitor.
- 3- Use the carburization method, which is a process of diffusing carbon into a steel for hardening purposes, to enrich the surface with carbon with a view to changing the nature of the carbide residue.

- 4- Study the nature and effect of the residual alloying elements at the corroding steel surface.

6.3 Industrial Applicability

The applications of this study in industry are numerous. Many types of mild steel are used in the construction of pipeline transmission systems. Compared to the use of corrosion resistant materials, corrosion inhibitors used in combination with carbon steel can be an economic alternative for corrosion mitigation in oil and gas pipelines.

Therefore, such research that sheds light on factors that affect inhibitor performance, as well as mechanistic phenomena thereof, is of great importance regarding the design, qualification, and choice of inhibitors. This process can be used in common industrial applications, particularly in infrastructure for the production of oil and gas, in order to:

- 1- Increase production
- 2- Avoid unscheduled shutdowns
- 3- Reduce environmental contamination
- 4- Reduce high repair costs
- 5- Avoid fire accidents

These advantages are reflected in the cost of crude oil.

REFERENCES

- [1] H. G. Koch, P. H. B. Michiel, and N. G. Thompson, "Corrosion Costs and Preventive Strategies in the United States," *Rep. by CC Technol. Lab. Inc. to Fed. Highw. Adm. (FHWA), Off. Infrastruct. Res. Dev.*, Report FHWA-RD-01-156, 2001.
- [2] E. Gulbrandsen, R. Nyborg, T. Loland, and K. Nisancioglu, "Effect of Steel Microstructure and Composition on Inhibition of CO₂ Corrosion," *Corrosion/ 2000*, Houston, TX, NACE, Paper. 23.
- [3] E. Gulbrandsen and S. Netic, "Effect of Precorrosion on the Performance of Inhibitors for CO₂ Corrosion of Carbon Steel," *Corrosion/ 1998*, Houston, TX, NACE, Paper. 13.
- [4] K. Kowata and K. Takahashi, "Interaction of Corrosion Inhibitors with Corroded Steel Surface," *Corrosion 96*, p. 219, 1996.
- [5] S. Papavinasam, "Corrosion Inhibitors," *John Wiley & Sons. Inc.*, 2000.
- [6] S. D. Kapusta, P. R. Rhodes, and D. A. Silverman, "Inhibitor Testing for CO₂ Environments," *Corrosion 91*, p. 471, 1991.
- [7] R. H. Hausler, D. W. Stegman, C.I.Cruz, and D. Tjandroso, "Laboratory Studies on Flow Induced Localized Corrosion in CO₂ / H₂S Environments. III. Chemical Corrosion Inhibition," *Corrosion 90*, p. 7, 1990.
- [8] R. H. Hausler and D. W. Stegman, "Laboratory Studies on Flow Induced Localized Corrosion in CO₂ / H₂S Environments. IV. Assessment of the Kinetics of Corrosion Inhibition by Hydrogen Evolution Measurements," *Corrosion 91*, p. 474, 1991.

- [9] S. Nešić and W. Sun, Shreir's Corrosion: Corrosion in acid gas solutions, Fourth Edition, Vol. 2. Amsterdam: Elsevier, 2010, pp. 1270–1298.
- [10] M. Nordsveen, S. Nešić, R. Nyborg, and A. Stangeland, "A Mechanistic Model for Carbon Dioxide Corrosion of Mild Steel in the Presence of Protective Iron Carbonate Films—Part 1: Theory and Verification," *Corrosion*, vol. 59, no. 5, pp. 443–456, 2003.
- [11] V. Ruzic, M. Veidt, and S. Nešić "Protective FeCO₃ layers - Part 1: Mechanical removal in single-phase aqueous flow," *Corrosion*, vol. 62, no. 5, pp. 419–432, 2006.
- [12] S. Nešić, M. Nordsveen, R. Nyborg, and A. Stangeland. "A mechanistic model for carbon dioxide corrosion of mild steel in the presence of protective iron carbonate films – part 2:Numerical experiment," *Corrosion*, vol. 59, no. 6, pp. 489 –497, 2003.
- [13] S. Nešić and L. Lunde, "Carbon dioxide corrosion of carbon steel in two-phase flow," *Corrosion*, vol. 50, no. 9, pp. 717–727, 1994.
- [14] A. Dugstad, "Mechanism of Protective film formation during CO₂ Corrosion of Carbon Steel," *Corrosion/1998*, Houston, TX, NACE, Paper. 31.
- [15] J. L. Crolet, N. Thevenot, and S. Nešić, "Role of Conductive Corrosion Products in the Protectiveness of Corrosion Layers," *Corrosion*, vol. 54, no. 3, pp. 194–203, 1998.
- [16] C. de W. and U. Lotz, "Prediction of CO₂ corrosion of carbon steel," *Corrosion/1993* Houston, TX, NACE, Paper. 69.

- [17] C. De Waard, U. Lotz, and A. Dugstad, "Influence of liquid flow velocity on CO₂ corrosion. A semi-empirical model," *Corrosion/1995*, Houston, TX, NACE, Paper. 128.
- [18] D. Lopez, T. Perez, and S. Simison, "The Influence of Microstructure and Chemical Composition of Carbon and Low Alloy Steels in CO₂ Corrosion. A State-of-the-art Appraisal," *Elsevier Ltd, Material and Design*, vol. 24, pp. 561–575, 2003.
- [19] J. W. and A. Atrens, "Microstructure and grain boundary microanalysis of X70 pipeline steel," *Journal of Material . Science.*, vol. 38, pp. 323 – 1330, 2003.
- [20] S. Thompos, D. Colvin, and G. Krauss, "Continuous cooling transformations and microstructures in a low carbon, high-strength low-alloy plate steel," *Metall.. Trans. A*, vol. 21, p. 1493, 1990.
- [21] A. Dugstad, H. Hemmer, and M. Seiersten "Effect of Steel Microstructure upon Corrosion Rate and Protective Iron Carbonates Film Formation," *Corrosion/2000*, Houston, TX, NACE, Paper. 24.
- [22] F. Farelas, B. Brown, and S. Nešić "Iron Carbide & Its Influence on Formation of Protective Iron Carbonate in CO₂ Corrosion of Mild Steel," *Corrosion/2013*, Houston, TX, NACE, Paper. 229.
- [23] D. Lopez, W. Schreiner, S. de Sanchez, and S. Simison, "The influence of carbon steel microstructure on corrosion layers. An XPS and SEM characterization," *Appl Surf Sci*, vol. 207, pp. 69–85, 2003.
- [24] D. Lopez, S. Simison, and S. de Sanchez, "The influence of steel microstructure on CO₂ corrosion. EIS studies on the inhibition efficiency of benzimidazole," *Electrochim Acta*, vol. 48, no. 7, pp. 845–854, 2003.

- [25] E. S. Akeer, "Effect of Carbon Steel Composition and Microstructure on CO₂ Corrosion," Ph.D. dissertation, Dept. Ch. Eng., Ohio Univ., Athens, OH, 2014.
- [26] M. Salcu, "Increasing the Lifetime of J55 Tubing by Improving Steel Metallurgy Laboratory and Field Tests Achievements," *Corrosion/2013*, Houston, TX, NACE, Paper. 2141.
- [27] P. Nice and M. Udea, "Effect of microstructure and chromium alloying content to the corrosion resistance of low-alloy steel well tubing in seawater injection service," *Corrosion/1998*, Houston, TX, NACE, Paper. 3.
- [28] M. B. Kermani and A. Morshed, "Carbon Dioxide Corrosion in Oil and Gas Production—A Compendium," *Corrosion 2003*, vol. 59, no. 8, pp. 659–683, Aug. 2003.
- [29] W. F. Smith and J. Hashemi, *Foundations of Materials Science and Engineering*, 4th ed. McGraw-Hill Publishing., 2006.
- [30] G. A. Zhang, Y. Zeng, X. P. Guo, F. Jiang, D. Y. Shi, and Z. Y. Chen, "Electrochemical Corrosion Behavior of Carbon Steel Under Dynamic High Pressure H₂S/CO₂ Environment," *Corrosion Science*, vol. 65, pp. 37–47, Dec. 2012.
- [31] H. B. Wang, H. Shi, T. Hong, C. Kang, and W. P. Jepson, "Characterization of Inhibitor and Corrosion Product Film Using Electrochemical Impedance Spectroscopy (EIS)," *Corrosion/2001*, Houston, TX, NACE, , Paper. 01023.
- [32] M. Ueda and H. Takabe, "Effect of Environmental Factor and Microstructure on Morphology of Corrosion Products in CO₂ Environments," *Corrosion99*, no. 13, 1999.

- [33] S. Nešić and L. Lunde, "CO₂ Corrosion of Carbon Steel in The Two-Phase Flow," *Corrosion/1993*, Houston, TX, NACE, Paper. 640.
- [34] S. Al-Hassan, B. Mishra, D. L. Olson, and M. M. Salama, "Effect of Microstructure on Corrosion of Steels in Aqueous Solutions Containing Carbon Dioxide," *Corrosion*, vol. 54, no. 6, pp. 480–491, Jun. 1998.
- [35] V. K and D. A, "Galvanic Influence of CO₂ Corrosion ," *CORROSION/89*, p. 468, 1989.
- [36] D. Askeland, P. Fulay, and W. Wright, "The Science and Engineering of Materials, Sixth Edition, CT.," Cengage Learning. Stamford, CT. 2006, pp. 493–531, 2006.
- [37] T. B. Massalski, H. Okamoto, P. R. Subramanian, and L. Kacprzak, "Binary alloy phase diagrams, Second Edition, " vol. 1, ASM international, Materials Park, OH, 1990, ch. 10, pp. 359-420.
- [38] Micrograph Library, University of Cambridge. Available: <http://www.doitpoms.ac.uk/miclib/pds.swf?targetFrame=Fe-C-X>, [May. 25, 2014]
- [39] 2000 MATTER, The University of Liverpool. Available: http://www.matter.org.uk/steelmatter/metallurgy/7_1_2.html, [May. 25, 2014]
- [40] G. Schmitt and B. Rothmann, "Corrosion mechanism of unalloyed steel in oxygen free carbon dioxide solutions - Part 1: Kinetics of the liberation of hydrogen," *Werkst. Korros.*, Vol. 28, No. 12, pp. 816-822, 1977.
- [41] W. Sun, S. Nešić, and R. C. Woollam, "The Effect of Temperature and Ionic Strength on Iron Carbonate (FeCO₃) Solubility Limit," *Corrosion Science*, vol. 51, no. 6, pp. 1273–1276, Jun. 2009.

- [42] A. Edwards, et al., "Mechanistic studies of the corrosion inhibitor oleic imidazoline," *Corrosion Science*, vol. 36, no. 2, pp. 315-325, 1994.

APPENDIX A: ANALYTICAL REPORT

Table A1
Analytical Report for X65 Steels by Nadcap

Material	Microstructure	Rockwell B Hardness (HRB)
X65 (0.14 wt. % C)	fine structure of pearlite in a ferrite matrix	87
X65 (0.05 wt. % C)	fine structure of pearlite in a ferrite matrix	87



OHIO
UNIVERSITY

Thesis and Dissertation Services